

NOELE FRANCHI LEONARDO

**CICLO BIOGEOQUÍMICO MARINHO NO ÚLTIMO MÁXIMO GLACIAL E
NO INTERGLACIAL *MARINE ISOTOPE STAGE 11C***

Tese apresentada à Universidade Federal de Viçosa, como parte das exigências do Programa de Pós-Graduação em Meteorologia Aplicada, para obtenção do título de *Doctor Scientiae*.

VIÇOSA
MINAS GERAIS - BRASIL
2019

**Ficha catalográfica preparada pela Biblioteca Central da Universidade
Federal de Viçosa - Câmpus Viçosa**

T

L581m
2019 Leonardo, Noele Franchi, 1985-
Ciclo biogeoquímico marinho no último máximo glacial e no
interglacial *marine isotope stage11c* / Noele Franchi Leonardo. –
Viçosa, MG, 2019.
xiii, 130 f. : il. (algumas color.) ; 29 cm.

Texto em inglês.

Orientador: Flavio Barbosa Justino.

Tese (doutorado) - Universidade Federal de Viçosa.

Inclui bibliografia.

1. Biogeoquímica. 2. Oceano Antártico.
3. Paleoclimatologia. 4. Interação Oceano-Atmosfera. 5. Dióxido
de Carbono. I. Universidade Federal de Viçosa. Departamento de
Engenharia Agrícola. Programa de Pós-Graduação em
Meteorologia Aplicada. II. Título.

CDD 22 ed. 577.14

NOELE FRANCHI LEONARDO

**CICLO BIOGEOQUÍMICO MARINHO NO ÚLTIMO MÁXIMO GLACIAL
E NO INTERGLACIAL MARINE ISOTOPE STAGE 11c**

Tese apresentada à Universidade Federal de Viçosa,
como parte das exigências do Programa de Pós-
Graduação em Meteorologia Aplicada, para obtenção
do título de *Doctor Scientiae*.

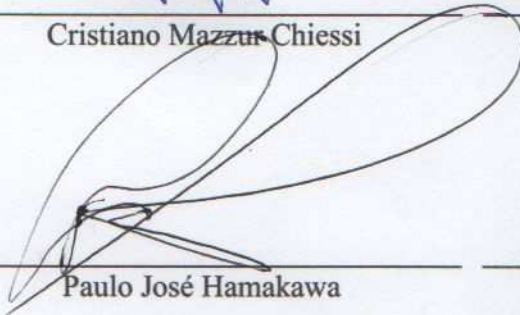
APROVADA: 24 de junho de 2019.



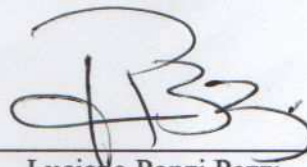
Cristiano Mazzur-Chiessi



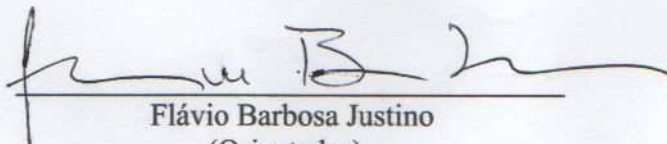
Lincoln Muniz Alves



Paulo José Hamakawa



Luciano Ponzi Pezzi



Flávio Barbosa Justino
(Orientador)

Agradecimentos

Ao meus pais (Luiz e Gislem), meus irmãos (Di e Eric) e meus dois amorzinhos, Julia e Luiza, muito Obrigada pelo amor incondicional. **AMO VOCÊS.**

Ao professor Dr. Flávio Justino por ter acreditado me mim, pelo incentivo em cursar o Doutorado, além dos churrascos e das conversas jogadas fora.

Ao programa de Meteorologia Aplicada da Universidade Federal de Viçosa, professores e funcionários, pela oportunidade de realizar o Doutorado.

À Coordenação Pessoal de Nível Superior (CAPES) pelo suporte financeiro.

Aos meus amigos e colegas da Pós-Graduação que me acompanharam e incentivaram: Vanúcia, Marcos Paulo, Alex, Cristian, Álvaro, Douglas, Carlos (vulgo Diego ou Gurjão), Pousa, Ricardo, Gabriel e Rafael pelas conversas, risadas e *bons drinks*.

À melhor pessoa de toda essa universidade Graça Freitas por toda a sua disposição em ajudar, aconselhar, todo o carinho e paciência. Saiba que esse programa não existe sem você.

Aos amigos que fiz nessa caminhada de doutorado e que levo para a vida; Danilo, Maria Clara, Chico, Marcinha, Priscila, Rafael, Ricardo, Vágna e Eli.

Em especial, Marcela e Marlos por todo o companheirismo, amizade, todas as conversas e por terem me amparado na casa de vocês. Obrigada de coração por todo o suporte e ajuda que vocês me deram, vocês são minha família.

Aos meus amigos distantes e que sempre estiveram presentes em minha vida, mesmo eu faltando em casamentos, batizados, aniversários e chá de bebê. **AMO VOCÊS.**

À Prof. Dra. Alessandra Fonseca da Universidade Federal de Santa Catarina por ter me acolhido em seu laboratório e por me mostrar o gigante mundo da Biogeoquímica Marinha.

Ao Dr. Juan Muglia do *School of Earth and Ocean Sciences -University of Victoria* pela paciência no processo simulação do modelo e as contribuições nos artigos.

À banca de avaliação da tese: Dr. Luciano Ponzi Pezzi, Dr. Paulo Hamakawa, Dr. Lincoln Muniz Alvez e Dr. Cristiano M. Chiessi por toda a contribuição para que esse processo se finalizasse da melhor maneira possível. Muito Obrigada.

Por último e não menos importante, não posso deixar de agradecer aos oceanos, por toda inspiração, conhecimento, conforto e pelo prazer que é tentar te entender melhor.

Meu sinceros agradecimentos a todos vocês que direta ou indiretamente construíram essa tese comigo..

Sumário

Lista de Figuras	v
Lista de Tabelas	ix
Resumo	x
Abstract	xii
1 Introdução	1
1.1 Apresentação da Tese	4
1.2 Objetivos	5
1.2.1 Objetivos Específicos	5
1.3 Fundamentação Teórica	5
1.3.1 Forçantes Orbitais e Mudanças Climáticas	5
1.3.2 Períodos Glaciais e Interglaciais	7
1.3.3 Ciclo do Carbono nos Oceanos	11
1.4 Descrição do Modelo	14
1.4.1 UVic ESCM	14
2 The Impact of ICE-6G Ice Sheet Topography in the Oceanic Carbonate System	30
2.1 Introduction	32
2.2 Data and Model Setup	35
2.2.1 Model Description	35
2.2.2 Paleotopography Experiments	37
2.2.3 Experimental Design	38
2.2.4 Wind Stress	39
2.2.5 Evaluation of the present day simulation	40
2.3 Results and Discussion	44
2.3.1 ICE6G Climate	44
2.3.2 The Glacial Marine Carbon System	50
2.4 Climate Variability	56
2.4.1 Global Wind Stress Variability and the Oceanic Biogeochemistry	56
2.4.2 The Pacific Decadal Oscillation and the Oceanic Biogeochemistry	60
2.5 Summary and concluding remarks	65
3 Southern Ocean response to Glacial and Interglacial Forcing	77
3.1 Introduction	79
3.2 Climate model and simulations	82
3.2.1 Carbonate System	84

3.2.2	Model, LGM and MIS11c Climate Validation	86
3.3	LGM and MIS11c climate state	90
3.3.1	$f\text{CO}_2$ exchange processes	96
3.3.2	Biological production	98
3.3.3	Carbonate Chemistry	102
3.3.4	Characteristics in the Weddell Sea	110
3.4	Summary and Conclusions	117
4	Perspectivas Futuras	130

Lista de Figuras

1.1	Ciclos de Milankovitch. Adaptada de Zachos et al. (2001)	6
1.2	Efeito da formação e dissolução do CaCO_3 na alcalinidade total, TCO_2 e na $p\text{CO}_2$ oceânica. Adaptada de (Zeebe and Wolf-Gladrow, 2001 ; Sigman and Boyle, 2000).	13
1.3	Fluxograma do UVic ESCM, com cada componente climático associado ao acoplador; oceano, sedimento, terrestre, atmosfera e gelo marinho. Os fluxos são representados pelas setas e as cores apontam de onde são originados. O tamanho dos círculos representam o tamanho relativo do código base. Adaptado de (Wania et al., 2012) .	17
2.1	(a) Paleotopography anomalies between ICE6G and PD reconstructions [Km]. (b) as (a) but for ICE6G and ICE4G reconstructions (c) surface temperature differences between ICE6G and PD simulations ($^{\circ}\text{C}$). (d) As (c) but for ICE6G and ICE4G differences. Hachured areas are statistically significant at the 95% level.	38
2.2	Standard deviation for simulated zonal and meridional surface wind stress for (a;b) PMIP3, (c;d) ICE6G and (e;f) ICE4G. Simulated annual mean zonal (g) and meridional (h) surface wind stress over the ocean for PMIP3 (black), ICE6G (blue), ICE5G (red) and ICE4G (green). PMIP3 data from (Muglia and Schmittner, 2015)	41
2.3	Taylor diagram comparing statistic pattern of annual mean fields between UVic ESCM simulation control and corresponding GLO-DAP_v2 observations, including surface temperature, salinity, nitrate, phosphate, total alkalinity and TCO_2 . All fields are normalized by the standard deviation of corresponding observations. Indeed, observation fields have a standard deviation of one, which is represented by REF (x label). The distance between the model points and the reference point indicate the quadratic -root-mean-square (QRMS) difference between model simulation and observations.	45
2.4	(a) Annual mean wind speed anomalies between ICE6G and PD (m/s). (b) sea surface temperature ($^{\circ}\text{C}$) and (c) E-P flux (mm/day); (b), (d) and (f) are the same as (a), (c) and (d) but for differences between ICE6G and ICE4G runs. Hachured areas are statistically significant at the 95% level.	46
2.5	Global meridional overturning circulation based on (a) PD conditions, (b) ICE6G (c) ICE4G and (d) differences between ICE-6G and PD and (e) anomalies between ICE6G and ICE4G.	48

2.6	Global ocean basin average vertical profile of temperature ($^{\circ}\text{C}$) and salinity, from simulations of PD, ICE6G and ICE4G.	49
2.7	Anomalies between the ICE6G and PD (a, TA), (c, TCO_2), (e, NO_3^-) and (g, PO_4^{3-}). Anomalies between ICE6G and ICE4G simulations (b, Ta), (d, TCO_2), (f, NO_3^-) and (h, PO_4^{3-}). Hatched areas are statistically significant at the 95% level.	53
2.8	Global ocean basin average vertical profile of TA $\mu\text{mol}/\text{kg}$, TCO_2 $\mu\text{mol}/\text{kg}$, O_2 $\mu\text{mol}/\text{kg}$, NO_3 $\mu\text{mol}/\text{kg}$ and PO_4^{3-} $\mu\text{mol}/\text{kg}$ from simulations of PD, ICE6G and ICE4G.	55
2.9	Global response associated with the 1 st EOF related to zonal wind stress. The patterns are displayed by amplitudes by regressing; (a) wind stress (Pa), (b) SST ($^{\circ}\text{C}$), (c) SSS and (g) E-P flux anomalies upon the standardized first principal component time series.	57
2.10	Same as in Fig. 6 but for surface (a) TA ($\mu\text{mol}/\text{kg}$), (b) TCO_2 ($\mu\text{mol}/\text{kg}$), (c) NO_3^- ($\mu\text{mol}/\text{kg}$) and (d) PO_4^{3-} ($\mu\text{mol}/\text{kg}$).	60
2.11	First component of the PDO (a) PD, (b) ICE6G and (c) ICE4G simulations. Regression anomalies between ICE6G and PD (d) simulations and ICE6G and ICE4G simulations (e). The top-right percentage values represent the respective explained variance of the first EOF.	61
2.12	Regression anomalies between for ICE6G and PD simulations (a) SST, (b) SSS, (c) E-P flux and (d) wind speed. These patterns are shown by regressing the 1 st PC of the PDO onto the SST, SSS, E-P flux and wind speed.	62
2.13	Same as figure 8 but for surface (a) TA, (b) TCO_2 , (c) NO_3^- and (d) PO_4^{3-}	63
3.1	Taylor diagram comparing statistical pattern of annual mean fields between UVic ESCM simulation control and corresponding GLODAP_v2 observations, including surface temperature, salinity, nitrate, phosphate, total alkalinity and TCO_2 . All fields are normalized by the standard deviation of corresponding observations. Indeed, observation fields have a standard deviation of one, which is represented by REF (x label). The distance between the model points and the reference point indicates the quadratic root-mean-square (QRMS) difference between model simulation and observations.	87
3.2	(a) Topography differences between LGM and PD simulations (km), Sea level temperature anomalies ($^{\circ}\text{C}$) between (b) LGM and PD, (d) MIS11c and PD. (c) Monthly insolation anomalies simulation at the top of the atmosphere for interglacial MIS11c (Wm^{-2}) with respect to the current orbit.	89
3.3	Ice thickness for (a) LGM, (b) MIS11c, (c) anomalies. Note the nonlinear bar label axes.	92

3.4	Temperature in °C for the surface (a) LGM,(b) MIS11c, (c) anomalies and averaged meridional crosscut for (d) LGM, (e) MIS11c and (f) anomalies. Note the nonlinear vertical axes, used to zoom in on the upper ocean layers. Hachured areas are statistically significant at the 95% level.	94
3.5	Same as Fig. 3.4 for Salinity . Note the nonlinear vertical axes, used to zoom in on the upper ocean layers.Hachured areas are statistically significant at the 95% level.	95
3.6	Atlantic Meridional Overturning in Sv for: a) LGM, b) MIS11c and c) LGM - MIS11c.	96
3.7	Annual mean surface ocean $p\text{CO}_2$ (ppm) calculated by CO2SYS for (a)MIS11c and b) LGM.	97
3.8	O_2 in $\mu\text{mol}/\text{kg}$ for the surface (a) LGM,(b) MIS11c, (c) anomalies and averaged meridional crosscut for (d) LGM, (e) MIS11c and (f) anomalies. Note the nonlinear vertical axes, used to zoom in on the upper ocean layers.	99
3.9	NO_3^- in $\mu\text{mol}/\text{kg}$ for the surface (a) LGM,(b) MIS11c, (c) anomalies and averaged meridional crosscut for (d) LGM, (e) MIS11c and (f) anomalies. Note the nonlinear vertical axes, used to zoom in on the upper ocean layers.	101
3.10	PO_4^{3-} in $\mu\text{mol}/\text{kg}$ for the surface (a) LGM,(b) MIS11c, (c) anomalies and averaged meridional crosscut for (d) LGM, (e) MIS11c and (f) anomalies. Note the nonlinear vertical axes, used to zoom in on the upper ocean layers.	101
3.11	TA in $\mu\text{mol}/\text{kg}$ for the surface (a) LGM,(b) MIS11c, (c) anomalies and averaged meridional crosscut for (d) LGM, (e) MIS11c and (f) anomalies. Note the nonlinear vertical axes, used to zoom in on the upper ocean layers.	102
3.12	TCO_2 in $\mu\text{mol}/\text{kg}$ for the surface (a) LGM,(b) MIS11c, (c) anomalies and averaged meridional crosscut for (d) LGM, (e) MIS11c and (f) anomalies. Note the nonlinear vertical axes, used to zoom in on the upper ocean layers.	104
3.13	pH for the surface (a) LGM,(b) MIS11c, (c) anomalies and averaged meridional crosscut for (d) LGM, (e) MIS11c and (f) anomalies. Note the nonlinear vertical axes, used to zoom in on the upper ocean layers.	105
3.14	CO_3^{2-} in $\mu\text{mol}/\text{kg}$ for the surface (a) LGM,(b) MIS11c, (c) anomalies and averaged meridional crosscut for (d) LGM, (e) MIS11c and (f) anomalies. Note the nonlinear vertical axes, used to zoom in on the upper ocean layers.	106
3.15	HCO_3^- in $\mu\text{mol}/\text{kg}$ for the surface (a) LGM,(b) MIS11c, (c) anomalies and averaged meridional crosscut for (d) LGM, (e) MIS11c and (f) anomalies. Note the nonlinear vertical axes, used to zoom in on the upper ocean layers.	107

3.16 Ω CaCO ₃ for the surface (a) LGM,(b) MIS11c, (c) anomalies and averaged meridional crosscut for (d) LGM, (e) MIS11c and (f) anomalies. Note the nonlinear vertical axes, used to zoom in on the upper ocean layers.	108
3.17 Depth profile of Ω aragonite on Southern Ocean. Black line for LGM simulations and red for MIS11c. Gray line for $\Omega = 1$ are the <i>Aragonite Saturation Horizon</i> (ASH), dashed lines show the depth of ASH for each simulation.	109
3.18 Globally averaged of Weddell Sea vertical profiles of temperature (°C), salinity, oxygen, phosphate and nitrate (all in $\mu\text{mol}/\text{kg}$).Black lines show LGM distributions; red lines show MIS11c concentrations calculated within UVic experiments. Note the nonlinear vertical axes, used to zoom in on the upper ocean layers	111
3.19 Same as Fig. 3.18 but for TA, TCO ₂ , carbonate, bicarbonate (all in $\mu\text{mol}/\text{kg}$), pH and Ω CaCO ₃ . Black lines show LGM distributions; red lines show MIS11c concentrations calculated within UVic experiments and CO2SYS. Gray line for $\Omega = 1$ are the <i>Aragonite Saturation Horizon</i> (ASH), dashed lines show the depth of ASH for each simulation. Note the nonlinear vertical axes, used to zoom in on the upper ocean layers.	114

Lista de Tabelas

1.1	Parâmetros orbitais para o LGM e para a era pré-industrial (adaptada do <i>Paleoclimate Modelling Intercomparison Project – PMIP</i>)	8
1.2	Parâmetros orbitais para o MIS11c e para a era pré-industrial (adaptada de Melles et al. (2012) ; Raymo and Mitrovica (2012))	10
1.3	Sumário das simulações.	18
2.1	Global surfaces averages, differences, correlation coefficient and standard deviation-normalized root mean square error (RMSE) between UVic ESCM simulation control versus GLODAP_v2 (Olsen et al., 2016) observations. For Global, NH and SH subtropics and Tropical region averages.	43
3.1	Orbital parameters for LGM, MIS11c and for the control (adapted from (Berger and Loutre, 1991 ; Loulergue et al., 2008 ; Coletti et al., 2015a ; NOAA, 2018)).	83
3.2	Anomalies sea surface temperature from LGM-PD from the reconstructions for the Southern Ocean comparative.	89
3.3	Comparative for PD and MIS11c insolation at the top of atmosphere between UVic simulation and Coletti et al. (2015a) . The analyzes were done for the point referring to the Lake El'gygytgyn for the month of greatest insolation especially July, for surface temperature and TOA.	90
3.4	Surface mean values for Southern Ocean of physical and biogeochemical parameters calculated with UVic ESCM and CO2SYS for control, MIS11c and LGM.	93

Resumo

LEONARDO, Noele Franchi, D.Sc., Universidade Federal de Viçosa, junho de 2019. **Ciclo Biogeoquímico marinho no Último Máximo Glacial e no Interglacial *Marine Isotope Stage 11c***. Orientador: Flávio Barbosa Justino.

As flutuações atmosféricas das concentrações de CO₂ têm sido fortemente correlacionadas com o clima em escalas de tempo de milhões de anos, ou causadas, ou pelo menos, amplificando as mudanças climáticas. Este estudo procurou investigar a relação entre as mudanças nas forçantes orbitais, concentração de CO₂ e topografia no ciclo biogeoquímico marinho. Para isso foi utilizado o modelo UVic ESCM versão 2.9, que é um modelo de complexidade intermediária acoplado para simular o clima médio no Último Máximo Glacial (LGM) e Interglacial Isotope Marine Stage 11c (MIS11c). Com relação às simulações, o modelo UVic foi capaz de representar satisfatoriamente as condições climáticas atuais (PD), com boa correlação e baixos valores de erro quadrático médio. Para paleoreconstruções, mesmo com a baixa disponibilidade de dados, principalmente para o Interglacial MIS11c, boa concordância com outros estudos foram encontradas. Com a adição da topografia ICE6G, a temperatura média no LGM foi de aproximadamente 5 °C mais fria do que encontrada nos dias atuais, houve modificação na circulação atmosférica, especialmente nas regiões do Atlântico e do Pacífico Norte. Diferenças significativas foram encontradas na comparação entre duas topografias para o LGM; ICE6G e ICE4G. Aquecimento de aproximadamente 3 °C no Atlântico Norte, como resultado do aumento da concentração de gelo na América do Norte para a topografia ICE6G, provavelmente causada por subsidência ao sul e leste da anomalia topográfica. Anomalias positivas e negativas variam amplamente para o padrão de fluxo Evaporação-Precipitação (E-P), com a atmosfera mais fria e mais seca levando a uma redução na precipitação de LGM nas regiões da Europa. Mudanças na temperatura da superfície do mar e salinidade e fluxos de E - P levam a mudanças no sistema de carbonato oceânico, resultando em um aumento geral na alcalinidade total e uma redução nas concentrações totais de carbono dissolvido (TCO₂) em LGM em relação ao PD. Esta é uma consequência da baixa concentração de

CO₂ e do aumento nas concentrações de carbonato de cálcio (CO₃²⁻) levando ao aumento do pH oceânico. Mudanças na intensidade da Circulação de Revolvimento Meridional entre os períodos glacial e interglacial levaram a mudanças nos padrões de circulação oceânica, diminuindo sua intensidade no Último Máximo Glacial em relação ao PD e MIS11c. A resposta do ciclo biogeoquímico ao LGM e MIS11c simulado para o Oceano Austral mostrou um grande aumento na superfície de oxigênio a partir de 55 °S e uma diminuição na Antártica (particularmente no Mar de Weddell). Análises de nitrato (NO₃⁻), fosfato (PO₄³⁻), TCO₂ e alcalinidade total (TA) mostram que elas estão intimamente ligadas a variações em CO₂ concentrações entre atmosfera e superfície oceânica, assim como a disponibilidade de sedimentação do CaCO₃.

Abstract

LEONARDO, Noele Francho, D.Sc., Universidade Federal de Viçosa, June, 2019. **Marine Biogeochemical Cycle for Last Glacial Maximum and Marine Isotope Stage 11c.** Advisor: Flávio Barbosa Justino.

Atmospheric CO₂ fluctuations have been highly correlated with climate on million years time scales, or caused or at least amplified, the climatic changes. This thesis sought to investigate the relationship between orbital forcings and different concentrations of CO₂ in the marine biogeochemical carbon cycle. For this, we used the model UVic ESCM version 2.9, which is a coupled model to simulate the average climate in the Last Glacial Maximum (LGM) and Interglacial Marine Isotope Stage 11c (MIS11c). Regarding the simulations, the UVic model was able to satisfactorily represent the current climate conditions (PD), with a good correlation and low mean square error values. For paleoreconstructions, even with the low availability of in-situ data to compare, especially for MIS11c, good concordances with other studies were found. Results indicate enhanced cooling in northern North America in the ICE6G compared to the ICE4G simulation due to the lapse rate effect. The decrease of -24°C in the surface temperature in the ICE6G relative to the PD led to a modification of the atmospheric circulation, mainly in the Atlantic and North Pacific region. Significant differences were found in the comparison between two topographies for LGM; ICE6G and ICE4G. Warming of approximately 3 °C in the North Atlantic, as a result of the increased concentration of ice in North America for the ICE6G topography, probably caused by air subsidence to the south and east of the topography anomaly. Positive and negative anomalies vary widely for the Evaporation-Precipitation flow pattern (E - P), with the cooler and drier atmosphere leading to a reduction in LGM precipitation in the regions of Europe. Changes in sea surface temperature and salinity and E - P fluxes lead to changes in the ocean carbonate system, resulting in an overall increase in total alkalinity and a reduction in total dissolved carbon concentrations (TCO₂) in LGM in relation to the PD. This is a consequence of the low concentration of CO₂ and the

increase in calcium carbonate concentrations (CO_2^{3-}) leading to increased oceanic pH. Changes in the intensity of the Meridional Overturning Circulation between the glacial and interglacial periods led to changes in oceanic circulation patterns, decreasing their intensity in the Last Glacial Maximum relative to PD and MIS11c. The response of the biogeochemical cycle to the simulated LGM and MIS11c for the Southern Ocean showed a large increase in surface oxygen from 55 °S and a decrease in western Antarctica (particularly in the Weddell Sea). Analyzes for nitrate (NO_3^-), phosphate (PO_4^{3-}), TCO_2 and total alkalinity (TA) show that they are closely linked to variations in CO_2 concentrations between atmosphere and ocean surface as well as CaCO_3 sedimentation availability

Capítulo 1

Introdução

Nos últimos 2.5 milhões de anos o clima se diversificou em períodos glaciais e interglaciais. Os períodos glaciais são mais frios, substancialmente mais secos e com o aumento dos mantos de gelo em comparação com os períodos interglaciais (Rahmstorf, 2002; Clark et al., 2009; Sigman et al., 2010). Já os períodos interglaciais, são consideravelmente mais quentes e em alguns casos, ocorre a diminuição dos mantos de gelo (Melles et al., 2012; Coletti et al., 2015). As mudanças entre os períodos frios e quentes tem como principais causas: oscilações nas forçantes orbitais e mudanças nas concentrações de CO₂ (Li et al., 1998; Weaver et al., 1998). Estima-se que as concentrações de CO₂ tem variado em cerca de 50-100 ppm durante os períodos glaciais e interglaciais nos últimos 800.000 ky (Bereiter et al., 2015).

Os motivos que promoveram a transição de períodos glaciais para interglaciais não são bem conhecidos. Nesse sentido, variações na topografia do Hemisfério Norte (Peltier, 1994, 2004; Peltier et al., 2015; Argus et al., 2014) e oscilações orbitais (Kutzbach and Guetter, 1986) tem sido apontados como uma das principais causas. Uma das explicações mais aceitáveis sobre a queda abrupta das concentrações de

CO₂ nos períodos glaciais, envolve a biogeoquímica marinha e a sua interação com a circulação oceânica (Sigman and Boyle, 2000), que induzem substanciais alterações na distribuição global dos campos de vento (Toggweiler et al., 2006; Muglia and Schmittner, 2015) e no nível médio dos mares (Kopp et al., 2009; Ren et al., 2017; Glock et al., 2018) e modificações tanto na magnitude, como na profundidade da Corrente de Revolvimento Meridional Global (MOC; (Ganachaud, 2003; Schmittner et al., 2007).

Entre os períodos glaciais, o Último Máximo Glacial (LGM) é considerado com a máxima cobertura de gelo (Lowell et al., 1995). O LGM ocorreu há cerca de 20.000 anos atrás e é considerado o período com menor nível do mar do quaternário, cerca de 135 m abaixo do encontrado hoje. O clima do LGM era seco com formação de grandes desertos, diminuição das florestas e concentrações de CO₂ perto dos 185ppm (Mix et al., 2001; Clark et al., 2009).

Dentre os interglaciais que ocorreram no Pleistoceno, destacam-se os *Marine Isotope Stage* (MIS) 1 (~11 ka BP), 5e (~127 ka BP), 11c (~409 ka AP) e o 31 (~1.072 ka BP), por serem considerados os mais quentes (Melles et al., 2012). O MIS11c foi um interglacial que ocorreu aproximadamente 428-383 kyr (45 mil anos) onde a forçante solar foi a mais longa registrada nos períodos interglaciais e gerou um calor intenso na região do Ártico (Melles et al., 2012). As concentrações de CO₂ eram de aproximadamente 285ppm e vem recebendo atenção por ser possivelmente análogo ao presente e futuras mudanças naturais no clima (Tzedakis, 2010).

Durante os períodos interglaciais essa capacidade dos oceanos em absorver CO₂ é diminuída em relação aos períodos glaciais, isso devido a solubilidade do CO₂ em águas mais frias ser maior (Broecker, 1982). Buchanan et al. (2016) apontam que

a resposta biogeoquímica dos oceanos no LGM, está atrelado com o aumento da salinidade e diminuição da temperatura, levando à um aumento na concentração de nutrientes (ie. nitrato, fosfato, sílica) e da alcalinidade total, reduzindo assim as concentrações de CO₂ atmosférico.

Já Kohfeld et al. (2005), sugere que os processos biológicos nos oceanos contribuem menos do que a metade nas variações das concentrações de CO₂ atmosférico entre os períodos glaciais e interglaciais, estando estes, vinculados à processos físicos de circulação oceânica e formação de massas d'água. Estudos apontam que o aumento da ressurgência no LGM em relação aos períodos interglaciais, levou a um excesso nas concentrações de nutrientes, elevando as condições de alto nitrato - baixa clorofila (em inglês *High-nitrate low-chlorophyll*) (Farrell et al., 1995; Kohfeld et al., 2005).

Desde que o oceano, em razão da sua inércia térmica, atua como regulador do clima terrestre e também como causa da variabilidade natural do clima, a sua maior capacidade de estocar CO₂, promove o equilíbrio das concentrações de CO₂ com a atmosfera em escalas glaciais-interglaciais. Afetando o sistema climático não só através da troca de energia, mas também pelo seu importante papel no ciclo biogeoquímico, mantido pelas trocas gasosas com a atmosfera (Adkins, 2013).

Em resumo, muitas mudanças tem sido observada ao longo dos milhares de anos nas propriedades oceânicas relacionadas com o clima, incluindo mudanças na temperatura, salinidade, nível do mar, pH, concentração de carbono e oxigênio. Esses padrões observados são consistentes com as mudanças na órbita da Terra e nas concentrações de CO₂. Então, descobrir e entender as relações entre o clima e as relações ecossistêmicas do passado é de fundamental importância para se en-

tender e possivelmente prever as mudanças no clima futuro. Além disso, as atuais preocupações com o aumento das concentrações de gases do efeito estufa, em especial o CO₂ e seu efeito principalmente nos oceanos, tem alavancado um leque de pesquisas sobre o tema. Assim, os estudos de climas extremos do passado, tem um importante papel no entendimento da variabilidade natural do clima e a sensibilidade dos modelos às forçantes climáticas.

Na tentativa de se entender melhor as condições climáticas do Último Máximo Glacial e a sua relação com o ciclo biogeoquímico do carbono oceânico, utilizou-se estudar o efeito direto da influência de diferentes topografias do LGM. Foi proposto então, disponibilizar um estudo sobre o ciclo biogeoquímico marinho, principalmente com o aprimoramento da inserção da nova topografia disponível por [Argus et al. \(2014\)](#); [Peltier et al. \(2015\)](#) ICE6G do período do LGM em um modelo climático do sistema terrestre. Assim como, procurou-se compreender o comportamento do Oceano Austral frente à dois extremos climáticos; o Último Máximo Glacial (com a topografia ICE6G) e o interglacial MIS11c. O MIS11c é um interglacial ainda pouco estudado, principalmente em suas feições climáticas oceânicas.

1.1 Apresentação da Tese

Foi utilizado para esse estudo o modelo físico - biogeoquímico UVic ESCM (2.9 ([Weaver et al., 1998](#); [Eby et al., 2013](#)) objetivando entender os diferentes processos que levaram à mudanças no ciclo biogeoquímico oceânico em duas diferentes eras, o MIS11c e o LGM. Seguindo a Introdução, apresenta-se os objetivos, a fundamentação teórica, a descrição o modelo UVic ESCM, os artigos submetidos e as

conclusões gerais com as limitações e as perspectivas futuras.

1.2 Objetivos

O objetivo geral desse trabalho é estudar o comportamento do ciclo biogeoquímico dos oceanos de acordo com as mudanças orbitais, concentração do CO₂ e topografia do Último Máximo Glacial. Foco também é dado ao entendimento do clima e do ciclo biogeoquímico marinho do carbono durante o *Marine Isotope Stage* 11c.

1.2.1 Objetivos Específicos

Esse trabalho teve como objetivos específicos:

1) Analisar as diferenças do impacto das diferentes topografias para o clima do LGM; ICE4G (Peltier, 1994), ICE5G (Peltier, 2004) e ICE6G (Argus et al., 2014; Peltier et al., 2015); e como os oceanos reagem à essas diferenças.

2) Investigar o impacto da forçante orbital e da concentração do CO₂ no Inter-glacial *Marine Isotope Stage* 11c no Oceano Austral.

1.3 Fundamentação Teórica

1.3.1 Forçantes Orbitais e Mudanças Climáticas

A principal evidência que relaciona o clima da Terra às alterações nas forçantes orbitais são provenientes de registros marinhos sedimentares de foraminíferos, a partir de isótopos de oxigênio. As flutuações nos registros são em grande parte, devido ao crescimento/diminuição do volume de gelo e da temperatura oceânica

(Shackleton and Pisias, 2013; Broecker, 1986). O clima da Terra é dirigido tanto por forçantes internas como externas, como os parâmetros orbitais de Milankovitch, que considera as mudanças orbitais da Terra.

A Teoria de Milankovitch (Berger, 1980), estabelece que as variações da órbita e da rotação da Terra controlam a intensidade dos efeitos da insolação de acordo com a latitude, divididos em: Excentricidade, Obliquidade e Precessão (Figura 1.1).

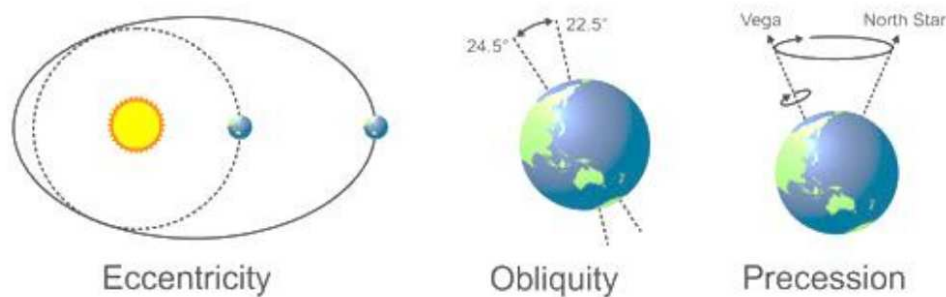


Figura 1.1: Ciclos de Milankovitch. Adaptada de Zachos et al. (2001).

A excentricidade da órbita da Terra ao redor do Sol oscila entre elíptica e quase circular em um período de aproximadamente 100.000 anos (Figura 1.1). Seu valor atual está ao redor 0.0167, no entanto, varia entre 0.0034 e 0.058. Essas oscilações, de mais elíptica para circular, são de fundamental importância para os processos de glaciação, alterando a distância entre o Sol e a Terra. Aumentando ou diminuindo a distância em que a radiação de ondas curtas, proveniente do Sol, percorre para chegar à Terra reduzindo ou aumentando a quantidade de radiação recebida na superfície em diferentes estações do ano.

O ciclo de obliquidade está relacionado com o ângulo entre o seu eixo rotacional e o seu eixo orbital (eixo perpendicular a eclíptica) (Figura 1.1). Oscila em aproximadamente a cada 41 mil anos, e está relacionado com a inclinação do eixo da Terra, sendo o seu efeito maior nas regiões polares. Seu valor atual é de 23,4°,

variando entre 22° e 24.5° . A menor inclinação do eixo resulta em uma distribuição mais uniforme da radiação solar entre o inverno e o verão, no entanto, aumenta a diferença entre as regiões polares e equatoriais.

Já o ciclo da precessão, cujo o período é de cerca de 22 mil anos, leva a variações na distância entre a Terra e o Sol, sendo esta maior no Equador e menor nos polos. A precessão é a lenta oscilação da Terra em torno do seu eixo, devido a rotação da Terra, o eixo terrestre não se alinha à eclíptica, precessiona em torno dele, variando a sua direção entre as estrelas Polaris e Vega (Figura 1.1). O ciclo da precessão leva à um deslocamento dos equinócios, conhecido como precessão dos equinócios. Atualmente a Terra está mais próxima ao sol em janeiro e mais afastada em julho e o inverso deve ocorrer em aproximadamente 11.000 anos.

1.3.2 Períodos Glaciais e Interglaciais

O principal mecanismo forçado pelos parâmetros orbitais é a quantidade de insolação recebida pela Terra. Se a insolação no verão for maior (menor) o derretimento das calotas de gelo deverá ser maior (menor). O menor grau de obliquidade resulta em um inverno mais quente e um verão mais frio, no qual, o ar mais aquecido no inverno, é capaz de reter mais umidade e produzir mais neve, e o verão menos frio resulta em uma diminuição do derretimento de gelo. Essa combinação leva à uma era glacial, devido ao feedback do albedo do gelo, levando à um maior crescimento dos mantos de gelo. O inverso também é verdadeiro, se existe um contraste entre as estações, inverno mais frio e verão mais quente, leva a redução do volume de gelo, com o conseqüente aquecimento, encaminhando para um período interglacial (Hartmann, 2015).

Acredita-se que uma mudança na distribuição sazonal da radiação solar, induzida por parâmetros orbitais seja responsável pelo início do Último Máximo Glacial (*Last Glacial Maximum*) aqui referido como LGM. No entanto, os valores dos parâmetros orbitais do LGM não eram tão diferentes dos valores atuais (Tabela 1.1, adaptada do *Paleoclimate Modelling Intercomparison Project - PMIP*). De acordo com Broccoli and Manabe (1987), apenas as variações nos parâmetros orbitais não podem explicar o clima do LGM e sim a junção com outros fatores físicos. A redução drástica da concentração do CO₂ atmosférico de cerca de 100 ppm do que no período pré-Industrial, aparece como sendo uma das principais forçantes responsáveis pelo resfriamento do LGM (Raynaud et al. 1983).

Tabela 1.1: Parâmetros orbitais para o LGM e para a era pré-industrial (adaptada do *Paleoclimate Modelling Intercomparison Project – PMIP*)

	LGM	Pré-Industrial
Excentricidade	0.018994	0.016724
Obliquidade	22.949°	23.446°
Precessão	114.42°	102.04°
CO ₂	185 ppm	280 ppm

A principal característica do LGM foi à formação de grandes mantos de gelo sobre os continentes e os oceanos, que cobriram grande parte do Hemisfério Norte, como a América do Norte, norte da Europa e Ásia, promovendo grandes alterações do clima na Terra na época, como secas, desertificações e uma drástica queda no nível médio dos mares. As maiores mudanças foram encontradas no Hemisfério Norte, onde a cobertura de gelo proporcionou uma migração da frente oceânica polar e grandes blocos de gelo para o Equador, chegando em aproximadamente 45°N,

coabrindo praticamente todo o atlântico norte nas altas latitudes durante o inverno. Resultou em uma vasta região da superfície terrestre coberta por gelo e tundra (120°W a 90°E e ao norte de 45°N), alterando significativamente a temperatura em todo o planeta.

Estudos com a utilização de modelagem numérica acoplados atmosfera-oceano, para reconstruir as condições de contorno do LGM realizados por [Yanase and Abe-Ouchi \(2007\)](#); [Clark et al. \(2009\)](#); [Chavaille et al. \(2013\)](#), apontam a maior forçante para o balanço de energia no topo da atmosfera foi o decréscimo da concentração de CO₂ , de 300 ppm para 200 ppm , enquanto que a menor contribuição veio da mudança do albedo das áreas continentais não cobertas por neve. [Weaver et al. \(1998\)](#); [Shin et al. \(2003\)](#) mostraram que houve um resfriamento moderado de 3°C sobre o continente e de 2°C sobre os oceanos e nos sub-trópicos, um resfriamento de 2 a 2.5°C; em latitudes médias uma redução de 8°C. A circulação termohalina no LGM foi mais rasa e mais fraca do que a encontrada atualmente e a circulação de Hadley foi fortalecida em razão do maior gradiente meridional de temperatura, assim como o transporte meridional de calor.

Dentre os interglaciais que ocorreram no Pleistoceno, destacam-se os *Marine Isotope Stage* (MIS) 1 (~11 ka AP), 5e (~127 ka AP), 11c (~409 ka AP) e o 31 (~1.072 ka AP), por serem considerados os mais quentes ([Melles et al., 2012](#)). O MIS11c foi consideravelmente o mais longo entre eles (~ 380 e 423 ka), e é caracterizado pela baixa excentricidade e obliquidade. Foi marcado por intensas anomalias de insolação no verão (comparadas ao período pré-industrial) em torno de +45 55Wm² , levando à um intenso aquecimento em todo o Ártico ([Melles et al., 2012](#); [Coletti et al., 2015](#)). As concentrações de CO₂ eram de aproximadamente 285ppm e vem

recebendo atenção por ser possivelmente análogo ao presente e futuras mudanças naturais no clima (Tzedakis, 2010). Evidências apontam uma redução na espessura de gelo na Groelândia (Melles et al., 2012; Raymo and Mitrovica, 2012; Coletti et al., 2015).

Tabela 1.2: Parâmetros orbitais para o MIS11c e para a era pré-industrial (adaptada de Melles et al. (2012); Raymo and Mitrovica (2012)

	MIS11c	Pré-Industrial
Excentricidade	0.01932	0.016724
Obliquidade	23.78°	23.446°
om Precessão	277.67°	102.04°
[CO2]	285ppm	280 ppm

O MIS11c foi identificado através de registros sedimentares do Lago El'gygytgyn, situado no extremo nordeste da Sibéria, cerca de 100km do círculo do Ártico, criado a partir da queda de um meteorito de 3.6 Ma \pm 0.04 Ma atrás (Layer, 2000) e contem os mais longos registros terrestres do clima do Ártico, devido a sua bacia nunca ter sido coberta por calotas de gelo do Quaternário (Melles et al., 2012; Coletti et al., 2015). As análises das reconstruções do Lago El'gygytgyn apontam que os valores precipitação e da temperatura eram de 5°C e 300mm respectivamente superiores aos do encontrado no Holoceno (Melles et al., 2012; Coletti et al., 2015). Melles et al. (2012) inferiram que devido o recuo do gelo do oeste da Antártica (*West Antarctic Ice Sheet*; WEIS) possibilitou perturbações na circulação termohalina com significativa mudança no nível médio dos mares, ampliando assim o extremo e prolongado aquecimento no Ártico durante o MIS11c.

1.3.3 Ciclo do Carbono nos Oceanos

A assimilação de como o carbono se comporta quando é absorvido ou liberado dos oceanos, é a base fundamental para o entendimento das variações do sistema carbonático oceânico em diferentes escalas de tempo. Ele é caracterizado por uma série de equilíbrios, descritos abaixo.

Assim que o CO_2 é absorvido na água do mar ele forma o composto H_2CO_3 que por sua vez depende da constante de dissociação (K_1), liberando íons de H^+ e de bicarbonato (HCO_3^-), se dissociando novamente de acordo com a constante K_2 em íons de 2H^+ e carbonato (CO_3^{2-}) (eq. 3.1.) As constantes de dissociação K_1 e K_2 são dependentes na temperatura e salinidade (Millero, 1979).



Variações nas $p\text{CO}_2$ na superfície dos oceanos são determinadas pela temperatura da superfície do mar (SST), salinidade (SSS), carbono inorgânico dissolvido (TCO_2 , soma dos compostos inorgânicos como: H_2CO_3 , HCO^- e CO_3^{2-}) e alcalinidade (TA) e estão descritos na equação 1.2.

$$p\text{CO}_2 \sim \frac{K_2}{K_0 K_1} \frac{(2\text{TCO}_2 - \text{TA})^2}{\text{TA} - \text{TCO}_2} \quad (1.2)$$

Onde K_0 é a constante de solubilidade do CO_2 . As concentrações de TA são dependentes apenas da bomba biológica, enquanto que o TCO_2 depende também da bomba de solubilidade.

Variações nessas propriedades, e portanto na $p\text{CO}_2$, são derivadas da interação

de processos físicos, químicos e biológicos. Esses mecanismos são conhecidos como bombas de carbono ("*Carbon Pumps*"), que desempenham um papel fundamental na redistribuição do carbono entre a superfície e o fundo marinho. As bombas de carbono são divididas em 2; Bomba Biológica e a Bomba de Solubilidade. A Bomba Biológica, engloba as bombas do carbonato e a microbiológica e são influenciadas pela disponibilidade de luz, nutrientes e produção primária. A bomba de solubilidade envolve diferenças de temperatura, salinidade e cobertura de gelo (Toggweiler et al., 2003).

A troca de CO_2 depende da diferença de $p\text{CO}_2$ entre a atmosfera e os oceanos. A $p\text{CO}_2$ oceânica por sua vez, depende do TCO_2 e da TA (Eq. 1.2). As bombas de carbono então, tem a função transportar o carbono orgânico (C_{org}) e o carbonato de cálcio (CaCO_3), do momento da produção na superfície para as camadas mais profundas dos oceanos, onde eles irão remineralizar lentamente e se dissolver. Ambas as bombas alteram as concentrações de TCO_2 e de TA na superfície oceânica, afetando assim a $p\text{CO}_2$ (Jansen, 2017).

Os efeitos das bombas de carbono sobre o sistema carbonato dos oceanos, podem ser descritos em termos das variações de TA e TCO_2 (Figura 3.12). O (C_{org}) que é produzido na superfície pela fotossíntese, é exportado para o fundo oceânico, assim como o CaCO_3 , produzido por organismos calcários. O C_{org} e CaCO_3 possuem efeitos opostos; enquanto que o C_{org} remove o TCO_2 , o pH e as concentrações de CO_3^{2-} aumentam, ao mesmo tempo que a $p\text{CO}_2$ diminui nas águas superficiais. O CaCO_3 por outro lado, remove a TA, diminui o pH e as concentrações de CO_3^{2-} , elevando assim a $p\text{CO}_2$ da superfície oceânica. A maior dissolução do CaCO_3 do que a sua formação, provoca o aumento do pH, a diminuição da $p\text{CO}_2$ em super-

fície, aumentando assim a capacidade dos oceanos em absorver CO_2 atmosférico (Zeebe and Wolf-Gladrow, 2001).

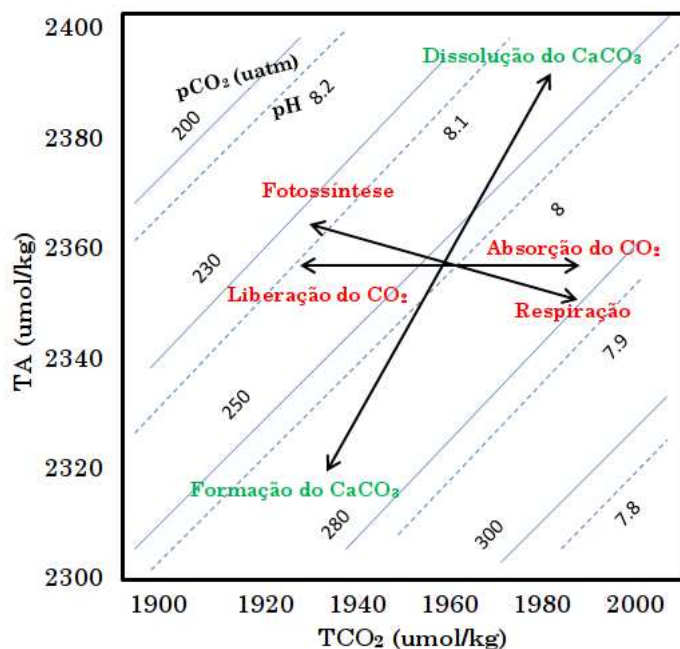


Figura 1.2: Efeito da formação e dissolução do CaCO_3 na alcalinidade total, TCO_2 e na $p\text{CO}_2$ oceânica. Adaptada de (Zeebe and Wolf-Gladrow, 2001; Sigman and Boyle, 2000).

As concentrações de TCO_2 e TA no oceano profundo, também são afetadas pela precipitação do CaCO_3 , resultando na diminuição das concentrações de CO_3^{2-} . Esse processo, está relacionado com a produção de carbono orgânico na superfície que libera TCO_2 através da atividade microbológica nos processos de oxidação (Volk and Hoffert, 1985). Todos esses processos então, afetam as taxas de deposição do CaCO_3 no sedimento oceânico, que por sua vez, altera a capacidade dos oceanos de absorver ou liberar CO_2 da/para atmosfera (seta horizontal).

Todas as bombas de carbono são sensíveis as mudanças climáticas em diferentes graus e aspectos, sendo um dos mecanismos mais importantes para se explicar as oscilações de $p\text{CO}_2$ durante as eras glaciais/interglaciais (Reid et al., 2009; Sigman and Boyle, 2000; Sigman et al., 2010).

1.4 Descrição do Modelo

1.4.1 UVic ESCM

A maioria dos modelos climáticos do sistema terrestre (ESCM), possuem uma arquitetura única para todas as suas componentes, em diferentes processos de acoplamento, no entanto, torna os modelos menos independentes. Algumas interfaces novas dos modelos do sistema climático terrestre faz uso de acopladores, podendo assim ser utilizado em vários processos de modelagem e em vários grupos, como é o caso do Uvic ESCM (Fig. 1.3).

O UVic ESCM (University of Victoria – Earth System Climate Model; [Weaver et al., 1998](#)), é um modelo de complexidade intermediária do sistema climático terrestre. Inclui em suas componentes (Fig. 1.3) um modelo de circulação geral oceânica 3D baseado na versão 2 do “*Modular Ocean Model*” ([Griffies et al., 2004](#)) com 19 níveis verticais de profundidade, onde a difusividade vertical do oceano é parametrizada globalmente em um perfil uniforme seguindo ([Bryan and Lewis, 1979](#)). Os vórtices, difusividade, linhas isopícnas e espessura oceânica, são parametrizações Gent-McWilliams ([Gent et al., 1995](#)). Este é acoplado ao modelo de superfície terrestre, modelo de gelo marinho dinâmico e termodinâmico e um modelo simplificado de balanço energético atmosférico de uma camada ([Eby et al., 2013](#)).

O modelo atmosférico incorpora as equações do balanço de energia e umidade, permitindo calcular os efeitos do transporte de calor latente e sensível ([Fanning and Weaver, 1996](#)). A componente de gelo marinho é a representação padrão da termodinâmica do gelo marinho com crescimento lateral e parametrização de der-

retimento de (Hibler, 1979). A componente assume que o gelo não capacidade para armazenar calor e a temperatura de superfície é balanceada diretamente com a forçante externa, incluindo também o modelo de dinâmica de gelo continental (*Continental Ice Dynamics Model; CIDM* (Marshall and Clarke, 1997a,b))

O UVic ESCM contem a completa representação dos ciclos do carbono tanto oceânico como terrestre. O ciclo do carbono terrestre é simulado usando o modelo de vegetação *Top-down Representation of Interactive Foliage and Flora Including Dynamics* (TRIFFID; (Meissner et al., 2003)). O modelo inclui o prognóstico geral do carbono armazenado no *permafrost* em que o carbono do solo é difundido lentamente dentro das camadas de solo congeladas durante o ano (MacDougall, 2017).

O ciclo do carbono inorgânico do oceano é simulado seguindo os protocolos do Ocean Carbon Cycle Model Intercomparison Project (OCMIP; (Orr and Epitalon, 2015)). O modelo do ecossistema oceânico é um aprimoramento do modelo de nutriente-fitoplâncton-zooplâncton-detritos (NPZD; (Schmittner and Galbraith, 2008a), parametrizações de rápida reciclagem dos nutrientes através de atividade microbológica (Schartau and Oschlies, 2004). Inclui também duas classes de fitoplâncton, os fixadores de nitrogênio e outros, ciclo do Nitrato, Fosfato, Oxigênio, Carbono Inorgânico Dissolvido, alcalinidade e também de outros traçadores, além de modular e calcular a contribuição da bomba biológica na biogeoquímica oceânica (Schartau and Oschlies, 2004; Schmittner and Galbraith, 2008b).

Os processos que ocorrem nos sedimentos são representados usando apenas o modelo óxico de respiração nos sedimentos (Archer et al., 2000). A versão 2.9 do UVic ESCM (Eby et al., 2013) inclui também a representação do reservatório de

carbono *permafrost*, englobando uma coluna de solo profundo de até 250 m de profundidade e também com a física completa do processo gelo - degelo (MacDougall et al., 2017).

O UVic ESCM incorpora o carbono oceânico e o terrestre em um modelo de circulação geral atmosférico e oceânico (Fig. 1.3), a fim de representar as interações físicas, químicas e biológicas no *feedback* do ciclo do carbono no sistema físico climático. Os principais aspectos a serem analisados da saída do UVic que foram considerados nesse trabalho estão relacionados com os processos oceânicos, principalmente os processos de captura do CO₂ que interferem na distribuição vertical desse carbono dissolvido nos oceanos, associados as diferentes circulações do vento, correspondente aos períodos do MIS11c e do LGM, a fim de se estudar as componentes das bombas do carbono.

Muitos pesquisadores e centros de pesquisa, tem usado atualmente o modelo Uvic ESCM a fim de identificar padrões do ciclo do carbono (Montenegro et al., 2007; Matthews et al., 2009), efeitos do aumento das concentrações de CO₂ (Weaver et al., 2007; Zickfeld et al., 2011; Eby et al., 2013), reconstrução de períodos do passado (Ewen et al., 2004; Meissner et al., 2003, 2012; Montenegro et al., 2007; Muglia and Schmittner, 2015; Muglia et al., 2018; Schmitt, 2011), acidificação oceânica (Matthews et al., 2009; Meissner et al., 2012), bombas de carbono (Matthews, 2006; Brovkin et al., 2007; Keller et al., 2012; Thibodeau et al., 2018).

Sabe-se ainda também que as incertezas nos dados observados de nutrientes dos oceanos são relativamente grandes, principalmente porque existe uma quantidade limitada de dados dos fluxos biogeoquímicos oceânicos, gerando possíveis vieses devido a incerteza das extrapolações dos dados de sedimento profundo dos

oceanos. Os valores dos fluxos globais de nutrientes simulados pelo UVic ESCM estão bem próximos das estimativas observacionais, sugerindo que o modelo reproduz satisfatoriamente os processos das bombas de carbono global, associados aos modelos de nutrientes (Keller et al., 2012).

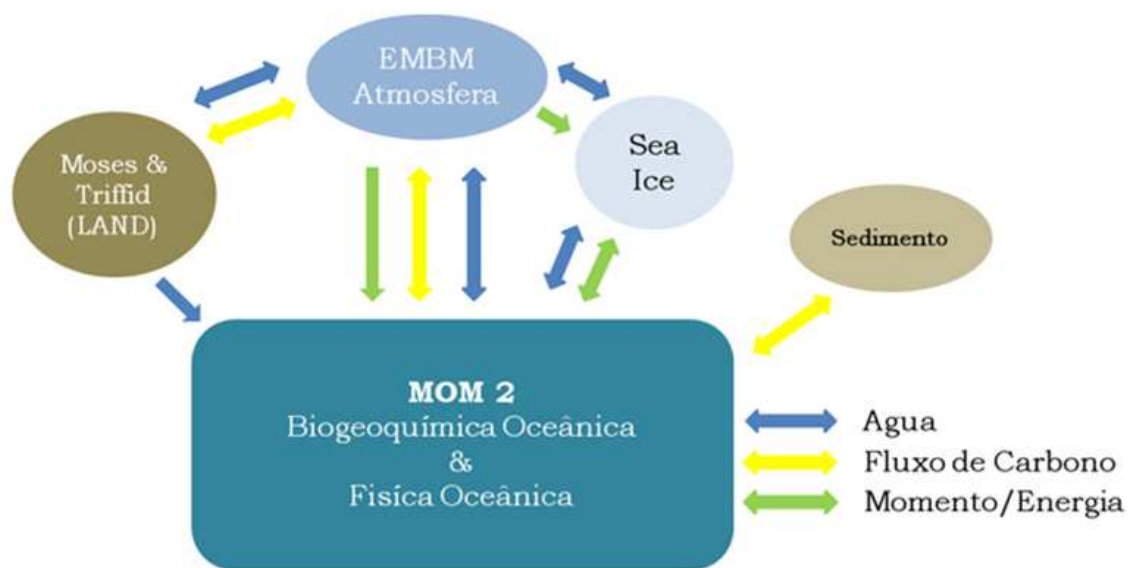


Figura 1.3: Fluxograma do UVic ESCM, com cada componente climático associado ao acoplador; oceano, sedimento, terrestre, atmosfera e gelo marinho. Os fluxos são representados pelas setas e as cores apontam de onde são originados. O tamanho dos círculos representam o tamanho relativo do código base. Adaptado de (Wania et al., 2012)

Afim de analisar o clima e o ciclo biogeoquímico no LGM e no MIS11c, 5 experimentos (Tab. 1.3) foram conduzidos. No total, foram modelados 53.000 anos com duração de aproximadamente 2 anos de dedicação. A simulação do dias atuais, com concentração de CO₂ da ordem de 380 ppm é uma simulação secundária a partir da simulação controle.

Tabela 1.3: Sumário das simulações.

Simulações		
	Condições Iniciais	Anos do Modelo
Controle	Pré-Industriais	10.000
Dias Atuais	CO ₂ (380ppm)	3.000
MIS11c	CO ₂ (285ppm)	10.000
LGM4G	ICE4G topografia	10.000
LGM5G	ICE5G topografia	10.000
LGM6G	ICE6G topografia	10.000

Referências Bibliográficas

- Adkins, J. F. (2013). The role of deep ocean circulation in setting glacial climates. *Paleoceanography*, 28(3):539–561.
- Archer, D. E., Eshel, G., Winguth, A., Broecker, W., Pierrehumbert, R., Tobis, M., and Jacob, R. (2000). Atmospheric pCO₂ sensitivity to the biological pump in the ocean. *Global Biogeochemical Cycles*, 14(4):1219–1230.
- Argus, D. F., Peltier, W. R., Drummond, R., and Moore, A. W. (2014). The Antarctica component of postglacial rebound model ICE-6G_C (VM5a) based on GPS positioning, exposure age dating of ice thicknesses, and relative sea level histories. *Geophysical Journal International*, 198(1):537–563.
- Bereiter, B., Eggleston, S., Schmitt, J., Nehrbass-Ahles, C., Stocker, T. F., Fischer, H., Kipfstuhl, S., and Chappellaz, J. (2015). Revision of the EPICA Dome C CO₂ record from 800 to 600 kyr before present. *Geophysical Research Letters*, 42(2):542–549.

- Berger, A. (1980). The Milankovitch astronomical theory of paleoclimates: A modern review. *Vistas in Astronomy*, 24:103–122.
- Broccoli, A. J. and Manabe, S. (1987). The influence of continental ice, atmospheric CO₂, and land albedo on the climate of the last glacial maximum. *Climate Dynamics*, 1(2):87–99.
- Broecker, W. S. (1982). Glacial to interglacial changes in ocean chemistry. *Progress in Oceanography*, 11(2):151–197.
- Broecker, W. S. (1986). Oxygen isotope constraints on surface ocean temperatures. *Quaternary Research*, 26(1):121–134.
- Brovkin, V., Ganopolski, A., Archer, D., and Rahmstorf, S. (2007). Lowering of glacial atmospheric CO₂ in response to changes on oceanic circulation and marine biogeochemistry. *Paleoceanography*, 22(4):1–14.
- Bryan, K. and Lewis, L. J. (1979). A water mass model of the World Ocean. *Journal of Geophysical Research*, 84(C5):2503.
- Buchanan, P. J., Matear, R. J., Lenton, A., Phipps, S. J., Chase, Z., and Etheridge, D. M. (2016). The simulated climate of the Last Glacial Maximum and insights into the global marine carbon cycle. *Climate of the Past*, 12(12):2271–2295.
- Chavaillaz, Y., Codron, F., and Kageyama, M. (2013). Southern westerlies in LGM and future (RCP4.5) climates. *Climate of the Past*, 9(2):517–524.
- Clark, P. U., Dyke, A. S., Shakun, J. D., Carlson, A. E., Clark, J., Wohlfarth, B., Mitrovica, J. X., Hostetler, S. W., and McCabe, A. M. (2009). The Last Glacial Maximum. *Science*, 325(5941):710–714.

- Coletti, A. J., DeConto, R. M., Brigham-Grette, J., and Melles, M. (2015). A GCM comparison of Pleistocene super-interglacial periods in relation to Lake El'gygytgyn, NE Arctic Russia. *Climate of the Past*, 11(7):979–989.
- Eby, M., Weaver, A. J., Alexander, K., Zickfeld, K., Abe-Ouchi, A., Cimadoribus, A. A., Crespin, E., Drijfhout, S. S., Edwards, N. R., Eliseev, A. V., Feulner, G., Fichefet, T., Forest, C. E., Goosse, H., Holden, P. B., Joos, F., Kawamiya, M., Kicklighter, D., Kienert, H., Matsumoto, K., Mokhov, I. I., Monier, E., Olsen, S. M., Pedersen, J. O., Perrette, M., Philippon-Berthier, G., Ridgwell, A., Schlosser, A., Von Deimling, T. S., Shaffer, G., Smith, R. S., Spahni, R., Sokolov, A. P., Steinacher, M., Tachiiri, K., Tokos, K., Yoshimori, M., Zeng, N., and Zhao, F. (2013). Historical and idealized climate model experiments: An intercomparison of Earth system models of intermediate complexity. *Climate of the Past*, 9(3):1111–1140.
- Ewen, T. L., Weaver, A. J., and Eby, M. (2004). Sensitivity of the inorganic ocean carbon cycle to future climate warming in the UVic coupled model. *Atmosphere - Ocean*, 42(1):23–42.
- Fanning, A. F. and Weaver, A. J. (1996). An atmospheric energy-moisture balance model: Climatology, interpentadal climate change, and coupling to an ocean general circulation model. *Journal of Geophysical Research: Atmospheres*, 101(D10):15111–15128.
- Farrell, J. W., Pedersen, T. F., Calvert, S. E., and Nielsen, B. (1995). Glacial–interglacial changes in nutrient utilization in the equatorial Pacific Ocean. *Nature*, 377(6549):514–517.

- Ganachaud, A. (2003). Large-scale mass transports, water mass formation, and diffusivities estimated from World Ocean Circulation Experiment (WOCE) hydrographic data. *Journal of Geophysical Research*, 108(C7).
- Gent, P. R., Willebrand, J., McDougall, T. J., and McWilliams, J. C. (1995). Parameterizing Eddy-Induced Tracer Transports in Ocean Circulation Models. *Journal of Physical Oceanography*, 25(4):463–474.
- Glock, N., Erdem, Z., Wallmann, K., Somes, C. J., Liebetrau, V., Schönfeld, J., Gorb, S., and Eisenhauer, A. (2018). Coupling of oceanic carbon and nitrogen facilitates spatially resolved quantitative reconstruction of nitrate inventories. *Nature Communications*, 9(1):1–10.
- Griffies, S. M., Harrison, M. J., Pacanowski, Ronald, C., and Rosati, A. (2004). A Technical Guide to MOM4, GFDL OCEAN GROUP TECHNICAL REPORT NO. 5. NOAA/Geophysical Fluid Dynamics Laboratory, page Available online at www.gfdl.noaa.gov.
- Hartmann, D. L. (2015). *Global physical climatology: Second Edition*. Elsevier Science.
- Hibler, W. D. (1979). A Dynamic Thermodynamic Sea Ice Model. *Journal of Physical Oceanography*, 9(4):815–846.
- Jansen, M. F. (2017). Glacial ocean circulation and stratification explained by reduced atmospheric temperature. *Proceedings of the National Academy of Sciences*, 114(1):45–50.
- Justino, F., Timmermann, A., Merkel, U., and Souza, E. P. (2005). Synoptic reorga-

- nization of atmospheric flow during the last glacial maximum. *Journal of Climate*, 18(15):2826–2846.
- Kageyama, M., Merkel, U., Otto-Bliesner, B., Prange, M., Abe-Ouchi, A., Lohmann, G., Ohgaito, R., Roche, D. M., Singarayer, J., Swingedouw, D., and Zhang, X. (2013). Climatic impacts of fresh water hosing under last glacial Maximum conditions: A multi-model study. *Climate of the Past*, 9(2):935–953.
- Keller, D. P., Oschlies, A., and Eby, M. (2012). A new marine ecosystem model for the University of Victoria earth system climate model. *Geoscientific Model Development*, 5(5):1195–1220.
- Kohfeld, K., Quéré1, C. L., Harrison1, S. P., and Anderson, R. F. (2005). Role of Marine Biology in Glacial-Interglacial CO₂ Cycles. *Science*, 308(5718):74–78.
- Kopp, R. E., Simons, F. J., Mitrovica, J. X., Maloof, A. C., and Oppenheimer, M. (2009). Probabilistic assessment of sea level during the last interglacial stage. *Nature*, 462(7275):863–867.
- Kutzbach, J. E. and Guetter, P. J. (1986). The Influence of Changing Orbital Parameters and Surface Boundary Conditions on Climate Simulations for the Past 18 000 Years. *Journal of the Atmospheric Sciences*, 43(16):1726–1759.
- Layer, P. W. (2000). Argon-40/argon-39 age of the El'gygytgyn impact event, Chukotka, Russia. *Meteoritics and Planetary Science*, 35(3):591–599.
- Li, X. S., Berger, A., Loutre, M. F., Haug, G. H., Tiedemann, R., Maslin, M. A., Haug, G. H., and Tiedemann, R. (1998). Simulating late Pliocene Northern Hemisphere climate decreasing. *Hemisphere*, 25(6):915–918.

- Lowell, T. V., Heusser, C. J., Andersen, B. G., Moreno, P. I., Hauser, A., Heusser, L. E., Schluchter, C., Marchant, D. R., and Denton, G. H. (1995). Interhemispheric Correlation of Late Pleistocene Glacial Events. *Science*, 269(5230):1541–1549.
- MacDougall, A. H. (2017). The oceanic origin of path-independent carbon budgets. *Scientific Reports*, 7(1):1–12.
- MacDougall, A. H., Swart, N. C., and Knutti, R. (2017). The Uncertainty in the Transient Climate Response to Cumulative CO₂ Emissions Arising from the Uncertainty in Physical Climate Parameters. *Journal of Climate*, 30(2):813–827.
- Marshall, S. J. and Clarke, G. K. C. (1997a). A continuum mixture model of ice stream thermomechanics in the Laurentide Ice Sheet 1. Theory. *Journal of Geophysical Research: Solid Earth*, 102(B9):20599–20613.
- Marshall, S. J. and Clarke, G. K. C. (1997b). A continuum mixture model of ice stream thermomechanics in the Laurentide Ice Sheet 2. Application to the Hudson Strait Ice Stream. *Journal of Geophysical Research: Solid Earth*, 102(B9):20615–20637.
- Matthews, H. D. (2006). Emissions targets for CO₂ stabilization as modified by carbon cycle feedbacks. *Tellus, Series B: Chemical and Physical Meteorology*, 58(5):591–602.
- Matthews, H. D., Gillett, N. P., Stott, P. A., and Zickfeld, K. (2009). The proportionality of global warming to cumulative carbon emissions. *Nature*, 459(7248):829–832.

- Meissner, K. J., Lippmann, T., and Gupta, A. S. (2012). Large-scale stress factors affecting coral reefs: Open ocean sea surface temperature and surface seawater aragonite saturation over the next 400 years. *Coral Reefs*, 31(2):309–319.
- Meissner, K. J., Weaver, A. J., Matthews, H. D., and Cox, P. M. (2003). The role of land surface dynamics in glacial inception: A study with the UVic Earth System Model. *Climate Dynamics*, 21(7-8):515–537.
- Melles, M., Brigham-Grette, J., Minyuk, P. S., Nowaczyk, N. R., Wennrich, V., DeConto, R. M., Anderson, P. M., Andreev, A. A., Coletti, A., Cook, T. L., Haltia-Hovi, E., Kukkonen, M., Lozhkin, A. V., Rosen, P., Tarasov, P., Vogel, H., and Wagner, B. (2012). 2.8 Million Years of Arctic Climate Change from Lake El'gygytgyn, NE Russia. *Science*, 337(6092):315–320.
- Millero, F. J. (1979). The thermodynamics of the carbonate system in seawater. *Geochimica et Cosmochimica Acta*, 43(10):1651–1661.
- Mix, A. C., Bard, E., and Schneider, R. (2001). Environmental processes of the ice age: Land, oceans, glaciers (EPILOG). *Quaternary Science Reviews*, 20(4):627–657.
- Montenegro, A., Brovkin, V., Eby, M., Archer, D., and Weaver, A. J. (2007). Long term fate of anthropogenic carbon. *Geophysical Research Letters*, 34(19):1–5.
- Muglia, J. and Schmittner, A. (2015). Glacial Atlantic overturning increased by wind stress in climate models. *Geophysical Research Letters*, 42(22):9862–9869.
- Muglia, J., Skinner, L. C., and Schmittner, A. (2018). Weak overturning circulation and high Southern Ocean nutrient utilization maximized glacial ocean carbon. *Earth and Planetary Science Letters*, 496:47–56.

- Orr, J. C. and Epitalon, J. M. (2015). Improved routines to model the ocean carbonate system: Mocsy 2.0. *Geoscientific Model Development*, 8(3):485–499.
- Peltier, W. (2004). GLOBAL GLACIAL ISOSTASY AND THE SURFACE OF THE ICE-AGE EARTH: The ICE-5G (VM2) Model and GRACE. *Annual Review of Earth and Planetary Sciences*, 32(1):111–149.
- Peltier, W. R. (1994). Ice Age Paleotopography. *Science*, 265(5169):195–201.
- Peltier, W. R., Argus, D. F., Drummond, R., Strange, A., Peltier, W. R., Argus, D. F., Drummond, R., Shahnas, M. H., Yuen, D. A., Pysklywec, R. N., Peltier, W. R., Argus, D. F., Drummond, R., Tarayoun, A., Audet, P., Mazzotti, S., Ashoori, A., Peltier, W. R., Argus, D. F., and Drummond, R. (2015). Journal of Geophysical Research : Solid Earth. *Journal of Geophysical Research: Solid Earth*, 2015(120):450–487.
- Rahmstorf, S. (2002). Ocean circulation and climate during the past 120,000 years. *Nature*, 419(6903):207–214.
- Raymo, M. E. and Mitrovica, J. X. (2012). Collapse of polar ice sheets during the stage 11 interglacial. *Nature*, 483(7390):453–456.
- Reid, P. C., Fischer, A. C., Lewis-Brown, E., Meredith, M. P., Sparrow, M., Anderson, A. J., Antia, A., Bates, N. R., Bathmann, U., Beaugrand, G., Brix, H., Dye, S., Edwards, M., Furevik, T., Gangstø, R., Hátún, H., Hopcroft, R. R., Kendall, M., Kasten, S., Keeling, R., Le Quéré, C., Mackenzie, F. T., Malin, G., Mauritzen, C., Ólafsson, J., Paull, C., Rignot, E., Shimada, K., Vogt, M., Wallace, C., Wang, Z.,

- and Washington, R. (2009). Chapter 1 Impacts of the Oceans on Climate Change. In *Advances in Marine Biology*, volume 56, pages 1–150. Academic Press.
- Ren, H., Sigman, D. M., Martínez-García, A., Anderson, R. F., Chen, M.-T., Ravelo, A. C., Straub, M., Wong, G. T. F., and Haug, G. H. (2017). Impact of glacial/interglacial sea level change on the ocean nitrogen cycle. *Proceedings of the National Academy of Sciences*, 114(33):E6759–E6766.
- Schartau, M. and Oschlies, A. (2004). Simultaneous data-based optimization of a 1D-ecosystem model at three locations in the North Atlantic: Part I—Method and parameter estimates. *Journal of Marine Research*, 61(6):765–793.
- Schmitt, R. (2011). Salinity and the Global Water Cycle. *Oceanography*, 21(1):12–19.
- Schmittner, A., Brook, E. J., and Ahn, J. (2007). Impact of the ocean's overturning circulation on atmospheric CO₂. *Geophysical Monograph Series*, 173:315–334.
- Schmittner, A. and Galbraith, E. D. (2008a). Glacial greenhouse-gas fluctuations controlled by ocean circulation changes. *Nature*, 456(7220):373–376.
- Schmittner, A. and Galbraith, E. D. (2008b). Glacial greenhouse-gas fluctuations controlled by ocean circulation changes. *Nature*, 456(7220):373–376.
- Shackleton, N. J. and Pisias, N. G. (2013). Atmospheric Carbon Dioxide, Orbital Forcing, and Climate. In *The Carbon Cycle and Atmospheric CO₂: Natural Variations Archean to Present*, volume 32, pages 303–317. American Geophysical Union (AGU).
- Shin, S. I., Liu, Z., Otto-Bliesner, B., Brady, E. C., Kutzbach, J. E., and Harrison, S. P.

- (2003). A simulation of the last glacial maximum climate using the NCAR-CCSM. *Climate Dynamics*, 20(2-3):127–151.
- Sigman, D. M. and Boyle, E. A. (2000). Glacial/interglacial variations in atmospheric carbon dioxide. *Nature*, 407(6806):859–869.
- Sigman, D. M., Hain, M. P., and Haug, G. H. (2010). The polar ocean and glacial cycles in atmospheric CO₂ concentration. *Nature*, 466(7302):47–55.
- Thibodeau, B., Not, C., Hu, J., Schmittner, A., Noone, D., Tabor, C., Zhang, J., and Liu, Z. (2018). Last Century Warming Over the Canadian Atlantic Shelves Linked to Weak Atlantic Meridional Overturning Circulation. *Geophysical Research Letters*, 45(22):12,376–12,385.
- Timmermann, A., Krebs, U., Justino, F., Goosse, H., and Ivanochko, T. (2005). Mechanisms for millennial-scale global synchronization during the last glacial period. *Paleoceanography*, 20(4).
- Toggweiler, J. R., Gnanadesikan, A., Carson, S., Murnane, R., and Sarmiento, J. L. (2003). Representation of the carbon cycle in box models and GCMs: 1. Solubility pump. *Global Biogeochemical Cycles*, 17(1).
- Toggweiler, J. R., Russell, J. L., and Carson, S. R. (2006). Midlatitude westerlies, atmospheric CO₂, and climate change during the ice ages. *Paleoceanography*, 21(2):1–15.
- Tzedakis, P. C. (2010). The MIS 11 - MIS 1 analogy, southern European vegetation, atmospheric methane and the "early anthropogenic hypothesis. *Climate of the Past*, 6(2):131–144.

- Vettoretti, G. and Peltier, W. R. (2013). Last Glacial Maximum ice sheet impacts on North Atlantic climate variability: The importance of the sea ice lid. *Geophysical Research Letters*, 40(24):6378–6383.
- Volk, T. and Hoffert, M. I. (1985). Ocean carbon pumps. *American Geophysical Union; Geophysical Monograph 32*, 32.
- Wania, R., Meissner, K. J., Eby, M., Arora, V. K., Ross, I., and Weaver, A. J. (2012). Carbon-nitrogen feedbacks in the UVic ESCM. *Geoscientific Model Development*, 5(5):1137–1160.
- Weaver, A. J., Eby, M., Fanning, A. F., and Wiebe, E. C. (1998). Simulated influence of carbon dioxide, orbital forcing and ice sheets on the climate of the Last Glacial Maximum. *Nature*, 394(6696):847–853.
- Weaver, A. J., Eby, M., Kienast, M., and Saenko, O. A. (2007). Response of the Atlantic meridional overturning circulation to increasing atmospheric CO₂: Sensitivity to mean climate state. *Geophysical Research Letters*, 34(5):1–5.
- Yanase, W. and Abe-Ouchi, A. (2007). The LGM surface climate and atmospheric circulation over East Asia and the North Pacific in the PMIP2 coupled model simulations. *Climate of the Past*, 3(3):439–451.
- Zachos, J., Pagani, M., Sloan, L., Thomas, E., and Billups, K. (2001). Trends, rhythms, and aberrations in global climate 65 Ma to present. *Science (New York, N.Y.)*, 292(5517):686–693.
- Zeebe and Wolf-Gladrow (2001). CO₂ in seawater: Equilibrium, Kinetics, Isotopes. In Halpern, D., editor, *Elsevier oceanography series*. Elsevier Oceanography Series.

Zickfeld, K., Eby, M., Damon Matthews, H., Schmittner, A., and Weaver, A. J. (2011).

Nonlinearity of carbon cycle feedbacks. *Journal of Climate*, 24(16):4255–4275.

Capítulo 2

The Impact of ICE-6G Ice Sheet Topography in the Oceanic Carbonate System

Noele F. Leonardo¹

¹Universidade Federal de Viçosa, Departamento de Engenharia Agrícola, Viçosa,
Minas Gerais, Brasil

Juan Muglia²

²College of Earth, Ocean, and Atmospheric Sciences, Oregon State University,
Corvallis, Oregon, USA

Flavio B. Justino¹

¹Universidade Federal de Viçosa, Departamento de Engenharia Agrícola, Viçosa,
Minas Gerais, Brasil

ARTIGO SUBMETIDO

Abstract

During the Last Glacial Maximum (20ka BP) the presence of large ice sheets over the Northern Hemisphere caused significant changes in ocean-atmosphere interaction. Changes were seen in both topography and atmospheric CO₂ levels. This paper investigates the impact of the most recent paleotopography (ICE6G) in the Earth's climate and the oceanic carbonate system, based on a series of experiments conducted with the oceanic-atmosphere-vegetation-ice-carbon model, namely UVic ESCM. Results indicate enhanced cooling in northern North America in the ICE6G compared to the ICE4G simulation due to the lapse rate effect. The decrease of -24°C in the surface temperature in the ICE6G relative to the PD led to a modification of the atmospheric circulation, mainly in the Atlantic and North Pacific region. Positive and negative anomalies vary widely for the E-P flux pattern, but colder and drier atmosphere leads to a reduction in precipitation in the ICE6G experiment. Changes in wind stress between ICE6G and PD induce low temperatures in the Northern Hemisphere. These features are related changes of Ekman's transport and evaporation cooling resulting in positive anomalies of SST. Thus, changes in sea surface temperature and salinity (SST, SSS) and E-P flux lead to modifications in the oceanic carbonate system, resulting in an overall increase of total alkalinity and a reduction in the concentrations of TCO₂ in the ICE6G in relation to the PD. This is a consequence of the low concentration of glacial CO₂ and increment in CO₃²⁻ concentrations. The TA and TCO₂ do not show a similar response to the SST and SSS, in the sense that larger departures from the PD are found in the Pacific equatorial region, which are affected by changes in water dilution as a result of precipitation and evaporation processes.

2.1 Introduction

During the last two millions years the Earth's climate has fluctuated between glacial (cold) and interglacial (warm) periods in consonance with variations in the orbital configuration and atmospheric CO₂ concentration (Justino et al., 2018; Petit et al., 1999; Scheffer et al., 2009). Despite substantial effort to understand in detail the oceanic carbon cycle, questions remain unanswered. In particular, how the lower troposphere may influence changes in the oceanic biogeochemistry (Rojas, 2013).

Modeling experiments mimicking the LGM climatic characteristics are very useful, because substantial changes in the oceanic and atmospheric features occurred as compared to current conditions (Rind, 1987; Justino et al., 2006; Justino and Peltier, 2008). The climate system varies in response to external and internal processes in which most fluctuations are related to the main modes of climate variability. In the Polar Regions, the annular modes play the dominant role, whereas in the tropics, the air-sea interaction dictates the climate variability (e.g. (Deser et al., 2012)). The LGM modes of climate variability were drastically modified from present conditions in the sense that the North Atlantic Oscillation (NAO) displays four distinct centers of action and an atmospheric circulation and internal variability completely different from modern conditions (Justino et al., 2005). As well, Pacific Decadal Oscillation (PDO) (Justino and Peltier, 2008) shows a strong anti-correlated pattern between oceans and the atmosphere, with an intensified glacial flow that generates air-sea flux exchange and shift Ekman dynamics.

The oceans are one of the largest reservoirs of CO₂ and are essentially the determinant of atmospheric CO₂ concentrations. On the other hand, carbon requires

centuries to be deposited into the deep ocean thousand-year timescale of glacial to interglacial changes in the pCO_{2atm} concentrations. As we know the CO_2 taken up of atmosphere is reserved as total dissolved inorganic carbon (TCO_2), organic carbon (C_{org}) and calcium carbonate ($CaCO_3$). Since the CO_2 has the ability to dissolve in seawater and this capacity is directly related to its concentration in the atmosphere and the temperature of the water. Oceanic CO_2 time series show that the surface ocean concentrations of CO_2 following the atmospheric CO_2 increase (Bates et al., 2014).

Paleoreconstructions and modeling studies demonstrated that the ocean glacial surface was about $2.5^\circ - 4^\circ C$ cooler (Annan and Hargreaves, 2013) and the sea-levels 130 m lower (Yokoyama et al., 2000; Peltier and Fairbanks, 2006) than today. In consonance with lower atmospheric CO_2 concentrations and SST, but higher SSS during glacial times (Broecker, 1986; Sigman and Boyle, 2000). The enhancement of biological production in the Southern Hemisphere (Oka et al., 2011) due to an increase of total alkalinity in the oceans may be related to the abrupt decrease of CO_2 in the LGM epoch due to an increase efficiency of the carbonate pump (Rickaby et al., 2010). Some chemical changes in deep water from glacial times promote release of particulate inorganic and organic phosphorus, and this might increase PO_4^{3-} and the biological pump efficiency of glacial oceans concentrations (Tamburini and Föllmi, 2009). Assumption is also raised associated to the iron dust supplies being mainly responsible for the decrease in atmospheric CO_2 levels.

The salinity increased of oceans in the ice ages is one of the opposite effects of the temperature changes in CO_2 concentrations. The largest accumulation of fresh water, a decrease in mean sea level, it is possible evaluate that the global ocean

in the Last Glacial Maximum (LGM) was about 3% saltier than today (Fairbanks, 1989). The spatial distribution of dissolved inorganic carbon (TCO_2) and the total alkalinity (TA) is reliant on temperature and salinity, which maintains the solubility in seawater by CO_2 . Reconstructions of deep water carbonate (CO_3^{2-}) suggest that the global TA was increased in the glacial ocean and changed by additional TCO_2 sequestration (Rickaby et al., 2010; Yu et al., 2013). Previous studies have pointed out that increased upwelling during the LGM period led to an excess of nutrients, especially nitrate (NO_3^-) which increased high-nitrate low-chlorophyll (HNLC) conditions (Farrell et al., 1995; Kohfeld et al., 2005). Nitrate is a nutrient highly dependent on marine productivity and carbon sequestration via the biological pump. It has suggested that the increase in the use of both NO_3^- and phosphate (PO_4^{3-}) during the LGM may have been due to the higher biological demand of these nutrients with respect to today (Martin, 1990). Despite these findings, the investigation of the LGM carbonate system is still needed because chemical changes impact on both the marine biological processes and the sequestration and dissolution of CO_2 .

The primary goal of this paper is to evaluate the UVic ESCM ability to simulate the LGM climate by comparing the response of different Paleotopography ICE6G (Peltier et al., 2015; Argus et al., 2014) and ICE4G (Peltier, 1994). Moreover, the impact of anomalous atmospheric and oceanic feature on total alkalinity (TA), total carbon dioxide (TCO_2) and nutrients (NO_3^- and PO_4^{3-}) are investigated. The analyses are based on sensitive experiments mimicking the current climate (1940-2015) and LGM conditions using those different paleotopographies and CO_2 concentrations.

The paper is organized as follows: Section 2 describes the coupled model, the design of the four experiments and the statistical approach. In section 3, the main results are presented from regression analyses as well the influence of Pacific Decadal Oscillation (PDO) on the oceanic biogeochemistry. Section 4 compiles the results and provides a discussion on the implications of the different topographies on the global oceanic carbonate system.

2.2 Data and Model Setup

2.2.1 Model Description

We investigate the oceanic carbon system and nutrients, including total alkalinity (TA), total dissolved inorganic carbon TCO_2 , NO_3^- , PO_4^{3-} and how these quantities vary with respect to temperature, salinity and winds for present day (PD) and LGM conditions.

Use the global ocean circulation model UVic ESCM (Earth System Climate Model) version 2.9 from University of Victoria . The UVic ESCM is a coupled model of intermediate complexity that includes a general three-dimensional oceanic circulation model (Modular Ocean Model, Version 2, (Pacanowski, 1995)) with 19 vertical levels and a resolution 1.8° for latitude and 3.6° for longitude. Coupled to a vertically integrated two-dimensional atmospheric model based on energy-moisture balance, a thermodynamic-dynamic sea ice model (Weaver et al., 1998).

Land surface scheme with a global dynamical vegetation (Meissner et al., 2003) and a sediment model (Archer, 1996). The biogeochemical module of the UVic ESCM also includes a fully coupled carbon cycle with terrestrial carbon fluxes and

reservoirs ((Meissner et al., 2003; Matthews, 2006) , organic (Schmittner and Galbraith, 2008) and inorganic (Ewen et al., 2004) carbon cycle in the ocean. This follows the Ocean Carbon Cycle Model Intercomparison Project (OCMIP) protocol (Orr, 1999) and the scheme also includes the interaction between nutrients, two types of phytoplankton and zooplankton (Wania et al., 2012).

The ecosystem-biogeochemical scheme is a nutrient-phytoplankton-zooplankton-detritus (NPDZ) model (Schmittner et al., 2005) with parametrization based on (Schartau and Oschlies, 2004) with microbial induced the nutrient recycling. The marine sediment component has 13 layers and the amplitude covers a few millimeters near of sediment surface to a few centimeters at the bottom domain at a depth of 10 cm. The dissolution of CaCO_3 to sediment assumes an instantaneous sinking of vertically integrated production (Schmittner and Galbraith, 2008) and the balance between respiration rate and sediment-mixing rate is induced by penetration depth of particulate organic carbon (POC) into sediment surface mixed layer in contact with pore layer. Concentrations and burial rates of sedimentary CaCO_3 are presumed using the particulate inorganic carbon (PIC) and POC rain ratio, dilutant burial rates and the reaction rate laws for both CaCO_3 and organic carbon (Archer, 1996). Only dissolution of oxic metabolic sedimentary CaCO_3 is simulated by the sediment scheme and the processes are represented using only oxic model of sediment respiration (Eby et al., 2009).

The PD, ICE6G, ICE5G and ICE4G simulations were integrated for 10.000 years starting from the same initial conditions and our analysis focus on the last 100 years of the simulation after the model reached the equilibrium, characterized by stabilization of marine nutrients.

2.2.2 Paleotopography Experiments

Comparing the ICE4G LGM reconstruction (Peltier, 1994) with present day topography, large continental ice sheets appear over North America, Scandinavia and east Siberia. The successor of ICE4G, ICE5G (Peltier, 2004), differs dramatically from the former dataset at all North American locations, Northwestern Eurasia/Europe (Peltier, 2004, 2002) and Greenland (Tarasov and Richard Peltier, 2002). Differences between ICE5G (Peltier, 2004) and ICE6G (Argus et al., 2014; Peltier et al., 2015) are primarily found in the western flank of the Laurentide Ice Sheet, and in the Canadian archipelago where ICE6G is higher. However, in central Canada ICE6G is lower than the ICE5G by about 1500 meters. No large topographic changes are noted in the west coast of North America.

Paleotopography differences between ICE6G and present day conditions, and between ICE6G and ICE4G, are shown in Figure 2.1. The ICE6G topography is higher by about 3000 meters when compared to current conditions in North America, Scandinavia and Eastern Siberia (Fig. 2.1a). Also, ICE6G differs significantly from ICE4G throughout the North American region, being approximately 1500 meters higher, and 500 meters lower in Greenland. In the Antarctic region the ice sheets are predominantly lower in ICE6G than in ICE4G by an average 1000 meters (Fig. 2.1b).

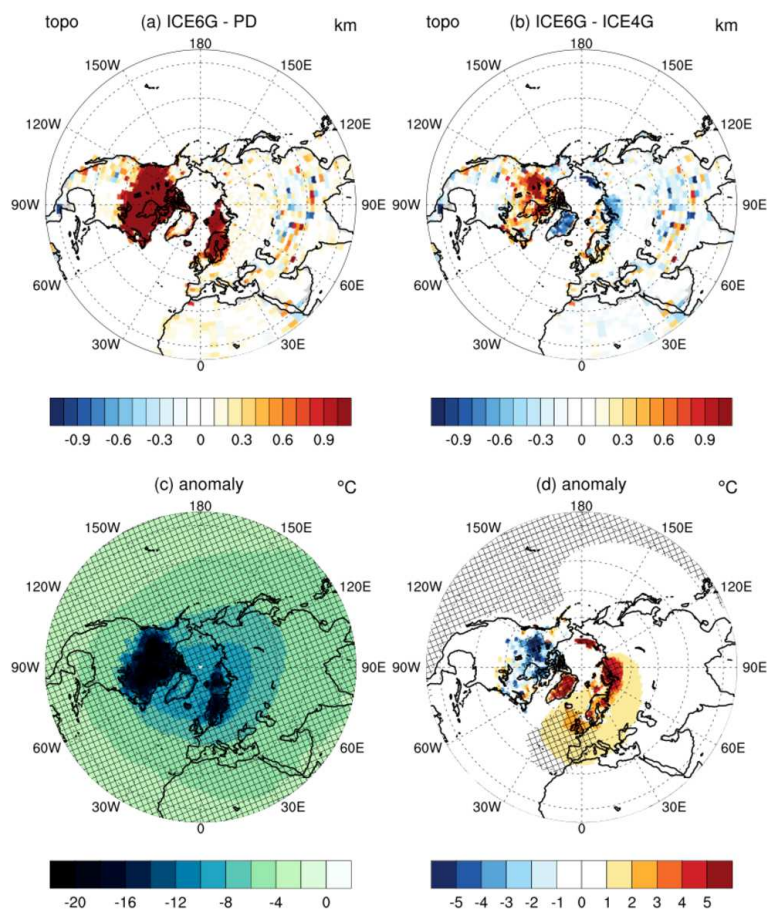


Figura 2.1: (a) Paleotopography anomalies between ICE6G and PD reconstructions [Km]. (b) as (a) but for ICE6G and ICE4G reconstructions (c) surface temperature differences between ICE6G and PD simulations (°C).(d) As (c) but for ICE6G and ICE4G differences. Hachured areas are statistically significant at the 95% level.

2.2.3 Experimental Design

Three experiments were conducted in order to investigate the atmospheric and oceanic response to the LGM topography. The first experiment (PD climate) is initialized from pre-industrial conditions applying an atmospheric CO_2 concentration of 380ppm. Our PD climate is the averaged climate between the years 1940-2015. Current orbital forcing and boundary conditions are used. Marine biogeochemistry follows the protocol proposed by the Ocean Carbon-Cycle Model Intercomparison Project (OCMIP) (Orr, 1999; Orr and Epitalon, 2015). Three LGM experiments were

conducted with the ICE4G (Peltier, 1994), ICE5G(Peltier, 2004) and ICE6G (Argus et al., 2014; Peltier et al., 2015) paleotopographies, atmospheric CO₂ concentration of 185 ppm, and the appropriate orbital forcing for the LGM period (Berger and Loutre, 1991). All paleotopographies are included in UVIC as anomalies with respect to the PD topography (Figure 2.1). Since the model includes a parameterization of water vapor/planetary longwave feedbacks, we include the radiative effect of N₂O and CH₄ for LGM for LGM as a modification of the planetary longwave radiative flux (Eby et al., 2009; Schmittner et al., 2011). It has to be mentioned that due to the large similarity between the simulations conducted with the ICE5G and ICE6G ice sheets, we only present results for the ICE4G and ICE6G reconstructions.

2.2.4 Wind Stress

The surface wind stress is the most important force for the oceanic circulation at the base of atmospheric boundary layer and their pattern can reflect the overall structure of the atmospheric and ocean circulation on a global scale. The LGM simulation includes glacial topography, orbital forcing and CO₂, however, as discussed (Fanning and Weaver, 1997; Handiani et al., 2013),the UVic has a parameterization for anomalous surface winds and wind stress taking into account any climate perturbation, delivered by near surface temperature and density anomalies, reproducing mainly the buoyancy force. The UVic LGM wind stress is compared with the Paleoclimate Model Intercomparison Project Phase 3 (PMIP3) models ensemble. These wind stress fields include a multi-model mean of LGM anomaly from PMIP3 and uses the initial condition wind stress from NCEP reanalysis plus PMIP3 multi-model mean for LGM minus pre-industrial wind stress anomaly, more de-

tails by (Muglia and Schmittner, 2015). For the LGM continental ice sheets, we use the reconstruction from the PMIP3 set up (?). Figure 2.2 shows the standard deviation (STD) and the zonal mean for the zonal and meridional wind components from the PMIP3, ICE6G and ICE4G simulations. The STD for both wind stress vectors (x, y) demonstrated reasonable agreement in the spatial pattern. This finding useful series to highlight that despite the intermediate complexity of UVic it can faithfully reproduce the time variability.

The zonal pattern is in accordance with the PMIP3 data well. Disagreements between the datasets are found in the Northern Hemisphere (NH) for the two components between the latitudes of $40^{\circ}\text{N} - 60^{\circ}\text{N}$. It can be argued that these differences in NH may be related to differences between the ice sheets topographies used in the PMIP3. It has to be mentioned that (Muglia and Schmittner, 2015) attributes the strengthening of the Meridional Overturning Circulation (MOC) to the use of wind pattern from the PMIP3 datasets.

2.2.5 Evaluation of the present day simulation

The performance of the UVic ESCM model to simulate the PD simulation is tested by comparing its output to the Global Ocean Data Analysis Project vol.2 (GLODAP_v2; (Key et al., 2015; Olsen et al., 2016)).

The GLODAP is a project cooperation of the National Oceanic and Atmospheric Administration (NOAA), the US Department of Energy (DOE) and the National Science Foundation (NSF) as part of the Joint Global Ocean Flux Study Group - Synthesis and Modeling Project "(JGOFS -SMP). GLODAP v2 is a combination of products from Carbon dioxide in the Atlantic Ocean (CARINA; (?)) and Pacific

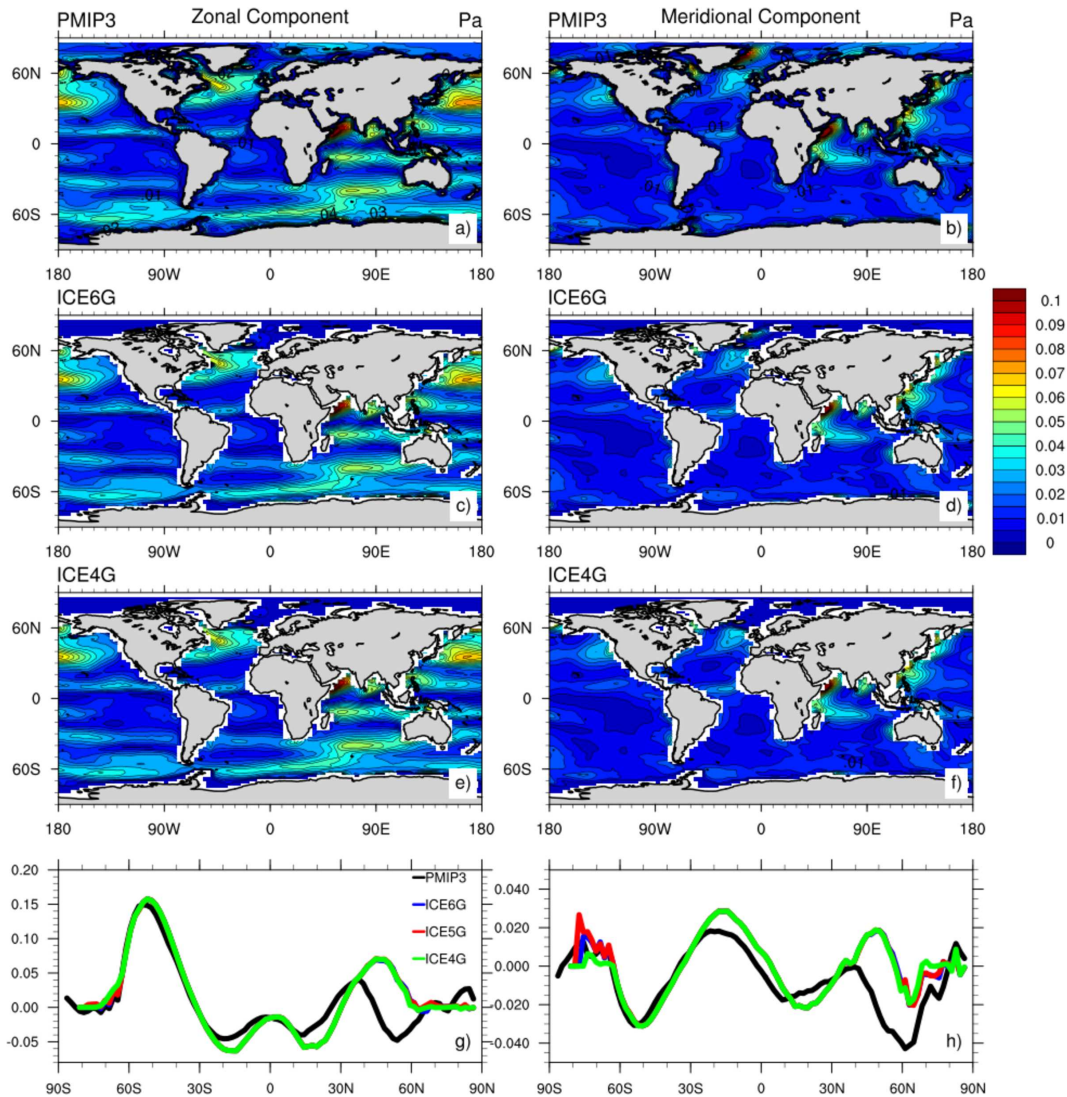


Figure 2.2: Standard deviation for simulated zonal and meridional surface wind stress for (a,b) PMIP3, (c;d) ICE6G and (e,f) ICE4G. Simulated annual mean zonal (g) and meridional (h) surface wind stress over the ocean for PMIP3 (black), ICE6G (blue), ICE5G (red) and ICE4G (green). PMIP3 data from (Muglia and Schmittner, 2015)

Ocean Inland Carbon (PACIFICA; (?)), plus 168 new cruises covering the Mediterranean Sea and the Nordic Sea (> 65 °N). GLODAPv2 data is available in three ways: (1) original without calibration; (2) as a merged data product where adjustments have been applied to minimize measurement bias and (3) weather maps. It is a set of data from marine cruising research centers comprised of 9618 hydrographic stations collected between 1985 and 2017 across the globe to create a quality and

quantity oceanographic database (??). Data are calibrated with quality-control for final mapping and interpolation and are available online in both raw and interpolated form.

Although the model has a simplified atmospheric component, sea surface temperature (SST) and sea surface salinity (SSS) exhibit a spatial averaged with good agreement between the PD climatology and GLODAP_v2 (not shown). The surface global differences with observations are shown in Figure 2.1.

The simulated SST shows an average of 17.55 °C about 0.26 °C colder than the GLODAP_v2 (17.82 °C). However, larger differences are found as in the Gulf of Alaska, Greenland, Iceland and Norway (GIN), and the North Atlantic region, where the model is cooler than GLODAP_v2. The simulated surface salinity differs by about 0.18 from GLODAP_v2 with most differences found in the subtropical gyres. Turning NO_3^- and PO_4^{3-} , both datasets show the major features in agreement with observations. The overall mean of NO_3^- is 7.21 $\mu\text{mol}/\text{kg}$ for GLODAP_v2 which is 0.83 $\mu\text{mol}/\text{kg}$ higher as compared to simulated (6.38 $\mu\text{mol}/\text{kg}$) values. The simulated PO_4^{3-} differs by about 0.16 $\mu\text{mol}/\text{kg}$ from GLODAP_v2.

Tabela 2.1: Global surfaces averages, differences, correlation coefficient and standard deviation-normalized root mean square error (RMSE) between UVic ESCM simulation control versus GLODAP_v2 (Olsen et al., 2016) observations. For Global, NH and SH subtropics and Tropical region averages.

		Glodap v2	UVic ESCM	Diff	Cor	RMSE
SST (°C)	Global	17.82	17.55	0.27	0.989	1.060
	30 °N - 60 °N	14.33	15.061	0.73	0.950	0.884
	30°N - 30 °S	25.15	25.96	0.81	0.910	1.032
	30°S - 60°S	11.61	10.72	0.89	0.981	0.976
SSS	Global	34.78	34.60	0.18	0.871	0.860
	30 °N - 60 °N	34.42	34.49	0.02	0.944	0.944
	30°N - 30 °S	34.92	35.21	0.29	0.822	0.773
	30°S - 60°S	34.54	34.53	0.01	0.832	1.041
TA ($\mu\text{mol}/\text{kg}$)	Global	2304.38	2337.66	32.76	0.810	0.965
	30 °N - 60 °N	2336.55	228.97	47.58	0.572	1.010
	30°N - 30 °S	2341.84	2323.41	18.43	0.359	2.190
	30°S - 60°S	2343.23	2299.86	43.38	0.954	1.157
TCO ₂ ($\mu\text{mol}/\text{kg}$)	Global	2039.9	2028.16	11.74	0.933	0.799
	30 °N - 60 °N	2045.15	2042.77	2.38	0.510	1.189
	30 °S - 30 °N	1967.23	1997.01	29.78	0.514	0.222
	30 °S - 60 °S	2076.89	2091.55	14.72	0.937	0.775
PO ₄ ³⁻ ($\mu\text{mol}/\text{kg}$)	Global	0.555	0.715	0.16	0.773	0.903
	30 °N - 60°N	0.43	0.50	0.07	0.927	0.915
	30 °S - 30°N	0.567	0.253	0.314	0.798	1.022
	30 °S - 60°S	0.875	0.995	0.120	0.559	0.863
NO ₃ ⁻ ($\mu\text{mol}/\text{kg}$)	Global	7.21	6.38	0.83	0.950	0.968
	30 °N - 60 °N	3.98	4.97	0.99	0.857	0.687
	30 °S - 30 °N	1.14	1.53	0.39	0.830	0.818
	30 °S - 60 °S	8.67	11.21	2.54	0.930	0.957

Values of TCO_2 vary between $2230 \mu\text{mol}/\text{kg}$ in the polar regions and $1800 \mu\text{mol}/\text{kg}$ in the subtropical regions for both simulated and GLODAP_v2 (see Tab. 2.1). The simulated TA shows global mean values up to $2337.66 \mu\text{mol}/\text{kg}$, differing from the GLODAP_v2 by about $32.76 \mu\text{mol}/\text{kg}$. The simulated global surface distribution (not shown) accurately reproduces the main features of surface TA found in the observations.

Similarly values of nutrients by the UVic ESCM are also reasonable with respect to the observational estimates, as can be seen from the high correlation and low root mean square errors (Figure 3.1) when comparing our PD simulation with the GLODAP_v2 reconstruction.

2.3 Results and Discussion

2.3.1 ICE6G Climate

Changes in topography lead to near surface air temperature anomalies over North America by about -24°C in the ICE6G simulation as compared to present day conditions, and differences over the Fennoscandian ice sheet by about -18°C (Fig. 2.1). When compared to the ICE4G simulation, the ICE6G simulation experiment a decrease in the near surface temperature over the North American region. However, an increase in temperatures of up to 6°C occurs over Greenland, Scandinavia, Eurasia, and in the Antarctic continent in the ICE6G simulation, with respect to the ICE4G simulation. Since changes in albedo between the two runs are negligible, differences in the ICE6G and ICE4G a temperatures arise as a result of the lapse rate effect.

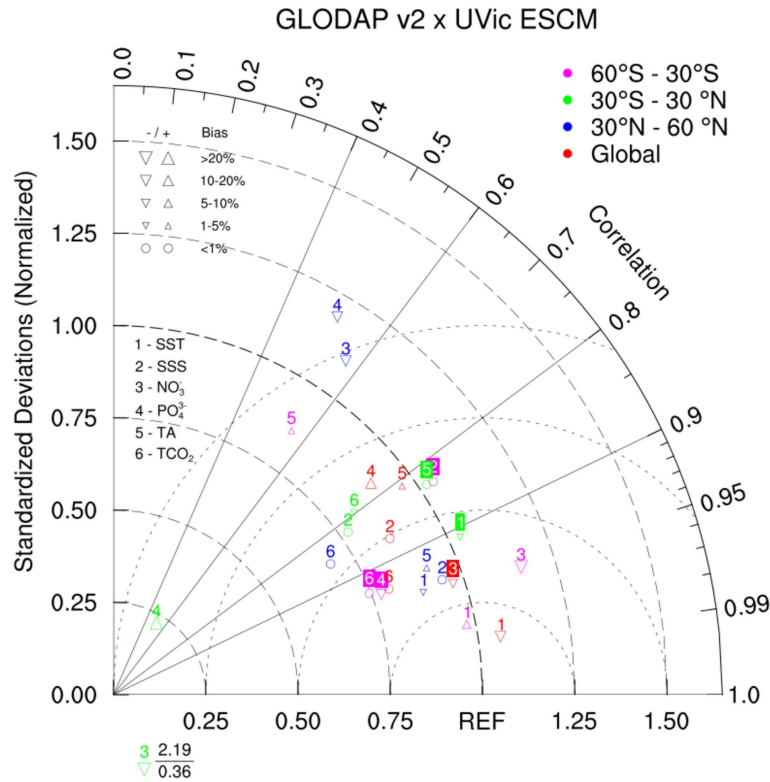


Figura 2.3: Taylor diagram comparing statistic pattern of annual mean fields between UVic ESCM simulation control and corresponding GLODAP_v2 observations, including surface temperature, salinity, nitrate, phosphate, total alkalinity and TCO₂. All fields are normalized by the standard deviation of corresponding observations. Indeed, observation fields have a standard deviation of one, which is represented by REF (x label). The distance between the model points and the reference point indicate the quadratic -root-mean-square (QRMS) difference between model simulation and observations.

Figure 2.4 presents differences between ICE6G and PD and ICE6G and ICE4G simulations for surface winds, sea surface temperatures and fresh water flux (E-P). Surface wind speed (Fig. 2.4a) is intensified in the ICE6G run as compared to both PD and ICE4G, particularly over the North Atlantic and Pacific (Fig. 2.4b). However, winds are weakened in the Southern Hemisphere tropical region, and over the northern portion of the Indian Ocean. Throughout the manuscript some comments may appear in respect to changes in the Southern Hemisphere, however, in most cases such figures are not shown. We confined most of the figures to the Northern Hemisphere where changes are much more accentuated as compared

to the Southern Hemisphere. Differences between ICE6G and ICE4G simulations (Fig. 2.4b) indicate that wind stress in the former experiment are linked to the mid-latitudes meridional thermal gradient (Justino et al., 2006).

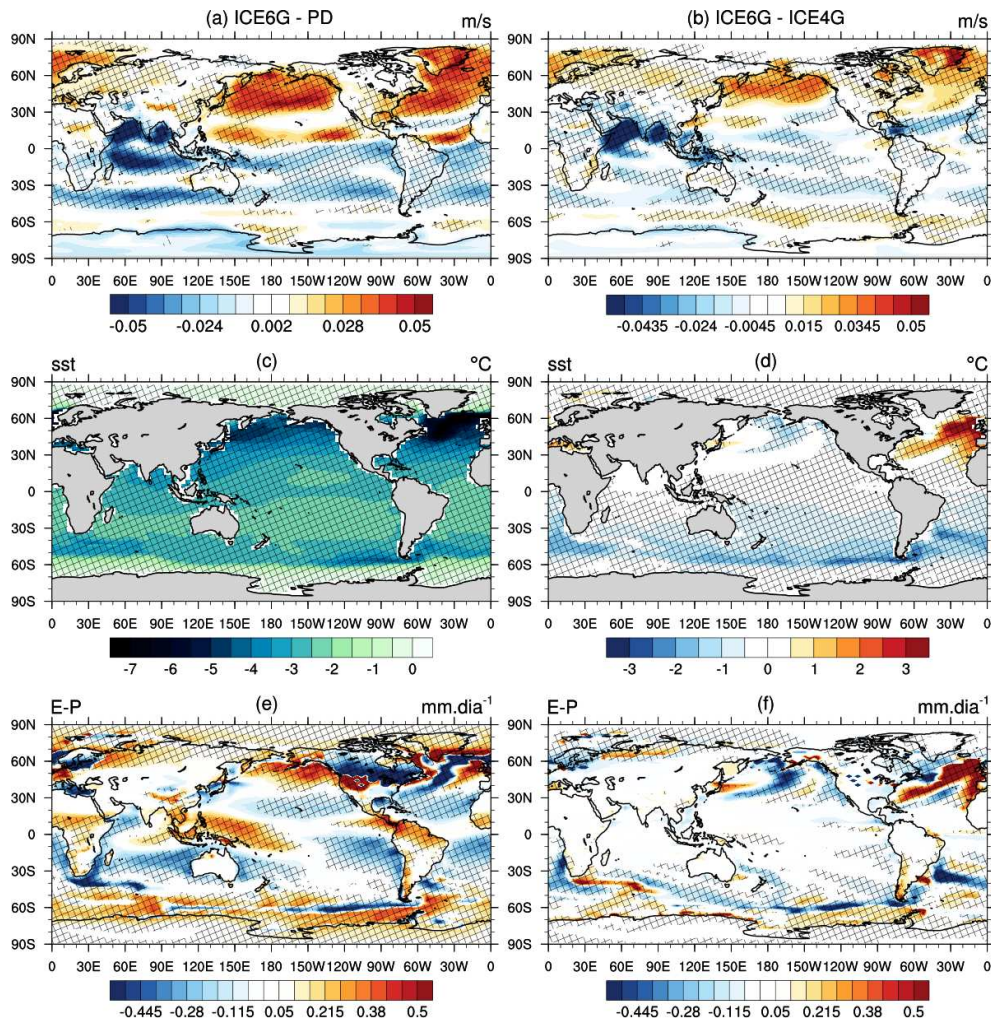


Figura 2.4: (a) Annual mean wind speed anomalies between ICE6G and PD (m/s). (b) sea surface temperature (°C) and (c) E-P flux (mm/day); (b), (d) and (f) are the same as (a), (c) and (d) but for differences between ICE6G and ICE4G runs. Hatched areas are statistically significant at the 95% level.

As expected, the climate with ICE6G topography leads to lower SST (Fig. 2.4) with respect to the PD associated with a decrease of CO₂ concentrations. Changes are larger in the Nordic Sea region and western north Pacific in consonance with the wind intensification. However, the SST anomalies between the ICE6G and ICE4G simulations (Fig. 2.4d) show a warmer North Atlantic region in the ICE6G

case. A similar pattern was found by (Justino et al., 2006) in analyzing differences between climate simulations conducted with the ICE5G and ICE4G topographies on a simpler model. They attributed this warming to the air subsidence to the south and east of the topographic anomaly. In the Southern Hemisphere, SSTs in the vicinity of the Antarctic continent are about -2.5 °C cooler in the ICE6G experiment with respect to ICE4G.

Important for the hydrological cycle and the oceanic carbonate system, the fresh water flux is also affected by changes in topography (Fig. 2.4e,f). As shown in the Figure 2.4 the dominant patterns of the E-P flux anomalies vary globally with scattered positive and negative anomalies. Indeed, in a large part of the tropical regions reduced fresh water in the ICE6G simulation with respect to PD is observed. Changes in E-P, between the two runs are induced by a reduction in precipitation related to a drier atmosphere in the ICE6G experiment. Positive anomalies are noted in the North Atlantic region and the Labrador Sea related to the cold and dry eastward flow from the Laurentide ice sheet reducing precipitation. Turning to anomalies between ICE6G and ICE4G (Fig. 2.4f), positive values in the North Atlantic region indicate that the ICE6G evaporation is higher than that ICE4G. These modifications result in increased surface salinity throughout the North Atlantic in the ICE6G experiment with respect to the ICE4G run (not shown). These changes in the thermal and haline oceanic characteristics induce changes in the rate of water mass formation.

Under PD conditions (Fig. 2.5a) the upper cell of the Atlantic Meridional Overturning (AMOC) extends between 800 and 2000 meters deep with a maximum transport of 20Sv, occurring at 1700m (Fig 2.5a). For glacial conditions the trans-

port is between 15-10Sv for the LGM ICE6G simulation but a shutdown of the AMOC occurs in the ICE4G simulation (Fig. 2.5). Higher transport is also found in the abyssal overturning cell of MOC in the two LGM runs compared with PD counterpart. The MOC is weaker in the LGM, for both the ICE6G and in ICE4G runs suggesting a more stratified ocean contrast with models from the Paleo Climate Model Intercomparison Project 3, as shown in (Muglia and Schmittner, 2015). Our results are consistent with other studies based on atmosphere-ocean coupled models, which show a weaker MOC as a response to ice sheet topography and a northward drift of the abyssal overturning cell of MOC. (Ferrari et al., 2014; Negre et al., 2010). It has to be mentioned that modeling results present distinct results insofar as the magnitude of the glacial AMOC is concerned (Weber et al., 2007).

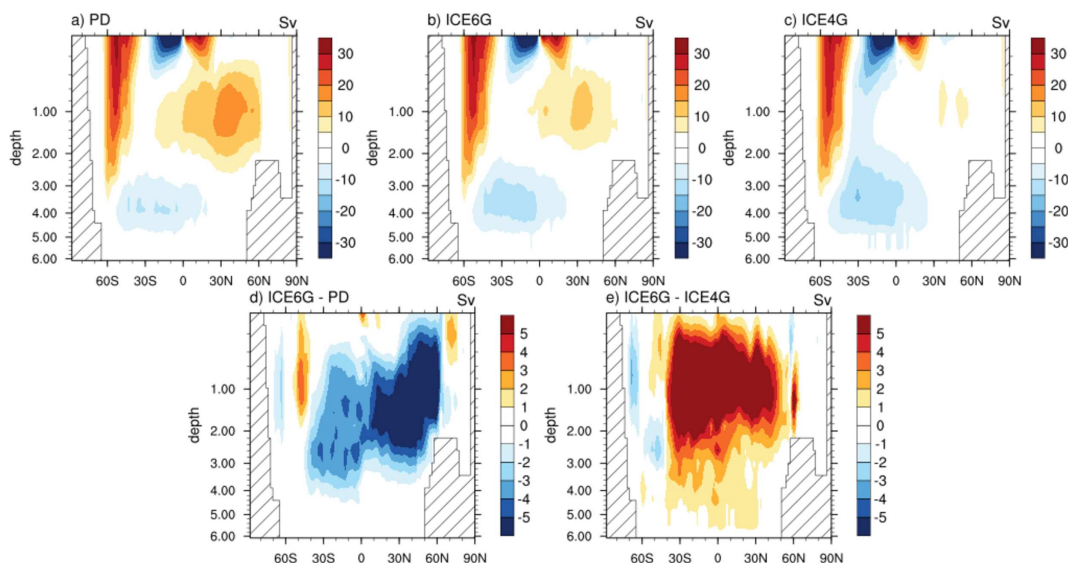


Figura 2.5: Global meridional overturning circulation based on (a) PD conditions, (b) ICE6G (c) ICE4G and (d) differences between ICE-6G and PD and (e) anomalies between ICE6G and ICE4G.

Figure 2.6 shows the globally ocean temperature for the three simulations in each ocean basin. All the three basins (Atlantic, Pacific and Indian) in the LGM's simulations are cooler than those in the PD run. For the Atlantic basin (2.8) the

ICE6G and ICE4G delivered very close results. Unlike the Pacific and Indian Basins, where ICE4G is slightly warmer than the ICE6G. At 1000 m depth, the LGM temperature range from approximately 0.5 °C to -2 °C where in the PD it is from 5 °C (7 °C for Indian Basin) to 0.5 °C. It is interesting to notice that the Pacific Ocean is colder and saltier than the Atlantic.

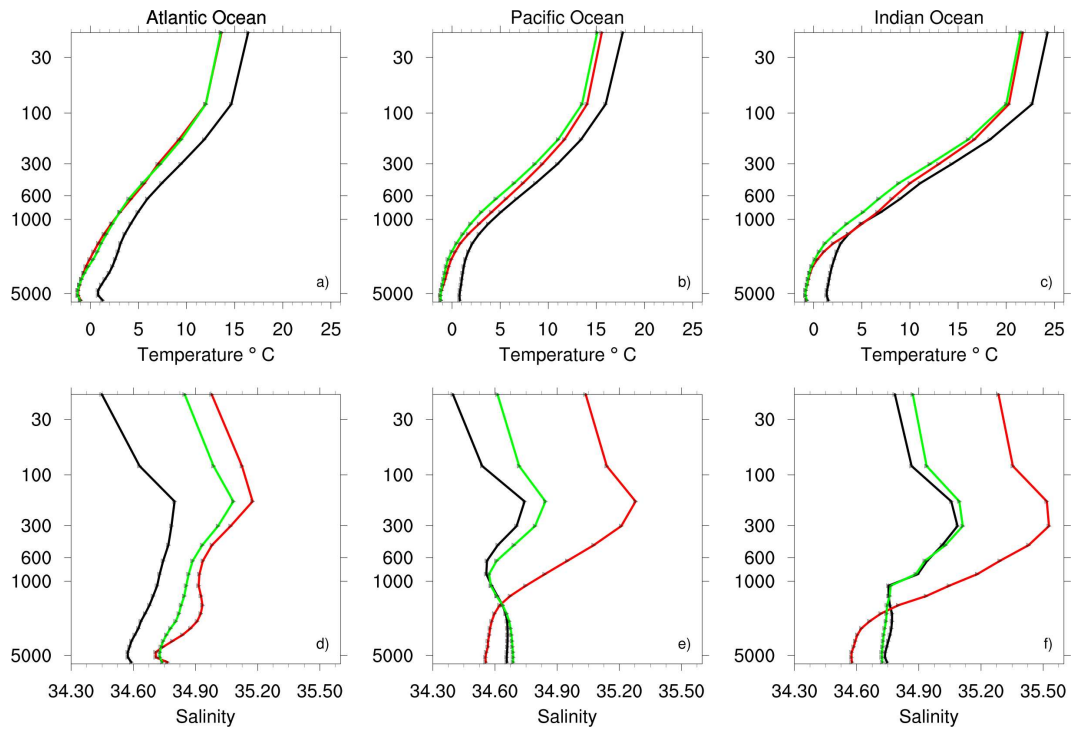


Figura 2.6: Global ocean basin average vertical profile of temperature (°C) and salinity, from simulations of PD, ICE6G and ICE4G.

In general the Indian Basin is warmer than the others for all simulations. The thermocline base is slightly shallower in the Pacific and Indian than in the Atlantic. As expected the salinity increases over ocean basins in the LGM simulations, partly related to reduced fresh water with respect to the PD simulation. Paleoreconstructions show that the bottom water of the LGM was more saline and more stratified than today (Watson and Naveira Garabato, 2006; Buchanan et al., 2016). The LGM's salinity increases all over basin, but not equally distributed. The

sea ice cover growth and melting results in a vertically asymmetric distribution of salt, which is consistent with our results.

2.3.2 The Glacial Marine Carbon System

The marine carbon system is evaluated from calculation of TCO_2 , TA, NO_3^- and PO_4^{3-} . These quantities are impacted by changes in wind stress, fresh water fluxes, temperature and salinity (Fig. 2.7). Analyzing differences between the LGM and PD simulations, changes in surface winds, temperature and in E-P rates (Fig. 2.4) promote changes in the oceanic biogeochemical cycle (Fig. 2.9). Since the UVic has the coupled sediment scheme on, it can be inferred that the variability of TA as well as on the removal is directly related through CaCO_3 burial. Mean surface TA increases in the ICE6G (2367.65 $\mu\text{mol}/\text{kg}$) with respect to the PD simulation (2337.73 $\mu\text{mol}/\text{kg}$).

Elevated oceanic alkalinity in glacial times leads to a decrease of burial CaCO_3 . In the North Atlantic (GIN seas), a decrease in surface TA may be related to increased glacial pH and carbonate ions CO_3^{2-} due to the carbonate compensation. The burial mass anomalies of CaCO_3 (not shown) between ICE6G and PD conditions were by about $\approx 150 \text{ g C m}^3$ higher in PD than in the LGM. However, for the GIN Sea alkalinity negative anomalies are found ($\approx 10 \text{ g C m}^3$) which have been associated with the burial CaCO_3 mass. Differences between the (2367.65 $\mu\text{mol}/\text{kg}$) and ICE4G (2397.84 $\mu\text{mol}/\text{kg}$) show lower TA values in the ICE6G with respect to ICE4G run. However, in the North Atlantic and GIN seas the TA is higher in the ICE6G related to positive SST and E-P flux anomalies. Turning to the TCO_2 , Figure 4c shows lower surface averages in the ICE6G experiment compared to PD, with

the exception of the Weddell Sea and the eastern portion of Antarctica.

Large fluctuations of the TCO_2 are due to the solubility pump and are highlighted in downwelling regions and subtropical gyres. The lower atmospheric CO_2 prescribed for the LGM experiment, equilibrates the ocean TCO_2 at lower values, thus producing lower surface concentration in the ICE6G experiment ($1988\mu\text{mol/kg}$) compared with the PD ($2027\mu\text{mol/kg}$). This reduction of the concentrations of TCO_2 acts to capture the atmospheric CO_2 . Although the solubility pump has the major role, the biological pump also has the ability to reduce surface TCO_2 as organic C through decomposition and sinking of the water column into the deep ocean. In the deep ocean the regeneration of the TCO_2 is helped by the decrease of the carbonate concentrations, changing the state of saturation of the calcium carbonate CaCO_3 .

In general both LGM's and PD ocean basins are enriched in TCO_2 compared with the surface. Glacial TCO_2 concentrations (fig. 2.8d,e,f) are approximately $85\mu\text{mol/kg}$ than PD. This carbon loss may be related to the physical changes, like the increase in sea ice areas, solubility due to cooling, and changes in the MOC. In the surface is because of lower pCO_2 concentration at the LGM than PD. The maximum concentration for TCO_2 in Pacific (Indian) is found in intermediate waters between 1500 - 2500 m (1000 - 1500 m). Both deep TA and TCO_2 are higher in the Pacific and Indian than in the Atlantic, for LGM's and PD simulations, because older waters are enriched over time with the conveyor belt circulation. Besides that, circulation plays an important role in the TCO_2 and TA distribution through ocean basins. These variations in surface ocean carbonate concentrations are correlated with salinity (fig. 2.6). While mainly the physical dynamics and export production

determine the surface concentration of nutrients, vertical distribution is controlled by remineralization (Archer, 1996). The colder surface waters filled the LGM's simulation with more oxygen concentrations than PD ((fig. 2.8g,h,i) for all ocean basins. For Pacific and Indian, the difference was more than 120 $\mu\text{mol/kg}$ greater than PD. An increase in oxygen concentrations in the deep ocean for all ocean basins and the anoxic water was less than PD simulations, with the exception of the Atlantic basin, where the concentrations were similar.

Global averages of nitrate (phosphate) are 4.41 $\mu\text{mol/kg}$ (0.68 $\mu\text{mol/kg}$) and 5.29 $\mu\text{mol/kg}$ (0.71 $\mu\text{mol/kg}$) for the ICE6G and ICE4G simulations. These values are similar to those found in PD run, 5.38 $\mu\text{mol/kg}$ (0.74 $\mu\text{mol/kg}$), respectively. The surface mean reveals negative anomalies in the Equatorial Pacific, Pacific sector of the Southern Ocean and Sub-Arctic North Pacific and Atlantic, when compared to the other two simulations (Fig. 2.9e-h). The natural pattern of both PO_4^{3-} and NO_3^- is represented by a pronounced latitudinal gradient but few differences between the ocean basins. High concentrations are found in high latitudes and Pacific - Atlantic Equatorial regions, due to strong upwelling. Positive anomalies were found primarily in the Atlantic sector of the Southern Ocean. The low nutrient variations between LGM and PD are related to the non-inclusion of dissolved iron (DFe) mainly of nitrate concentrations; however, the shallower and weaker MOC in the LGM simulation may act to suppress the nutrient transfer from the deep ocean to the surface. The increase in stratification and northward transport of MOC deep cell may be one of the main factors for this suppression.

Usually nitrogen and phosphorus cycles are treated similarly in the biogeochemical models, connected by the Redfield ratio (106C:16N:1P). Bacterial processes

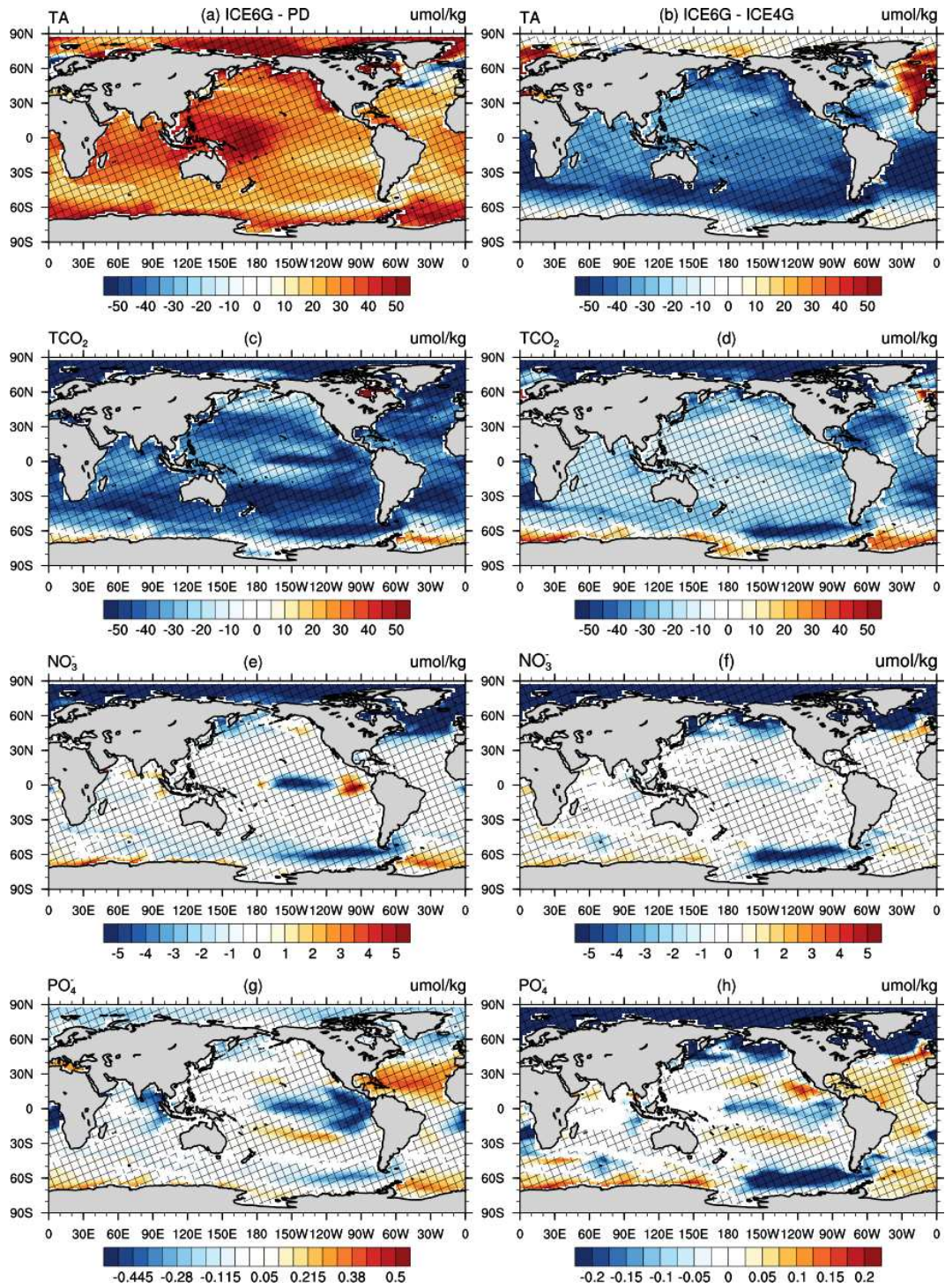


Figura 2.7: Anomalies between the ICE6G and PD (a, TA), (c, TCO₂), (e, NO₃⁻) and (g, PO₄³⁻). Anomalies between ICE6G and ICE4G simulations (b, Ta), (d, TCO₂), (f, NO₃⁻) and (h, PO₄³⁻). Hatched areas are statistically significant at the 95% level.

like nitrogen fixation and denitrification change the distribution of PO₄³⁻ and NO₃⁻.

One of the explanations for to lowering the atmospheric concentration of CO₂ on

the glacial times is the nutrient hypothesis (McElroy, 1983). It is proposed that surface water carbon fixation and removal may increase the nutrient concentration on the global oceans leading to increases in the (C/N/P) ratio. This hypothesis is most important in the Southern Ocean because of a great amount of unused inventory of surface nutrients and the connection between the surface and deep water rich in CO_2 (Sigman and Boyle, 2000). The Atlantic, Pacific and Indian vertical average for marine carbon system are shown in Figure 2.8. For the Atlantic basin, both LGM's and present day simulations show qualitatively similar distribution of TA (fig. 2.8a,b,c), the higher alkalinity for LGM's in the deep ocean than PD and between ICE6G and ICE4G. The lower TA between 500 - 600 m may be associated with biological production of CaCO_3 and for that the higher TA in the deep ocean results from the dissolution of CaCO_3 . This is more pronounced in the Pacific and Indian Basins. One observation, the LGM simulations result in more alkaline and saline waters than the present.

The increase in Atlantic basin was relative to formation of intermediate and deep water. The increase of PO_4^{3-} in LGM simulations is relative to the high subduction of AABW (phosphate-rich water mass) reducing the concentrations of PO_4^{3-} to the upper layers of the ocean. For Atlantic Basin, NO_3^- and PO_4^{3-} both LGM's and PD simulations increase in the abyssal with elevation of TA, TCO_2 and O_2 concentrations below 2500 m. The intense oxygen minimum and high nutrients concentrations. So the nutrients are not consumed by biologic activity, they were dragged to the deep ocean as high-preformed nutrients concentrations at water masses formation (deep and intermediate). The formation of water masses such as NADW and AABW controlled the preformed nutrient concentration in the ocean

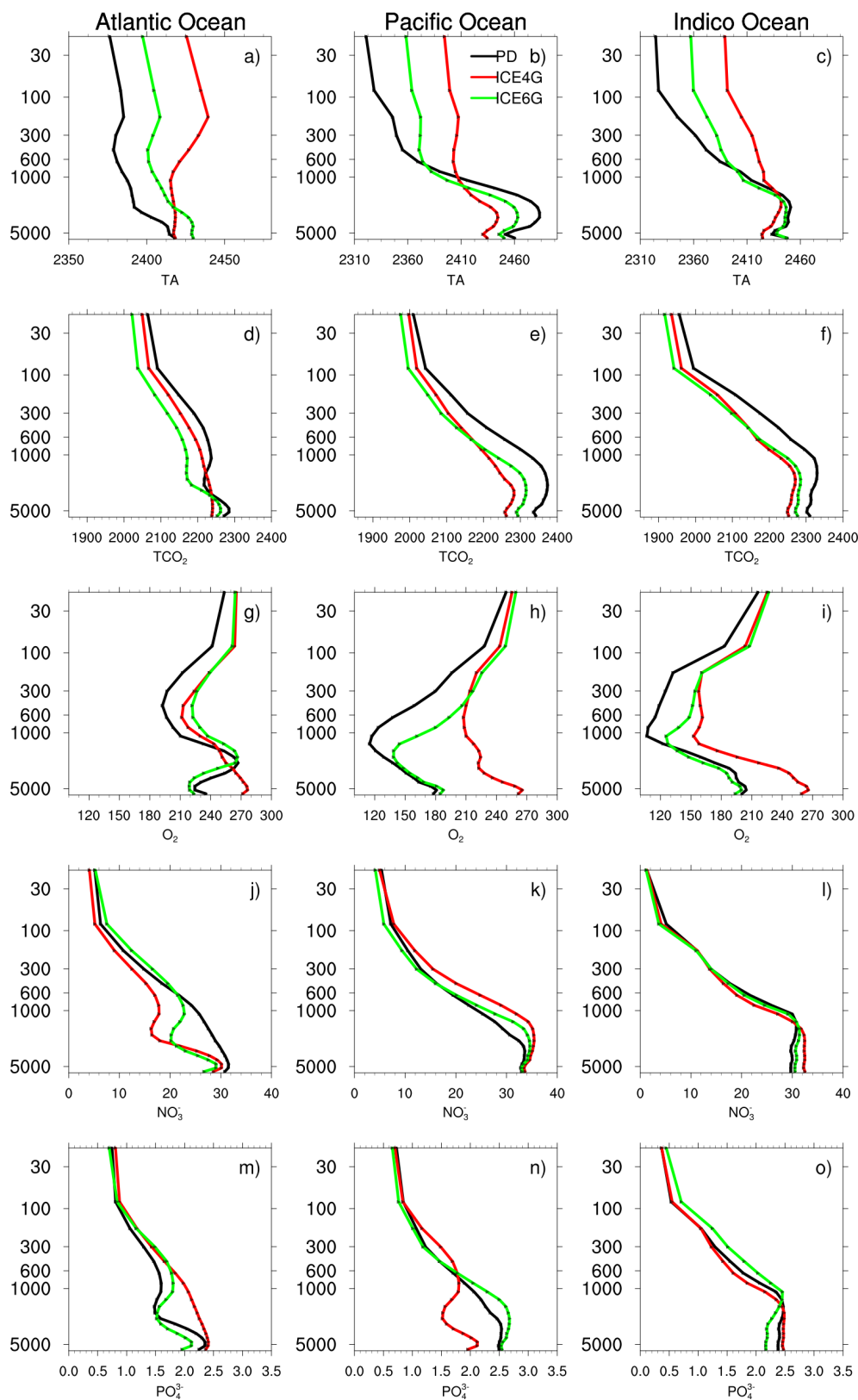


Figura 2.8: Global ocean basin average vertical profile of TA $\mu\text{mol/kg}$, TCO₂ $\mu\text{mol/kg}$, O₂ $\mu\text{mol/kg}$, NO₃ $\mu\text{mol/kg}$ and PO₄³⁻ $\mu\text{mol/kg}$ from simulations of PD, ICE6G and ICE4G.

interior, which is partially controlled by atmospheric $p\text{CO}_2$ (Sigman et al., 2010). The oceanic nutrients and export production increases at the level of atmospheric $p\text{CO}_2$ decrease, despite the export production being also limited by light, Fe/Si and restricting the impact of changes in nutrients on atmospheric $p\text{CO}_2$ (Rosell-Melé et al., 2007).

2.4 Climate Variability

2.4.1 Global Wind Stress Variability and the Oceanic Biogeochemistry

In order to investigate the spatial variability associated with the leading pattern of the zonal wind stress, empirical orthogonal functions (EOF) have been applied globally and regression analysis was applied upon atmospheric and oceanic variables for the LGM and PD simulations. Differences in the regressed pattern of the wind stress show a very well-marked dipole pattern in the North Pacific with positive anomalies between 40°N and 60°N , and a negative signal 20°N and 30°N (Figure 2.9). A tripole-like pattern is seen in the Indian Ocean with positive anomalies in the southern region over the 30°S latitudinal belt. It is also clear that the introduction of the ICE-6G topography induces a strengthening of the wind stress in the north Atlantic and over the subtropical Pacific Ocean (Figure 2.9a,b).

The regression between the first principal component (PC) of the zonal wind stress and ocean components are shown in Figure 2.9 and for the carbonate system in Figure 2.10. Changes of SST induced by the main wind pattern show that the

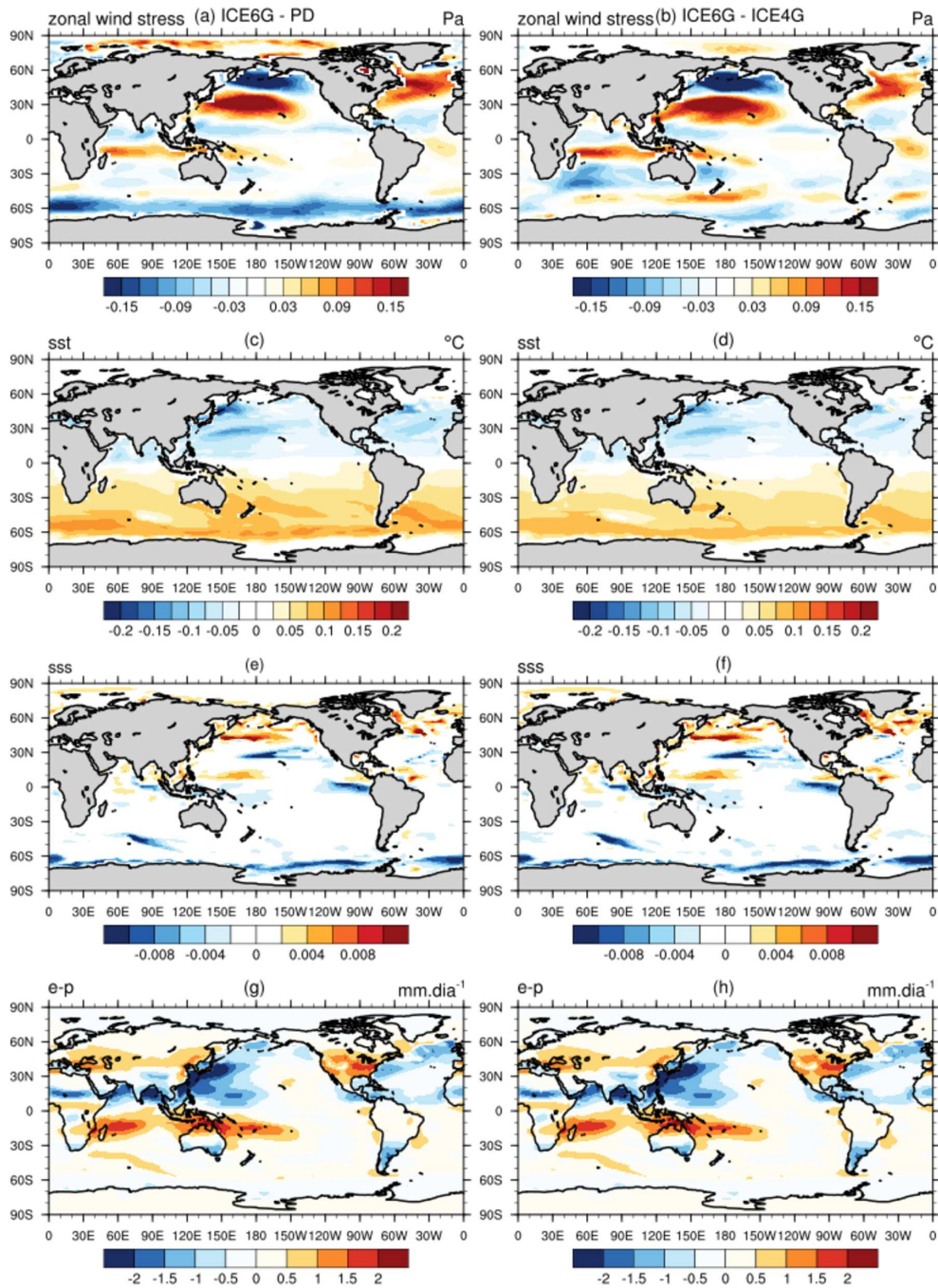


Figure 2.9: Global response associated with the 1st EOF related to zonal wind stress. The pattern are displayed by amplitudes by regressing; (a) wind stress (Pa), (b) SST (°C), (c) SSS and (g) E-P flux anomalies upon the standardized first principal component time series.

presence of the ICE6G with respect to the PD topography induces lower temperature in the Northern Hemisphere (Fig. 2.9c). Whereas higher temperatures are delivered in parts of Southern Hemisphere, positive anomalies between the LGM

and PD climate have proposed by the GLAMAP reconstructions (Sarnthein et al., 2003) and (Justino et al., 2005). It may be argued that the ICE6G buoyancy forcing induces intensified westerly flow, leading to enhanced upwelling and evaporating cooling which result in lower SST. However, the SH warming resembles a response to the seesaw effect characteristic of the LGM epoch under weaker thermohaline flow (Stocker, 1998). We argue that in case of strong winds in the NH a slowdown of the westerly flow occurs in the SH, reducing the Ekman circulation and the evaporative cooling leading to positive SST anomalies. Similarly, by comparing the ICE6G and ICE4G simulations (Fig. 2.9d) the magnitude anomalies in the SH are smaller than those between ICE6G and PD. This should be expected because changes in the glacial topographies, though important, are smooth with respect to ICE5G and ICE4G. Salinity anomalies induced by the dominant wind pattern demonstrated that changes are larger in the Nordic Seas and northern Pacific for both anomalous conditions, the ICE6G minus PD, and ICE6G minus ICE4G experiments (Fig 2.9e,f).

The regression of the wind stress 1st PC on the E-P flux differs between PD and ICE4G, in respect to the ICE6G run (Fig. 2.9g,h). In fact, larger changes are found in the equatorial region of the Pacific and Indian Ocean. Over the subtropical western Pacific and Atlantic, precipitation in the ICE6G run is higher than that delivered by the PD and the ICE4G simulations. This is related to stronger meridional thermal gradients. The opposite is true in the equatorial Pacific and Indian oceans where the ICE6G is drier than PD and the ICE4G (Fig. 2.9g,h).

Figure 2.10 shows the variations of total alkalinity (TA) and dissolved inorganic carbon (TCO₂) in response to the 1st PC of the global wind stress. It is demonstra-

ted that the TA and TCO₂ do not follow the SST, SSS or E-P flux regression patterns (Fig. 2.9). In fact local features are dominant in which larger variations of both TA and TCO₂ are found in the equatorial region. Those regions in the equatorial Pacific (warming pool and the cold tongue) deliver the largest positive anomalies of the E-P flux between the ICE6G and PD simulations (Fig. 2.4e). It has to be mentioned, moreover, that changes in the equatorial air-sea interaction (Bjerknes feedback) modify the photosynthesis, respiration and phytoplankton concentration as demonstrated by (Marzeion et al., 2005).

Turning to the NO₃⁻ differences between the ICE6G and PD runs, remarkable changes occur in the vicinity of the Antarctic continent (Fig 2.10e) and in the Northern Hemisphere extratropical oceans. In the northern Pacific the NO₃⁻ and wind stress are in phase in the sense that positive wind anomalies are accompanied by increased NO₃⁻ (Fig 2.10a). However, in the North Atlantic changes in NO₃⁻ match negative SST and E-P flux anomalies (Fig. 2.10e and Fig. 2.9c,g) but is negatively correlated to the wind stress dominant pattern (Figs. 2.9a, 2.10e).

Strictly speaking, the regression anomalies between ICE6G and ICE4G show a strong pattern in the Indian Ocean region, particularly in the region of Bengal Bay, which is dominated by high salinity during the LGM (Prell et al., 1980), and the Arabian Sea region for TA, TCO₂ and both nutrients (Fig.2.10 a-e). Distinct processes affect the TA and TCO₂ however, for the LGM interval, changes in water dilution caused by evaporation and precipitation (Millero et al., 2006) are candidate to play the major role. This is also clear in the North Pacific and Atlantic.

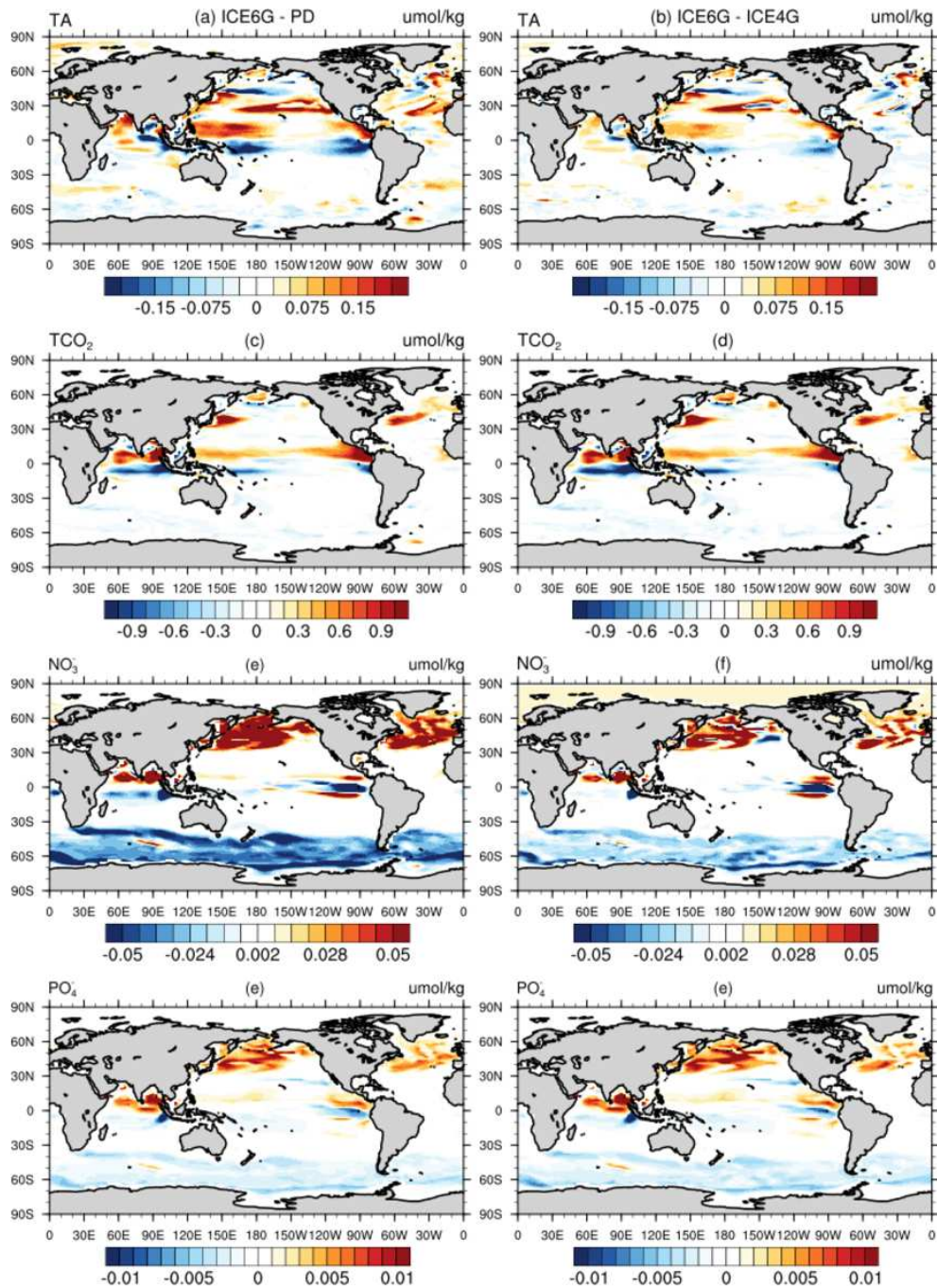


Figura 2.10: Same as in Fig. 6 but for surface (a)TA ($\mu\text{mol}/\text{kg}$), (b)TCO₂ ($\mu\text{mol}/\text{kg}$), (c) NO₃⁻ ($\mu\text{mol}/\text{kg}$) and (d) PO₄³⁻ ($\mu\text{mol}/\text{kg}$).

2.4.2 The Pacific Decadal Oscillation and the Oceanic Biogeochemistry

The Pacific Decadal Oscillation (PDO) is calculated based on EOF applied to SST in the North Pacific (20 °N - 60 °N, 110 °E - 260 °E, (Mantua and Hare, 2002)) for

Capítulo 2

the LGM and PD experiments. The PDO is the dominant mode of multidecadal variability in the NH (Fig. 2.11). During the warm phase of the PDO, positive SST anomalies are seen in the central Pacific accompanied by cold conditions in the northwestern Pacific. Figure 2.12 shows that the inclusion of the LGM Paleotopography does not induce substantial changes to the PDO, as reproduced by the PD, ICE6G and ICE4G simulations. However, SST anomalies (Fig. 2.11d,e) depicted by the ICE6G run are enhanced with respect to both PD and ICE4G conditions.

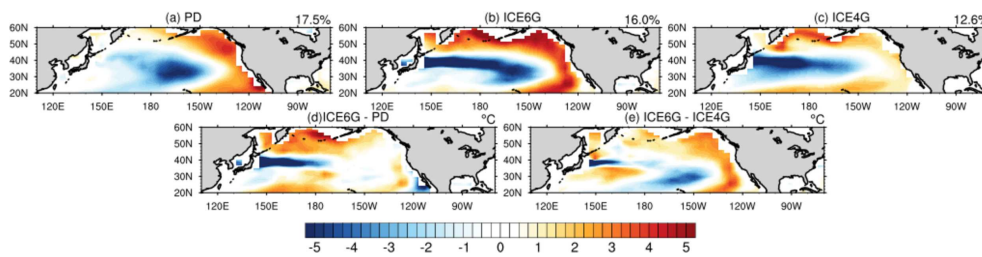


Figura 2.11: First component of the PDO (a) PD, (b) ICE6G and (c) ICE4G simulations. Regression anomalies between ICE6G and PD (d) simulations and ICE6G and ICE4G simulations (e). The top-right percentage values represent the respective explained variance of the first EOF.

Differences in the regression pattern between the ICE6G and PD induced by changes in the PDO are discussed in Figures 2.11 and 2.12. By observing the SST pattern (Fig. 2.12a), it is notable that during the warm phase of the PDO for the LGM interval, higher SST appears in the eastern subtropical and north Pacific, and in the vicinity of the European and African coast. It is very interesting that differences in the regression pattern of SSS (Fig. 2.12b) are very similar those found for the SST. But there is no clear relationship with the EP flux (Fig. 2.12c).

Figure 2.12d shows the wind differences. It is demonstrated that the ICE6G PDO speeds up the wind flow in the extratropics but slows down the circulation in the subtropics. The intensive westerlies are associated with warm water transport from the subtropical gyre to the northeastern Pacific, which reduces the influence

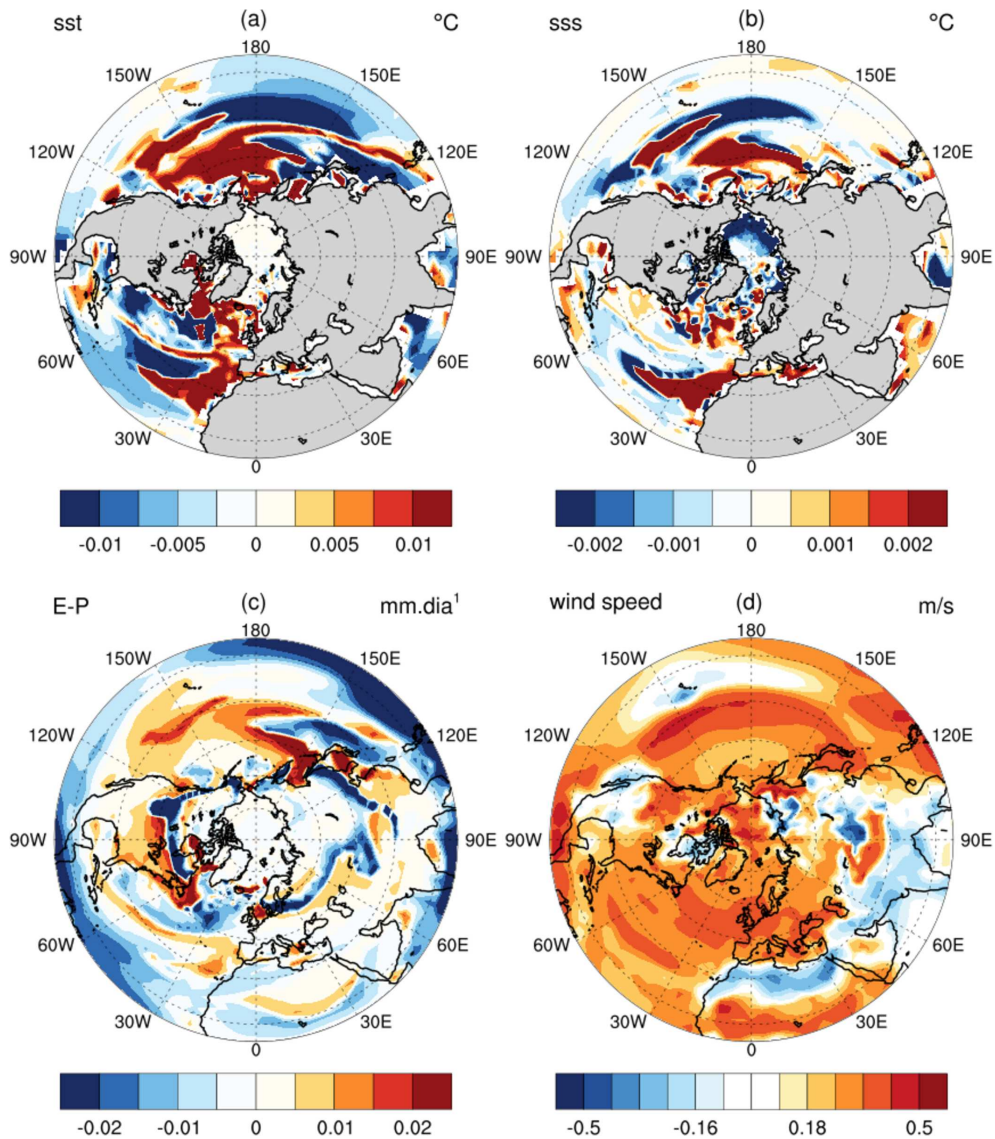


Figura 2.12: Regression anomalies between for ICE6G and PD simulations (a) SST, (b) SSS, (c) E-P flux and (d) wind speed. These pattern are shown by regressing the 1st PC of the PDO onto the SST, SSS, E-P flux and wind speed.

of upwelled much cooler waters. The influence of the PDO to the carbonate system is shown in Figure 2.13. For TA a good match is found with SST and SSS in the Atlantic (Fig.2.12a,b) and the subtropical Pacific. The match between the TCO_2 and SST/SSS is not as clear because the pattern exhibits more dominant mesoscale features (Fig.2.13b). However, in the extratropics, the patterns of TA and TCO_2 and also for nutrients are significantly higher in ICE6G as compared to PD (Fig. 2.13). It is important to mention that the deepening of the mixed layer associated with

increased westerlies over the western Pacific increases the nutrient concentrations, through the upwelling of subsurface rich nutrients water (Yasunaka et al., 2016). In the Arctic region, the low salinity leads to a strong vertical stratification that decreases TA values. The largest variations between ICE6G and PD were found in the Pacific and North Atlantic, Indian Ocean and this is also reflected for nutrients (Fig. 2.13c, d).

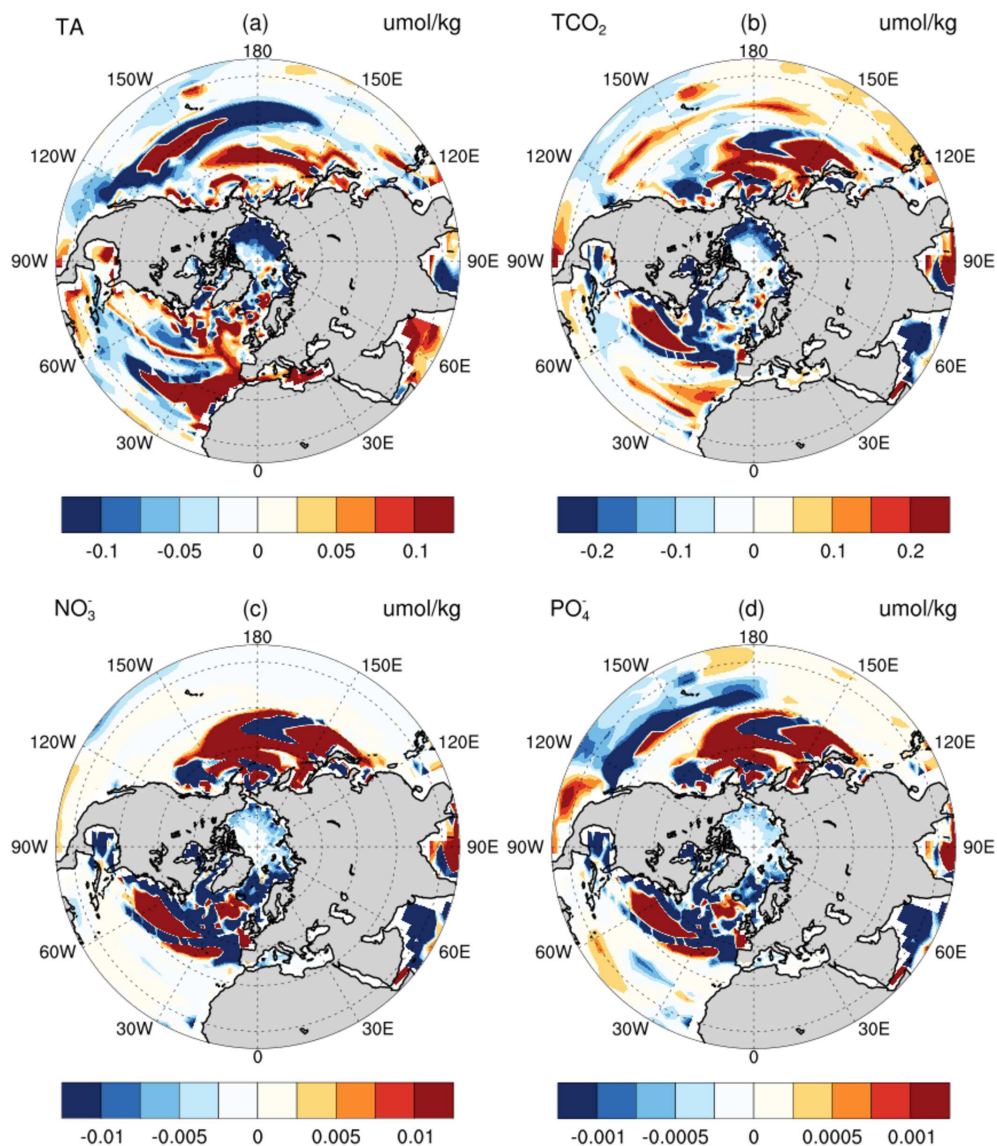


Figura 2.13: Same as figure 8 but for surface (a) TA, (b) TCO_2 , (c) NO_3^- and (d) PO_4^{3-}

Turning to analyses of the nutrients (Fig. 2.13c, d) it is observed that remarkable

changes between the ICE6G and PD runs occur in the Pacific Ocean. It shows higher values for the Northern Pacific region and negative anomalies in the Arabian Sea and Equatorial Pacific as response of the PDO 1st PC.

2.5 Summary and concluding remarks

This study is focused on understanding the effects of a new topography (ICE6G (Argus et al., 2014; Peltier et al., 2015)) on the Last Glacial Maximum, and how it influences the oceanic carbonate system. Three simulations were performed with the UVic ESCM 2.9 (Weaver et al., 1998; Eby et al., 2013); the first simulation applies the concentration of CO₂ of 380ppm and the current orbital configurations; the second simulation includes the ice sheet topography ICE4G (Peltier, 1994) and the orbit configurations of the LGM (Berger and Loutre, 1991), and the third simulation was carried out with the ICE6G ice sheet topography (Argus et al., 2014; Peltier et al., 2015) and the orbital configurations of the LGM (Berger and Loutre, 1991).

The comparison between the two ice sheet topographies delivered significant differences due to increased topography height in the North America region and decrease in the region of Greenland in the ICE6G, resulting in a cooling in North America and warming over Greenland. This increased topography height and cooling in the ICE6G simulation leads to a strengthening of the wind stress, which impacts the rate of water mass formation. Even with the simplified atmosphere model, the UVic ESCM was able to simulate increased temperature in the North Atlantic in the ICE6G with respect the other topographies simulations (ICE5G and ICE4G), as found by (Justino et al., 2006; Vettoretti and Peltier, 2013).

A weakening and shift of the MOC is observed accompanied by a major intrusion of deep MOC cell northward to the North Atlantic being coherent with data that suggests a decrease in AMOC ventilation and circulation during the LGM (McManus et al., 2004). This feature seems to be one of the main mechanisms res-

possible for the small variation of nutrients in the glacial periods. The differences can also be seen in the vertical profile in the different ocean basins, the LGM simulations throughout the water column are compatible with the results found in the literature, such as lower temperature, higher salinity resulting in higher concentrations of TA and less than TCO_2 . However, large differences are found between ICE6G and ICE4G simulations for salinity in the Pacific and Indian Ocean basins which were larger by about 0.9 psu in ICE4G than in ICE6G. In agreement with the highest ice concentration in the Eastern Antarctica in ICE4G than ICE6G run.

In glacial periods, the increase of the surface alkalinity and the decrease of the surface TCO_2 , are caused by the decrease in pCO_2 concentrations. As the UVic has the sediment scheme coupled with the oceanic model, it is argue that the decrease of burial CaCO_3 is related to the changes in the sediments . Higher alkalinity anomalies were found in the deep ocean between ICE6G and ICE4G simulations and can be linked with higher salinity in Pacific and Indian Basins. On the other hand, the Atlantic Basin shows slightly higher concentration in the deep ocean nutrients for ICE6G simulation than ICE4G.

The nutrient anomaly fields obtained by regressing the dominant PDO mode onto TCO_2 , NO_3^- and PO_4^{3-} show similar spatial distribution, with negative anomalies in the Alaska gyre but positive anomalies in the western subarctic region. In the North Atlantic great variability is found in the GIN seas, with negative anomalies for both nutrients and TCO_2 , however, TA presented positive values, following induced salinity pattern. The subtropical region experiences large anomalies for both TA and TCO_2 , but little changes for NO_3^- is related to the PDO positive phase, which is related to induced changes in salinity and E-P flux.

Referências Bibliográficas

- Annan, J. D. and Hargreaves, J. C. (2013). A new global reconstruction of temperature changes at the Last Glacial Maximum. *Climate of the Past*, 9(1):367–376.
- Archer, D. (1996). A data-driven model of the global calcite lysocline. *Global Biogeochemical Cycles*, 10(3):511–526.
- Argus, D. F., Peltier, W. R., Drummond, R., and Moore, A. W. (2014). The Antarctica component of postglacial rebound model ICE-6G_C (VM5a) based on GPS positioning, exposure age dating of ice thicknesses, and relative sea level histories. *Geophysical Journal International*, 198(1):537–563.
- Bates, N., Astor, Y., Church, M., Currie, K., Dore, J., Gonaález-Dávila, M., Lorenzoni, L., Muller-Karger, F., Olafsson, J., and Santa-Casiano, M. (2014). A Time-Series View of Changing Ocean Chemistry Due to Ocean Uptake of Anthropogenic CO₂ and Ocean Acidification. *Oceanography*, 27(1):126–141.
- Berger, A. and Loutre, M. (1991). Insolation values for the climate of the last 10 million years. *Quaternary Science Reviews*, 10(4):297–317.
- Broecker, W. S. (1986). Oxygen isotope constraints on surface ocean temperatures. *Quaternary Research*, 26(1):121–134.
- Buchanan, P. J., Matear, R. J., Lenton, A., Phipps, S. J., Chase, Z., and Etheridge, D. M. (2016). The simulated climate of the Last Glacial Maximum and insights into the global marine carbon cycle. *Climate of the Past*, 12(12):2271–2295.

- Deser, C., Phillips, A., Bourdette, V., and Teng, H. (2012). Uncertainty in climate change projections: The role of internal variability. *Climate Dynamics*, 38(3-4):527–546.
- Eby, M., Weaver, A. J., Alexander, K., Zickfeld, K., Abe-Ouchi, A., Cimadoribus, A. A., Crespin, E., Drijfhout, S. S., Edwards, N. R., Eliseev, A. V., Feulner, G., Fichefet, T., Forest, C. E., Goosse, H., Holden, P. B., Joos, F., Kawamiya, M., Kicklighter, D., Kienert, H., Matsumoto, K., Mokhov, I. I., Monier, E., Olsen, S. M., Pedersen, J. O., Perrette, M., Philippon-Berthier, G., Ridgwell, A., Schlosser, A., Von Deimling, T. S., Shaffer, G., Smith, R. S., Spahni, R., Sokolov, A. P., Steinacher, M., Tachiiri, K., Tokos, K., Yoshimori, M., Zeng, N., and Zhao, F. (2013). Historical and idealized climate model experiments: An intercomparison of Earth system models of intermediate complexity. *Climate of the Past*, 9(3):1111–1140.
- Eby, M., Zickfeld, K., Montenegro, A., Archer, D., Meissner, K. J., and Weaver, A. J. (2009). Lifetime of Anthropogenic Climate Change: Millennial Time Scales of Potential CO₂ and Surface Temperature Perturbations. *Journal of Climate*, 22(10):2501–2511.
- Ewen, T. L., Weaver, A. J., and Eby, M. (2004). Sensitivity of the inorganic ocean carbon cycle to future climate warming in the UVic coupled model. *Atmosphere - Ocean*, 42(1):23–42.
- Fairbanks, R. G. (1989). A 17,000-year glacio-eustatic sea level record: influence of glacial melting rates on the Younger Dryas event and deep-ocean circulation. *Nature*, 342(6250):637–642.

- Fanning, A. F. and Weaver, A. J. (1997). A horizontal resolution and parameter sensitivity study of heat transport in an idealized coupled climate model. *Journal of Climate*, 10(10):2469–2478.
- Farrell, J. W., Pedersen, T. F., Calvert, S. E., and Nielsen, B. (1995). Glacial–interglacial changes in nutrient utilization in the equatorial Pacific Ocean. *Nature*, 377(6549):514–517.
- Ferrari, R., Jansen, M. F., Adkins, J. F., Burke, A., Stewart, A. L., and Thompson, A. F. (2014). Antarctic sea ice control on ocean circulation in present and glacial climates. *Proceedings of the National Academy of Sciences*, 111(24):8753–8758.
- Handiani, D., Paul, A., Prange, M., Merkel, U., Dupont, L., and Zhang, X. (2013). Tropical vegetation response to Heinrich Event 1 as simulated with the UVic ESCM and CCSM3. *Climate of the Past*, 9(4):1683–1696.
- Justino, F., Kucharski, F., Lindemann, D., Wilson, A., and Stordal, F. (2018). A modified seasonal cycle during MIS31 superinterglacial favors stronger ENSO variability. *Climate of the Past Discussions*, pages 1–22.
- Justino, F. and Peltier, W. R. (2008). Climate anomalies induced by the Arctic and Antarctic Oscillations: Glacial Maximum and present-day perspective. *Journal of Climate*, 21(3):459–475.
- Justino, F., Timmermann, A., Merkel, U., and Peltier, W. R. (2006). An initial inter-comparison of atmospheric and oceanic climatology for the ICE-5G and ICE-4G models of LGM paleotopography. *Journal of Climate*, 19(1):3–14.

- Justino, F., Timmermann, A., Merkel, U., and Souza, E. P. (2005). Synoptic reorganization of atmospheric flow during the last glacial maximum. *Journal of Climate*, 18(15):2826–2846.
- Key, R. M., Olsen, A., van Heuven, S., Lauvset, S. K., Velo, A., Lin, X., Schirnack, C., Kozyr, A., Tanhua, T., and Hoppema, M. (2015). Global Ocean Data Analysis Project, Version 2 (GLODAPv2). ORNL/CDIAC- 162, NDP-093. Carbon Dioxide Information Analysis Center, Oak Ridge National Laboratory, US Dept. of Energy, Oak Ridge, Tennessee. doi: 10.3334/CDIAC/OTG.NDP093_GLODAPv2, 2.
- Kohfeld, K., Quéré¹, C. L., Harrison¹, S. P., and Anderson, R. F. (2005). Role of Marine Biology in Glacial-Interglacial CO₂ Cycles. *Science*, 308(5718):74–78.
- Mantua, N. and Hare, S. (2002). Mantua2001.pdf. *Journal of Oceanography*, 58(1):35–44.
- Martin, J. H. (1990). Glacial-interglacial CO₂ change: The Iron Hypothesis. *Paleoceanography*, 5(1):1–13.
- Marzeion, B., Timmermann, A., Murtugudde, R., and Jin, F. F. (2005). Biophysical feedbacks in the tropical Pacific. *Journal of Climate*, 18:58–70.
- Matthews, H. D. (2006). Emissions targets for CO₂ stabilization as modified by carbon cycle feedbacks. *Tellus, Series B: Chemical and Physical Meteorology*, 58(5):591–602.
- McElroy, M. B. (1983). Marine biological controls on atmospheric CO₂ and climate. *Nature*, 302(5906):328–329.

- McManus, J. F., Francois, R., Gherardl, J. M., Kelgwin, L., and Drown-Leger, S. (2004). Collapse and rapid resumption of Atlantic meridional circulation linked to deglacial climate changes. *Nature*, 428(6985):834–837.
- Meissner, K. J., Weaver, A. J., Matthews, H. D., and Cox, P. M. (2003). The role of land surface dynamics in glacial inception: A study with the UVic Earth System Model. *Climate Dynamics*, 21(7-8):515–537.
- Millero, F. J., Graham, T. B., Huang, F., Bustos-Serrano, H., and Pierrot, D. (2006). Dissociation constants of carbonic acid in seawater as a function of salinity and temperature. *Marine Chemistry*, 100(1-2):80–94.
- Muglia, J. and Schmittner, A. (2015). Glacial Atlantic overturning increased by wind stress in climate models. *Geophysical Research Letters*, 42(22):9862–9869.
- Negre, C., Zahn, R., Thomas, A. L., Masqué, P., Henderson, G. M., Martínez-Méndez, G., Hall, I. R., and Mas, J. L. (2010). Reversed flow of Atlantic deep water during the Last Glacial Maximum. *Nature*, 468(7320):84–88.
- Oka, A., Abe-Ouchi, A., Chikamoto, M. O., and Ide, T. (2011). Mechanisms controlling export production at the LGM: Effects of changes in oceanic physical fields and atmospheric dust deposition. *Global Biogeochemical Cycles*, 25:1–12.
- Olsen, A., Key, R. M., Van Heuven, S., Lauvset, S. K., Velo, A., Lin, X., Schirnick, C., Kozyr, A., Tanhua, T., Hoppema, M., Jutterström, S., Steinfeldt, R., Jeansson, E., Ishii, M., Pérez, F. F., and Suzuki, T. (2016). The global ocean data analysis project version 2 (GLODAPv2) - An internally consistent data product for the world ocean. *Earth System Science Data*, 8(2):297–323.

- Orr, J. C. (1999). On ocean carbon-cycle model comparison. *Tellus, Series B: Chemical and Physical Meteorology*, 51(2):509–510.
- Orr, J. C. and Epitalon, J. M. (2015). Improved routines to model the ocean carbonate system: Mocsy 2.0. *Geoscientific Model Development*, 8(3):485–499.
- Pacanowski, R. C. (1995). MOM 2 Documentation, users guide and reference manual, GFDL Ocean Group Technical Report 3. *Geophys. Fluid Dyn. Lab., Princeton University, Princeton, NJ.*, 0.
- Peltier, W. (2004). GLOBAL GLACIAL ISOSTASY AND THE SURFACE OF THE ICE-AGE EARTH: The ICE-5G (VM2) Model and GRACE. *Annual Review of Earth and Planetary Sciences*, 32(1):111–149.
- Peltier, W. R. (1994). Ice Age Paleotopography. *Science*, 265(5169):195–201.
- Peltier, W. R. (2002). On eustatic sea level history: Last Glacial Maximum to Holocene. *Quaternary Science Reviews*, 21(1-3):377–396.
- Peltier, W. R., Argus, D. F., Drummond, R., Strange, A., Peltier, W. R., Argus, D. F., Drummond, R., Shahnas, M. H., Yuen, D. A., Pysklywec, R. N., Peltier, W. R., Argus, D. F., Drummond, R., Tarayoun, A., Audet, P., Mazzotti, S., Ashoori, A., Peltier, W. R., Argus, D. F., and Drummond, R. (2015). Journal of Geophysical Research : Solid Earth. *Journal of Geophysical Research: Solid Earth*, 2015(120):450–487.
- Peltier, W. R. and Fairbanks, R. G. (2006). Global glacial ice volume and Last Glacial Maximum duration from an extended Barbados sea level record. *Quaternary Science Reviews*, 25(23-24):3322–3337.

- Petit, J. R., Jouzel, J., Raynaud, D., Barkov, N. I., Barnola, J.-M., Basile, I., Bender, M., Chappellaz, J., Davis, M., Delaygue, G., Delmotte, M., Kotlyakov, V. M., Legrand, M., Lipenkov, V. Y., Lorius, C., Pépin, L., Ritz, C., Saltzman, E., and Stievenard, M. (1999). Climate and atmospheric history of the past 420,000 years from the Vostok ice core, Antarctica. *Nature*, 399(6735):429–436.
- Prell, W. L., Hutson, W. H., Williams, D. F., Bé, A. W., Geitzenauer, K., and Molfino, B. (1980). Surface circulation of the Indian Ocean during the last glacial maximum, approximately 18,000 yr B.P. *Quaternary Research (United States)*, 14(3):309–336.
- Rickaby, R. E., Elderfield, H., Roberts, N., Hillenbrand, C. D., and Mackensen, A. (2010). Evidence for elevated alkalinity in the glacial Southern Ocean. *Paleoceanography*, 25(1):1–15.
- Rind, D. (1987). Components of the Ice Age circulation. *Journal of Geophysical Research*, 92(D4):4241–4281.
- Rojas, M. (2013). Sensitivity of Southern Hemisphere circulation to LGM and $4 \times \text{CO}_2$ climates. *Geophysical Research Letters*, 40(5):965–970.
- Rosell-Melé, A., Escala, M., Martínez-García, A., and Núñez, N. (2007). Drivers of atmospheric CO_2 concentrations over glacial to interglacial time scales. *Contributions to Science*, 3(3):395–404.
- Sarnthein, M., Gersonde, R., Niebler, S., Pflaumann, U., Spielhagen, R., Thiede, J., Wefer, G., and Weinelt, M. (2003). Overview of Glacial Atlantic Ocean Mapping (GLAMAP 2000). *Paleoceanography*, 18(2):n/a–n/a.

- Schartau, M. and Oschlies, A. (2004). Simultaneous data-based optimization of a 1D-ecosystem model at three locations in the North Atlantic: Part I—Method and parameter estimates. *Journal of Marine Research*, 61(6):765–793.
- Scheffer, M., Bascompte, J., Brock, W. A., Brovkin, V., Carpenter, S. R., Dakos, V., Held, H., Van Nes, E. H., Rietkerk, M., and Sugihara, G. (2009). Early-warning signals for critical transitions. *Nature*, 461(7260):53–59.
- Schmittner, A. and Galbraith, E. D. (2008). Glacial greenhouse-gas fluctuations controlled by ocean circulation changes. *Nature*, 456(7220):373–376.
- Schmittner, A., Oschlies, A., Giraud, X., Eby, M., and Simmons, H. L. (2005). A global model of the marine ecosystem for long-term simulations: Sensitivity to ocean mixing, buoyancy forcing, particle sinking, and dissolved organic matter cycling. *Global Biogeochemical Cycles*, 19(3):1–17.
- Schmittner, A., Urban, N. M., Shakun, J. D., Mahowald, N. M., Clark, P. U., Bartlein, P. J., Mix, A. C., and Rosell-Melé, A. (2011). Climate sensitivity estimated from temperature reconstructions of the Last Glacial Maximum. *Science*, 334(6061):1385–1388.
- Sigman, D. M. and Boyle, E. A. (2000). Glacial/interglacial variations in atmospheric carbon dioxide. *Nature*, 407(6806):859–869.
- Sigman, D. M., Hain, M. P., and Haug, G. H. (2010). The polar ocean and glacial cycles in atmospheric CO₂ concentration. *Nature*, 466(7302):47–55.
- Stocker, T. F. (1998). The seesaw effect. *Science*, 282(5386):61–62.

- Tamburini, F. and Föllmi, K. B. (2009). Phosphorus burial in the ocean over glacial-interglacial time scales. *Biogeosciences*, 6(4):501–513.
- Tarasov, L. and Richard Peltier, W. (2002). Greenland glacial history and local geodynamic consequences. *Geophysical Journal International*, 150(1):198–229.
- Vettoretti, G. and Peltier, W. R. (2013). Last Glacial Maximum ice sheet impacts on North Atlantic climate variability: The importance of the sea ice lid. *Geophysical Research Letters*, 40(24):6378–6383.
- Wania, R., Meissner, K. J., Eby, M., Arora, V. K., Ross, I., and Weaver, A. J. (2012). Carbon-nitrogen feedbacks in the UVic ESCM. *Geoscientific Model Development*, 5(5):1137–1160.
- Watson, A. J. and Naveira Garabato, A. C. (2006). The role of Southern Ocean mixing and upwelling in glacial-interglacial atmospheric CO₂ change. *Tellus, Series B: Chemical and Physical Meteorology*, 58(1):73–87.
- Weaver, A. J., Eby, M., Fanning, A. F., and Wiebe, E. C. (1998). Simulated influence of carbon dioxide, orbital forcing and ice sheets on the climate of the Last Glacial Maximum. *Nature*, 394(6696):847–853.
- Weber, S. L., Drijfhout, S. S., Abe-Ouchi, A., Crucifix, M., Eby, M., Ganopolski, A., Murakami, S., Otto-Bliesner, B., and Peltier, W. R. (2007). The modern and glacial overturning circulation in the Atlantic ocean in PMIP coupled model simulations. *Climate of the Past*, 3(1):51–64.
- Yasunaka, S., Ono, T., Nojiri, Y., Whitney, F. A., Wada, C., Murata, A., Nakaoka, S.,

and Hosoda, S. (2016). Long-term variability of surface nutrient concentrations in the North Pacific. *Geophysical Research Letters*, 43(7):3389–3397.

Yokoyama, Y., Lambeck, K., De Deckker, P., Johnston, P., and Fifield, L. K. (2000). Timing of the Last Glacial Maximum from observed sea-level minima. *Nature*, 406(6797):713–716.

Yu, J., Anderson, R. F., Jin, Z., Rae, J. W., Opdyke, B. N., and Eggins, S. M. (2013). Responses of the deep ocean carbonate system to carbon reorganization during the Last Glacial-interglacial cycle. *Quaternary Science Reviews*, 76:39–52.

Southern Ocean response to Glacial and Interglacial Forcing

Noele F. Leonardo¹

¹Universidade Federal de Viçosa, Departamento de Engenharia Agrícola, Viçosa, Minas Gerais, Brasil

Flavio B. Justino¹

¹Universidade Federal de Viçosa, Departamento de Engenharia Agrícola, Viçosa, Minas Gerais, Brasil

Alessandra L. Fonseca²

² Universidade Federal de Santa Catarina, Coordenadoria Especial de Oceanografia, Florianópolis, Santa Catarina, Brasil

Juan Muglia³

³College of Earth, Ocean, and Atmospheric Sciences, Oregon State University, Corvallis, Oregon, USA

ARTIGO SUBMETIDO

Abstract

The Southern Ocean are particularly vulnerable to climate changes. Atmospheric CO₂ fluctuations have been highly correlated with climate on million years time scales, or caused or at least amplified, the climatic changes. Thus, two simulations were done with the UVic ESCM 2.9 model for the LGM and MIS11c climate using orbital forcing and CO₂ prescribed for the ages. We have clearly identified the differences between the decrease and increase of CO₂ concentration in the Southern Ocean. The LGM simulation, produces a colder, saltier and more alkaline Southern Ocean than MIS11c. The MIS11c simulations, shows a reduced in O₂ content with respect to LGM may relative with less primary productivity and more CaCO₃ dissolution. According MIS11c simulation, surface ocean carbonate factory is expected to be more sensitive to a carbon oscillations due to increasing in the CO₂ dissolved in sea water. As expected, It will decrease the pH due to decreased alkalinity and ion carbonate concentrations. In this scenario, the aragonite concentration in the deep sediments would be more vulnerable to dissolution as a response of shoaling of depth of aragonite saturation . The increase of CO₂ dissolved in sea water in MIS11c, decrease the pH and saturation depth of CaCO₃ becomes more than 1000 meters shallower than found in the LGM simulation. This implies in a negative feedback of CO₂ absorption with saturation horizon becoming shallower, less Souther Ocean capacity has to uptake atmospheric CO₂. Since the CaCO₃ formation in the surface ocean and the dissolution in the deeper both affect TCO₂ and TA as also the pCO_2 . Our results indicated that, under high CO₂ conditions the surface of Southern Ocean appears to be more sensitive to a carbon perturbation, generally due to decrease of ion carbonate concentration that leads a changes in the carbonate buffer system that will results in a deepening more than 1000 m the aragonite depth saturation in relation to MIS11c results..

3.1 Introduction

The Pleistocene occurs between 2.6 ma and 10 ka ago and is distinguished by oscillations between cold glacial and the warmer interglacial periods ([Shackleton and Pisias, 2013](#)). Changes in the orbital forcing and CO₂ concentrations are the main drivers of these cycles. Ice core records have shown that atmospheric CO₂ concentration has diversified between 50 - 100 ppm during the climate cycles of the last 800 ka ([Bereiter et al., 2015](#)).

The most recent changes in CO₂ concentrations occurred in the last 12 ky BP, between the end of the Last Glacial Maximum (LGM) and before the pre-industrial era, suggesting that the atmosphere and oceans were in a state of quasi - equilibrium in the concentrations of CO₂ pressure. The interglacials before 430 ka such as Marine Isotope Stage (MIS) 13, 15, 17 and 19 are described by relatively lower atmospheric CO₂ (240 ppm), the most recent interglacials, MIS1, 5, 9 e 11 with slightly higher CO₂ level (280ppm) ([Lüthi et al., 2008](#)).

The LGM is particularly important because of its maximum ice cover ([Lowell et al., 1995](#)), with the lower quaternary sea level, about 135 m below that with respect to today ([Mix et al., 2001](#)) and CO₂ concentrations by about 185ppm ([Clark et al., 2009](#)). Between the interglacials that occurred in the Pleistocene, special attention is given to the MIS11c. It was the longest interglacial (409 and 423 ka), characterized by low eccentricity and obliquity ([Melles et al., 2012](#); [Coletti et al., 2015a](#)). The CO₂ concentrations were approximately 285ppm. The MIS11c has been receiving attention because it may represent the future changes in the human induced climate ([Tzedakis, 2010](#); [Coletti et al., 2015a](#)).

Since the future climate changes are expected to be more pronounced in the polar regions (IPCC, 2014), the investigation of past environmental changes is a key issue to elucidate future climate changes, especially in a warming world. The relationship of atmospheric CO₂ with balance between biological productivity and ventilation of the deep Southern Ocean pointing to the leading role of the high-latitude oceans as controller of natural CO₂ concentrations (Sarmiento and Toggweiler, 1984).

The oceans are the largest reservoirs of CO₂ which essentially determine the atmospheric CO₂ concentrations. In addition, the exchange between biologic processes and oceanic circulation determine the vertical and horizontal gradients of nutrient and carbon concentrations.

The CO₂ absorbed from the atmosphere is reserved as total dissolved inorganic carbon (TCO₂), organic carbon (C_{org}) and calcium carbonate (CaCO₃). It has been mentioned that the CO₂ its ability to dissolve in seawater is directly related to its pressure in the atmosphere and the density of the surface water, determined by temperature and salinity. Oceanic CO₂ time series show that the surface ocean concentrations of CO₂ following the atmospheric CO₂ increase (Bates et al., 2014). As more carbon dioxide is in the atmosphere, the greater the amount of this gas dissolved in the surface of the oceans.

During interglacial periods the ability of oceans to uptake CO₂ is decreased in relation to the glacial periods because the solubility of CO₂ in warmer waters are lower (Broecker, 1982). Buchanan et al. (2016) point out that the biogeochemical response of the oceans to LGM conditions is linked to increased salinity and decreased temperature, leading to an increase in nutrient concentration (ie

nitrate, phosphate, silica) and total alkalinity, reducing thus the concentrations of atmospheric CO₂. Cold water has low total alkalinity (TA) to TCO₂ ratio that decreases with the degree of carbonate mineral saturation and modifies the carbonate buffer system for further CO₂ uptake or release (Takahashi et al., 2014; Shadwick et al., 2013). Additionally, the solubility of calcium carbonate minerals increases at lower temperatures (Zeebe and Wolf-Gladrow, 2001).

Reconstructions of ion carbonate (CO₃²⁻) in the deep Southern Ocean are consistent with exchanges by biological activity at the surface in a stratified ocean (Yu et al., 2014). Its associated with the inventory of oceanic alkalinity, acts as key to the atmospheric CO₂ modulations in glacial and interglacial timescales. The late Holocene interglacial reconstructions point the decrease of oceanic alkalinity with declined oceanic CO₃²⁻ inventory, so the carbonate compensation contributes to releasing the deep ocean CO₂ during deglaciations (Yu et al., 2016).

The salinity increased of oceans in the ice ages due to sea ice formation and is one of the opposite effects of the temperature changes in CO₂ concentrations. The largest accumulation of fresh water, a decrease in mean sea level, it is possible evaluate that the global ocean in the Last Glacial Maximum (LGM) was about 3% saltier than today (Fairbanks, 1989). Unlike glacial ages, the atmospheric CO₂ is one of the first parameters to be changed, into an interglacial period, almost coinciding with the warming of the Southern high latitudes, which supports the origin of the Southern Hemisphere for the glacial / interglacial CO₂ shift (Sigman and Boyle, 2000).

This study, describes the impact of changes in the CO₂ concentration and orbital changes on the marine biogeochemical cycle in the Last Glacial Maximum and the

interglacial Marine Isotope Stage 11c. The comparisons are based on two sensitivity experiments with orbital forcing, CO_2 , the topography characteristic of the LGM namely ICE6G (Argus et al., 2014; Peltier et al., 2015). These simulations provide an additional perspective on the distribution of marine biogeochemical tracers, on the Southern Ocean.

3.2 Climate model and simulations

The simulations have been conducted with the UVic ESCM version 2.9 (University of Victoria - Earth System Climate Model). The UVic ESCM is a coupled model of intermediate complexity that includes a general 3D oceanic circulation model with 19 levels, coupled to a terrestrial model, a dynamic and thermodynamic sea ice model and a simplified atmospheric model based on energy balance with one level (Weaver et al., 1998). It has 1.8° of latitude and 3.6° of longitude. The biogeochemical module of the UVic ESCM uses predicted TCO_2 , Alkalinity, oxygen and phosphate values following the Ocean Carbon Cycle Model Intercomparison Project (OCMIP) protocol (Orr and Epitalon, 2015). The biogeochemical scheme is a nutrient-phytoplankton-zooplankton-detritus (NPDZ) model (Schmittner et al., 2005; Schartau and Oschlies, 2004).

The marine sediment component has 13 layers where the dissolution of CaCO_3 to sediment assumes an instantaneous sinking of vertically integrated production (Schmittner and Galbraith, 2008). Concentrations and burial rates of sedimentary CaCO_3 are presumed using the particulate inorganic carbon and particulate organic carbon rain ratio (Archer, 1996). Only dissolution of oxic metabolic sedimentary

CaCO₃ is simulated by the sediment scheme and the processes are represented using only oxic model of sediment respiration (Eby et al., 2009).

In order to investigate the marine biogeochemistry of carbon cycle, three sensitive simulations were done. The present-day simulation (PD) was initialized from the pre-industrial background applying the atmospheric CO₂ concentration of the 380ppm and current orbital forcing.

The MIS11c (428-383 ky BP) climate used an atmospheric CO₂ value of 285 ppm and orbital forcing as described in Table 3.1. The LGM (20 ky BP) climate was obtained by setting the orbital parameters for 21 ka BP conditions (Tab. 3.1), atmospheric CO₂ value of 180ppm and the ICE6G ice sheet topography (Argus et al., 2014; Peltier et al., 2015) as anomalies in respect to the PD topography.

The coupled model was integrated for 10.000 years to reached the quasi - equilibrium state and the analysis focus on the last 100 years of the simulation after the model has reached the equilibrium, characterized by stabilization of marine nutrients.

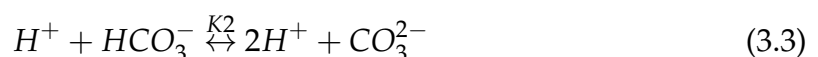
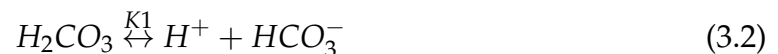
Tabela 3.1: Orbital parameters for LGM, MIS11c and for the control (adapted from (Berger and Loutre, 1991; Loulergue et al., 2008; Coletti et al., 2015a; NOAA, 2018)).

	eccentricity	obliquity	precession	CO ₂
LGM	0.018994	22.949°	114.42°	180ppm
MIS11c	0.01932	23.781°	277.67°	285ppm
PD	0.016724	23.446°	102.94°	380 ppm

3.2.1 Carbonate System

The UVic ESCM marine biogeochemical cycle includes the inorganic carbon model following the protocols of the Ocean Carbon-Cycle Model Intercomparison (OC-MIP; (Orr, 1999)). The output of simulation are concentrations of Phosphate (PO_4^{-3}), Nitrate (NO_3^-), Dissolved Oxygen (O_2), Total Alkalinity (TA), Dissolved Inorganic Carbon (TCO_2), temperature and salinity. Were used to calculate the fugacity concentrations of CO_2 (fCO_2), pH, ion carbonate (CO_3^{2-}) and bicarbonate (HCO_3^-) and solubility of calcite (Ω) (Lewis and Wallace, 1998).

The CO2SYS is the first publicly and widely accepted available software package for calculation parameters of the marine carbonate system. Currently other similar software package for carbonate system calculation are available and the comparison of these another packages has essentially the same results (Orr and Epitalon, 2015). The chemical equilibrium of CO2SYS for the carbonate system can be described by the following equation:



K_1 and K_2 are the first and second equilibrium constant of the carbonate system respectively and are given as empirical functions of temperature and salinity taken

from (Dickson, A.G., Sabine, C.L. and Christian, 2007):

$$K_1 = \frac{[HCO_3] + [H^+]}{[CO_2]} \quad (3.4)$$

$$K_2 = \frac{[CO_3^{2-}] + [H^+]}{[HCO_3]} \quad (3.5)$$

The carbonate ion concentration as a function of TCO₂ is shown in equation 3.6:

$$[CO_3^{2-}] = \frac{[TCO_2] + [K_1K_2]}{[H^+]^2[H^+]K_2 + K_1K_2} \quad (3.6)$$

In CO2SYS, *f*CO₂ is calculated from the input of TCO₂-pH according to the following equation:

$$fCO_2 = TCO_2x \frac{[H^+]^2}{[H^+]^2 + K_1x[H^+]K_1K_2/K_0} \quad (3.7)$$

Ideally, after air and water equilibrium, the CO₂ in gas phase will go up and down due to any changes in the concentration of dissolved CO₂ (H₂CO₃⁻) knowing as Henry's Law, described bellow;

$$K_h = \frac{pCO_2}{CO_2} \quad (3.8)$$

where *K_h* is the equilibrium constant that depends on temperature and salinity.

The solubility product of calcite needs to be calculated. The solubility product *K_sp* defines the concentration of [CO₃²⁻ and [Ca₂₊] in thermodynamic equilibrium with solid calcite and can be outlined by the following equation

$$K_{sp} = [Ca^{2+}] + [CO_3^{2-}] \quad (3.9)$$

where K_0 is the solubility coefficient of CO₂ in seawater.

Oceanic [Ca²⁺] variations are quite small and closely proportional variations in salinity. The relation between salinity and [Ca²⁺] has been taken from (Mucci, 1983). To calculate the saturation state of calcium carbonate (Ω), that is the function of carbonate ion concentration. The CaCO₃ saturation state of seawater Ω can be expressed as:

$$\Omega = \frac{[Ca^{2+}] + [CO_3^{2-}]}{K_{sp}} \quad (3.10)$$

Where K_{sp} is the solubility product constant for the specific CaCO₃ mineral and depends on salinity, temperature, and pressure. When $\Omega < 1$ represents undersaturation where dissolution is more favorable and $\Omega > 1$ are supersaturation and benefit the precipitation.

3.2.2 Model, LGM and MIS11c Climate Validation

A spatial pattern of UVic ESCM control simulation with corresponding observations of GLODAP_v2, using Taylor diagrams (Taylor, 2001). As shown in Fig 3.1, the data were analyzed separately between the global, SH, NH and the tropics. For the global and SH mean, the correlation coefficients range between 0.78 (PO₄³⁻) and 0.99 (SST) with normalized standardized deviation close to 1. However, simulated spatial pattern for the NH and the Tropical regions slightly deviations from observation and lower correlation for NO₃⁻ (r<0.4) and PO₄³⁻ (r<0.5). In short, UVic

ESCM reproduces reasonably well the large-scale features of physical and marine biogeochemical fields.

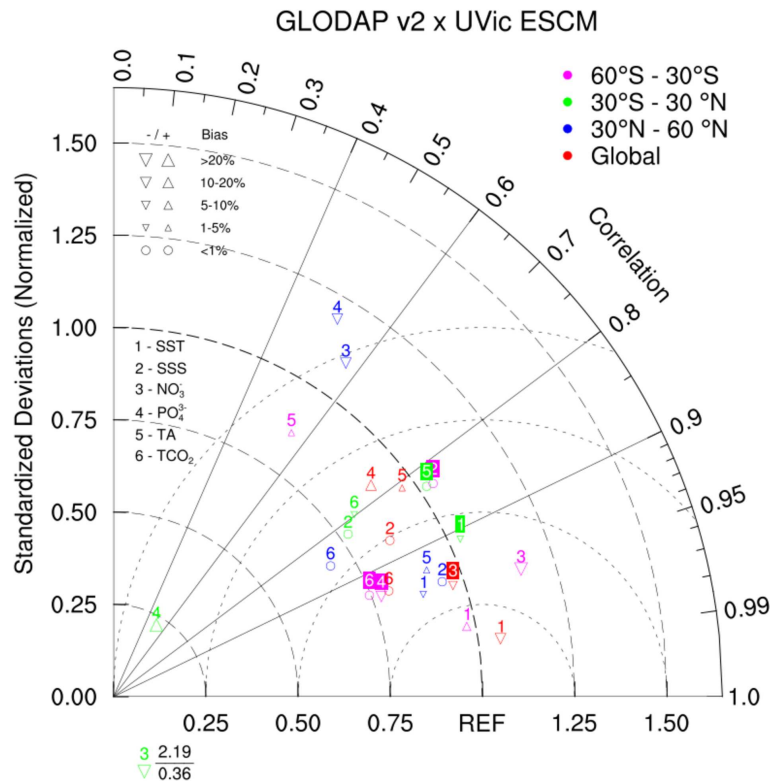


Figura 3.1: Taylor diagram comparing statistic pattern of annual mean fields between UVic ESCM simulation control and corresponding GLODAP_v2 observations, including surface temperature, salinity, nitrate, phosphate, total alkalinity and TCO₂. All fields are normalized by the standard deviation of corresponding observations. Indeed, observation fields have a standard deviation of one, which is represented by REF (x label). The distance between the model points and the reference point indicate the quadratic -root-mean-square (QRMS) difference between model simulation and observations.

The LGM ice sheets based on ICE6G topography (Argus et al., 2014; Peltier et al., 2015) is approximately higher by about 3000 meters than today in North America, Scandinavia and Eastern Siberia (Figure 3.2a). Leading to a surface temperature anomalies like -24°C over North America compared to present day conditions (3.2 b). In Antarctica the changes are concentrated in the Weddell sea, Antarctica Peninsula and West Antarctic ice sheets that is approximately 1000 m higher than today. Those changes in southern ice sheets are generally controlled by variations

of global sea level and endorse the assumption that the ice sheets of Antarctic continent follow oceanic teleconnections due to variations in the Northern Hemisphere (Huybrechts, 2002).

Changes in topography lead to sea level air temperature anomalies over North America by about -24°C , in the LGM simulation as compared to present day conditions and differences over the Fennoscandian ice sheet by about -18°C (Fig. 3.2b). Lower SSTs as compared to the PD are evident in the Nordic Sea region and western north Pacific (Fig. 3.2 b) in consonance with the wind intensification.

In comparison with reconstructions of Southern Ocean sea surface temperature, our LGM climate is 0.34 warmer than that delivered by the Multiproxy Approach for the Reconstruction of the Glacial Ocean Surface (MARGO, (Annan and Hargreaves, 2013)). By comparing to the CMIP3 ensemble (Schmitt, 2011), the differences show that our LGM simulation is 1.1°C colder than the CMIP3. Discrepancies between the simulated LGM and paleo-reconstructions may reflect the high variability of SST and the limited available number of samples.

In order to validate the results of MIS11c simulation, our results are compared with the outcomes of Melles et al. (2012) and Coletti et al. (2015a). They calculated the insolation at the top of the atmosphere (TOA) for the hottest month of summer (July) and the temperature at the location of Lake El'gygytgyn (172°E and 67.3°N).

The table (3.3) a good agreement is observed in the values presented by the UVic simulation of MIS11c and those values proposed by Melles et al. (2012) and Coletti et al. (2015a). The orbital configuration of MIS11c is characterized by the minima eccentricity (Table. 3.3) producing a high-intensity summer insolation, with more

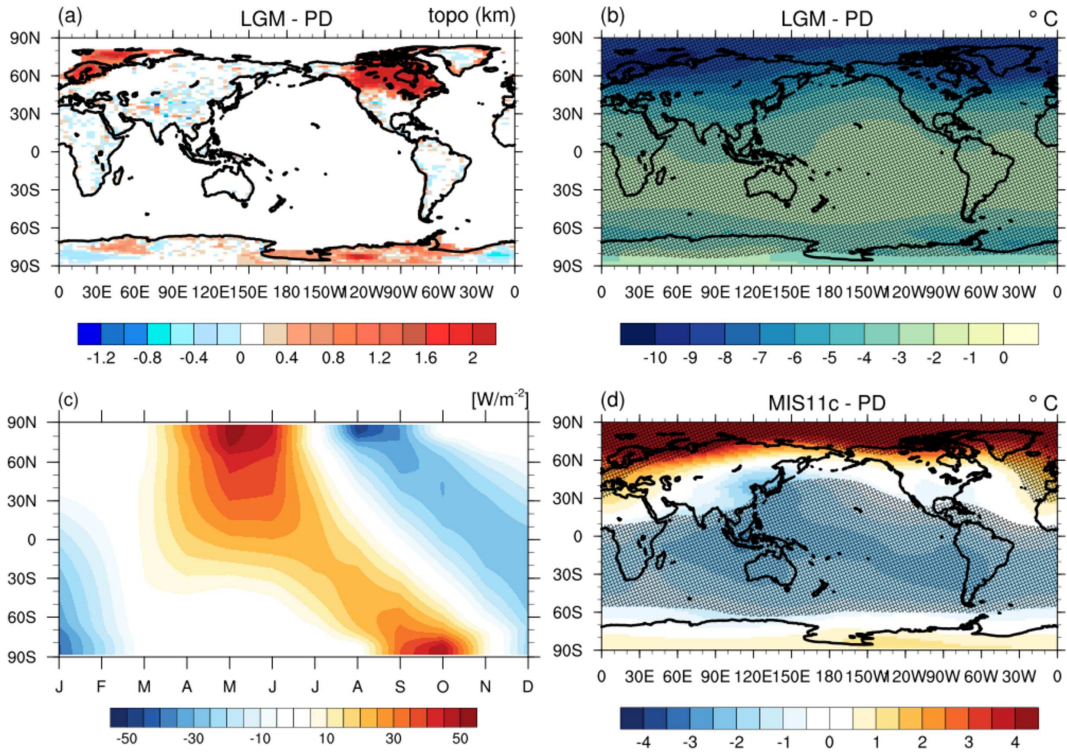


Figura 3.2: (a) Topography differences between LGM and PD simulations (km), Sea level temperature anomalies ($^{\circ}\text{C}$) between (b) LGM and PD, (d) MIS11c and PD. (c) Monthly insolation anomalies simulation at the top of the atmosphere for interglacial MIS11c (Wm^{-2}) with respect to the current orbit.

than 50 Wm^2 with respect to today (Melles et al., 2012; Coletti et al., 2015b). The model experiments show that the insolation anomalies, differing in the Northern and Southern Hemisphere compared to PD (3.2c). In the NH summer from + 35 to 50 Wm^2 and 20 to + 40 Wm^2 in the SH summer.

Tabela 3.2: Anomalies sea surface temperature from LGM-PD from the reconstructions for the Southern Ocean comparative.

Dataset	SST Anomalies ($^{\circ}\text{C}$)
UVic	-2.23
MARGO (Annan and Hargreaves, 2013)	-2.57
CMPI 3 (Schmittner et al., 2011)	-3.42

The MIS11c warm climate possible lead to a reduction in the West Antarctic ice

sheet and Greenland and may potentially contribute to increase sea levels up to 11 meters with respect to today (Raymo and Mitrovica, 2012). The Arctic also decreases the sea ice amount and increases heat flux, allowing the intrusion of warmer water into the Arctic basin from the North Pacific. (Cronin et al., 2013).

Tabela 3.3: Comparative for PD and MIS11c insolation at the top of atmosphere between UVic simulation and Coletti et al. (2015a). The analyses were done for the point referring to the Lake El'gygytgyn for the month of greatest insolation especially July, for surface temperature and TOA.

	PD		MIS11c - PD	
	TOA Wm ²	SAT (°C)	TOA Wm ²	SAT (°C)
UVic	439	10.05	+40 - 55	+0.45
Coletti et al. (2015a)	445	10.3	+45 - 55	+0.5

3.3 LGM and MIS11c climate state

In presenting our results, we focus on the difference between the LGM and MIS11c. So, first we show the simulated physical changes in the ocean and sea ice and then present how the ocean biogeochemical fields differ between those climate changes. Afterwards, we present some differences between LGM and MIS11c climate on the Weddell Sea.

The UVic ESCM uses prescribed present day winds, it includes wind feedback that has an empirical relationship, between the temperature and density of the atmospheric surface. Any perturbation in the present climate, leads the model to calculate the affected air temperature and consequently anomalies in the surface pressure. From those calculations anomalies of wind stress are added in the specific mean fields of each coupling scheme of the model (Weaver et al., 1998). Indeed,

anomalies between the LGM and MIS11c wind speeds, show positive anomalies of 0.2 m/s in the Southern Ocean and 1 m/s in the Antarctic continent (not shown). The wind increase in the LGM with respect to the MIS11c can be attributed to the larger sea ice thickness, as well to increase ice sea cover in Antarctic (Fig. 3.2 d), as suggested by [Banderas et al. \(2012\)](#) and [Chavaillaz et al. \(2013\)](#).

The mean sea ice thickness simulated for both LGM and MIS11c are present in the figure 3.3. Associated with the lower sea surface temperatures (Fig. 3.4) the coverage is larger in the LGM compared to the MIS11c as expected. However, over the Antarctic coast around the West Antarctic ice sheet, the ice thickness is higher in the MIS11c. The seasonal sea ice cycle for LGM (not shown) presented the largest sea-ice thicknesses between September and October, and for MIS11c between August and September. The maximum sea ice extent for the LGM reaches 42 °S in the Atlantic and Indian basin, and 50 °S in the Pacific basin. For MIS11c, it goes to 55 °S in the Atlantic basin and 60 °S in the Pacific basin. Similar results are found by [Buchanan et al. \(2016\)](#).

The anomalies in the Weddell Sea (Fig. 3.3c) shown values about 1.5 m higher for LGM simulations. The Figure 3.3 shown a large amount of sea ice production in the LGM on the East Antarctic coastal compared with MIS11c simulation being in agreement with [Kusahara et al. \(2015\)](#); [Kobayashi et al. \(2015\)](#), they simulations showed that the role of deep water formation during the LGM was in the East Antarctica bordering maximum ice extent.

The MIS11c climate in our simulation is characterized by mean surface temperature of the Southern Ocean (below 40 °S) by about 5.7 °C and the LGM 3.6 °C (table 3.4).

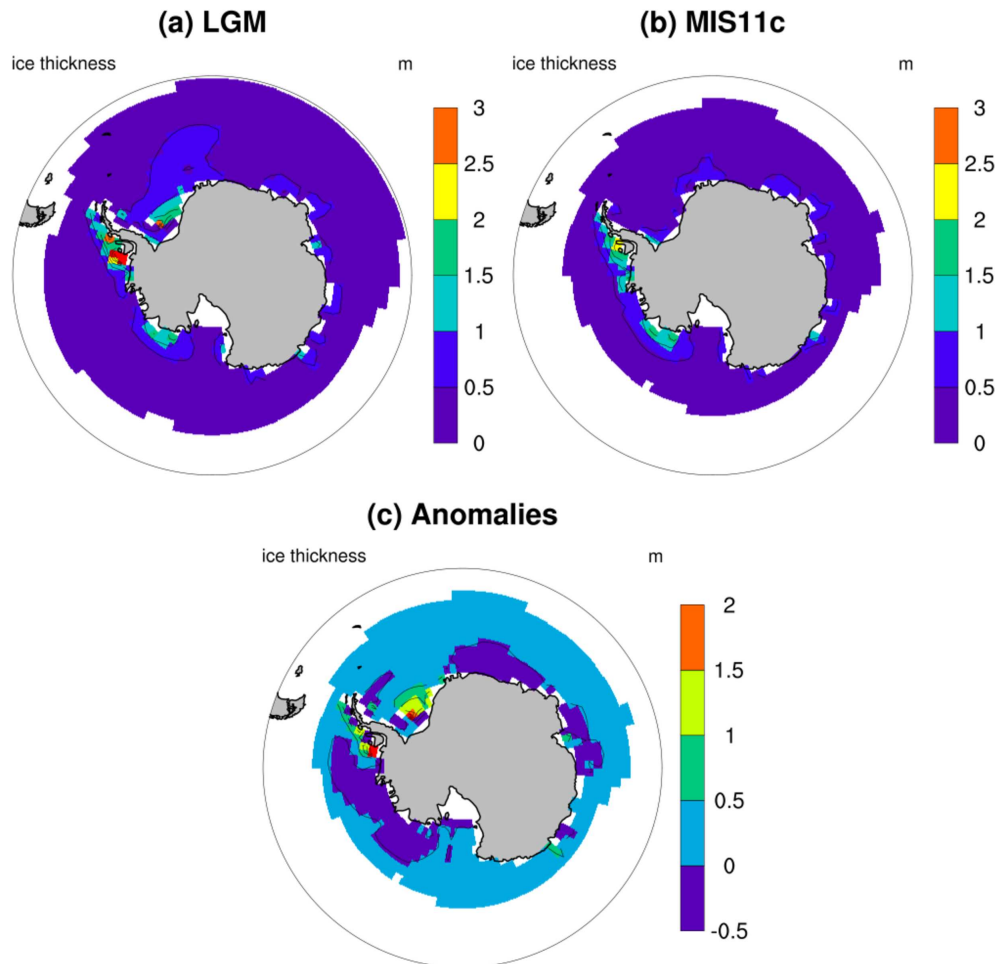


Figura 3.3: Ice thickness for (a) LGM,(b) MIS11c, (c) anomalies. Note the nonlinear bar label axes.

As expected, a latitudinal thermal gradient toward to the lower latitudes. Thus, extremely intensified in the LGM. Based on the thermal wind assumption a strengthening of wind stress might be expected by modifying the heat flux exchange between the atmosphere and ocean. The meridional mean temperature (Fig. 3.4d,e,f) shows that most of the Southern Ocean is colder in the LGM than MIS11c. It can be demonstrated that most of the Southern Ocean below 2000m is dominated by Antarctic Bottom Water (AABW) as part of the overturning lower cell. In the deep ocean, the temperature in the LGM is between 0 °C to -4 °C, whereas in the MIS11c temperatures range from 5 °C to -2 °C. The anomalies show its lowest value in the region

Tabela 3.4: Surface mean values for Southern Ocean of physical and biogeochemical parameters calculated with UVic ESCM and CO2SYS for control, MIS11c and LGM.

Variable	PD	MIS11c	LGM
SST (°C)	5.8	5.7	3.6
SSS	34.6	34.52	35.01
TA ($\mu\text{mol}/\text{kg}$)	2223.4	2236	2367.65
TCO ₂ ($\mu\text{mol}/\text{kg}$)	2123.2	2120	2091
PO ₄ ³⁻ ($\mu\text{mol}/\text{kg}$)	1.23	1.26	1.32
NO ₃ ⁻ ($\mu\text{mol}/\text{kg}$)	16.36	16.78	15.58
O ₂ ($\mu\text{mol}/\text{kg}$)	309.9	305.4	314.7
<i>f</i> CO ₂ (uatm)	345	290.8	188.81
HCO ₃ ²⁻ ($\mu\text{mol}/\text{kg}$)	1788.39	1848.2	1772.21
CO ₃ ⁻ ($\mu\text{mol}/\text{kg}$)	223.61	197.65	239.85
pH	8.16	8.14	8.45
Ω calcite	7.21	4.73	5.73
Ω aragonite	7.21	3.02	3.68

55 ° C which extends to approximately 800m (-3 °C).

The salinity in the Southern Ocean has an average of 34.5 for the MIS11c and 35 for the LGM (table 3.4). The East Antarctic region presents the largest anomalies, that are higher than 0.3 (Fig. 3.5 c). This high salinity in the LGM is related to the increase of brine rejection associated with more prone conditions for the sea ice formation. The large amount of sea ice is formed in the vicinity of East Antarctica (Fig. 3.3) and [Kusahara and Hasumi \(2013\)](#) suggests that deep water formation may be occurred there in the LGM, as found in our study.

The comparison between the LGM and MIS11c simulations, show positive anomalies along the vertical ocean column (Fig. 3.5f), implying that the salinity stratification was weakened in the deep Southern Ocean in the LGM, because larger ano-

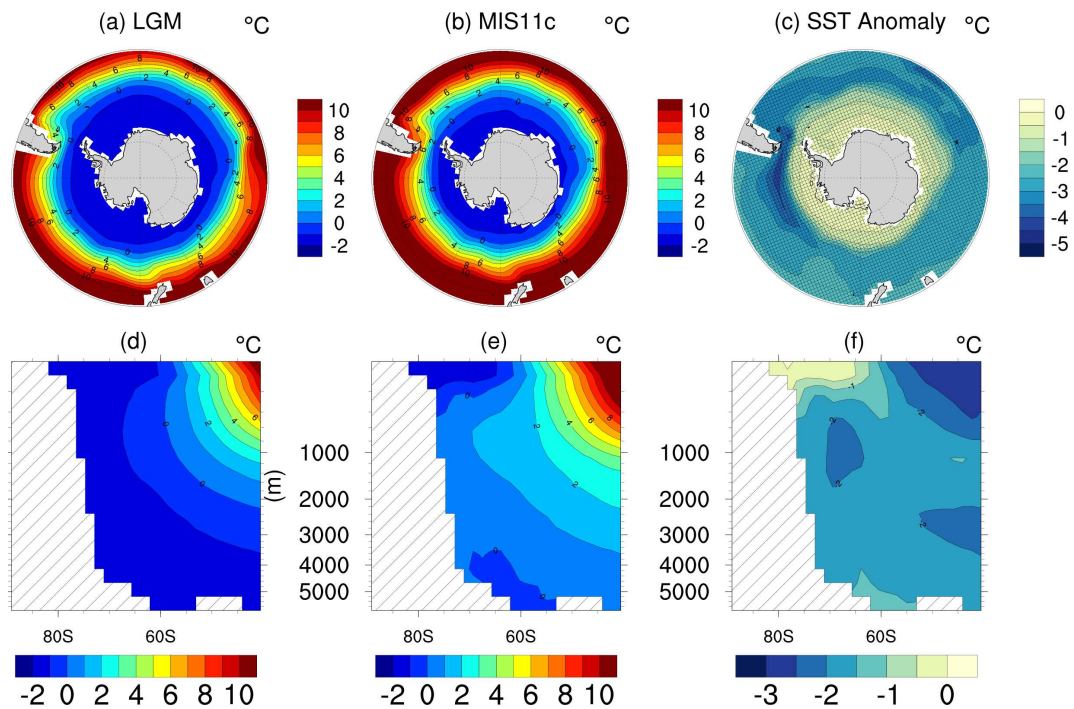


Figura 3.4: Temperature in °C for the surface (a) LGM,(b) MIS11c, (c) anomalies and averaged meridional crosscut for (d) LGM, (e) MIS11c and (f) anomalies. Note the nonlinear vertical axes, used to zoom in on the upper ocean layers. Hachured areas are statistically significant at the 95% level.

malies are evident in the upper levels. This enhanced convection in the Southern Ocean is claimed to be one cause for more oceanic carbon during the LGM with respect to the interglacial ages (Toggweiler, 1999). Less saline region between 1500m and 2000m may indicate the presence of Antarctic intermediate water (AAIW).

Changes in surface ocean features during the MIS11c and LGM affected the meridional overturning circulation. Reconstructions of the past climate have shown that both climates and the AMOC have changed in the past.

The AMOC pattern (Fig. 3.6) shows a weakening of AMOC in the LGM (Fig. 3.6a) the upper cell well remains as North Atlantic Deep Water (NADW) is shallower as compared to its counterpart in the MIS11c. The maximum NADW is also weaker in the LGM than in MIS11c by almost 10 Sv (Fig. 3.6b). We can observe a considerable subduction and northward flow of the LGM intermediate water

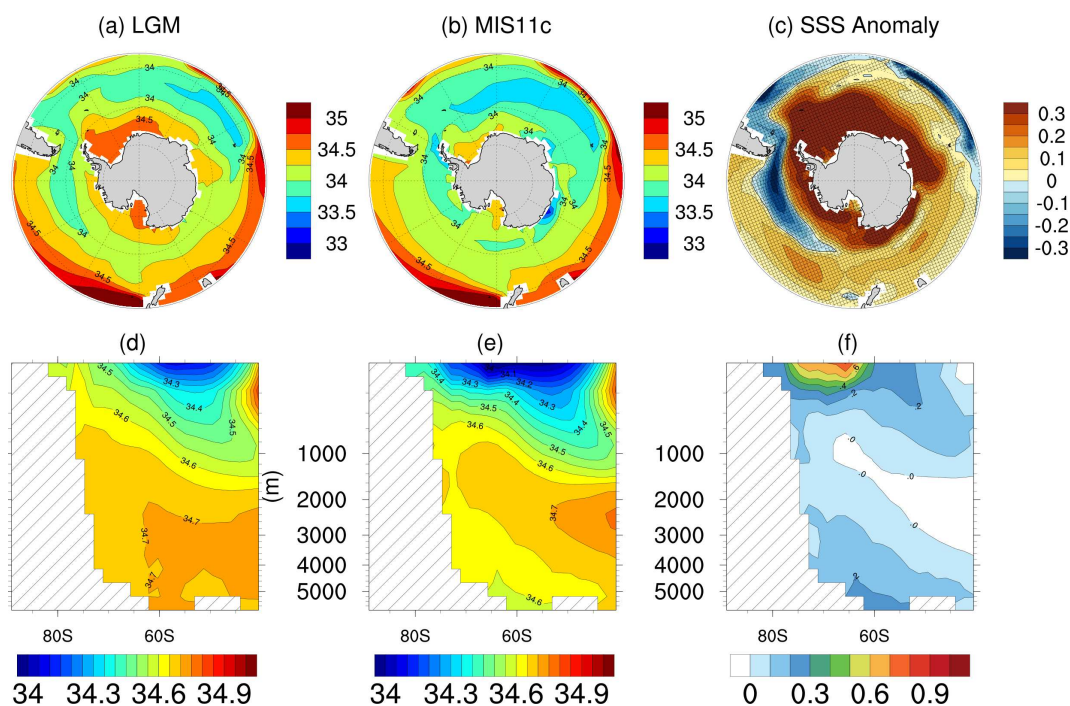


Figura 3.5: Same as Fig. 3.4 for Salinity . Note the nonlinear vertical axes, used to zoom in on the upper ocean layers. Hatched areas are statistically significant at the 95% level.

between 2000 and 3000 meters. Our results are consistent with proxy data from LGM, that suggested a shallower NADW and an AABW reaching farther in the NH (Duplessy et al., 1988; Lippold et al., 2012; Ferrari et al., 2014; Lippold et al., 2016).

The LGM temperatures are lower up to approximately 50 °S between two scenarios in the (Fig. 3.4 c). Temperature anomalies (close to 0 °C) bordering Antarctica are related to the ice cover that in both runs (MIS11c and LGM) hamper the drop in SSTs (Fig. 3.3). However, the lowest temperature anomalies are found in the area corresponding to the Antarctic Polar Front (APF) (Orsi et al., 1995) with values by about -4 °C.

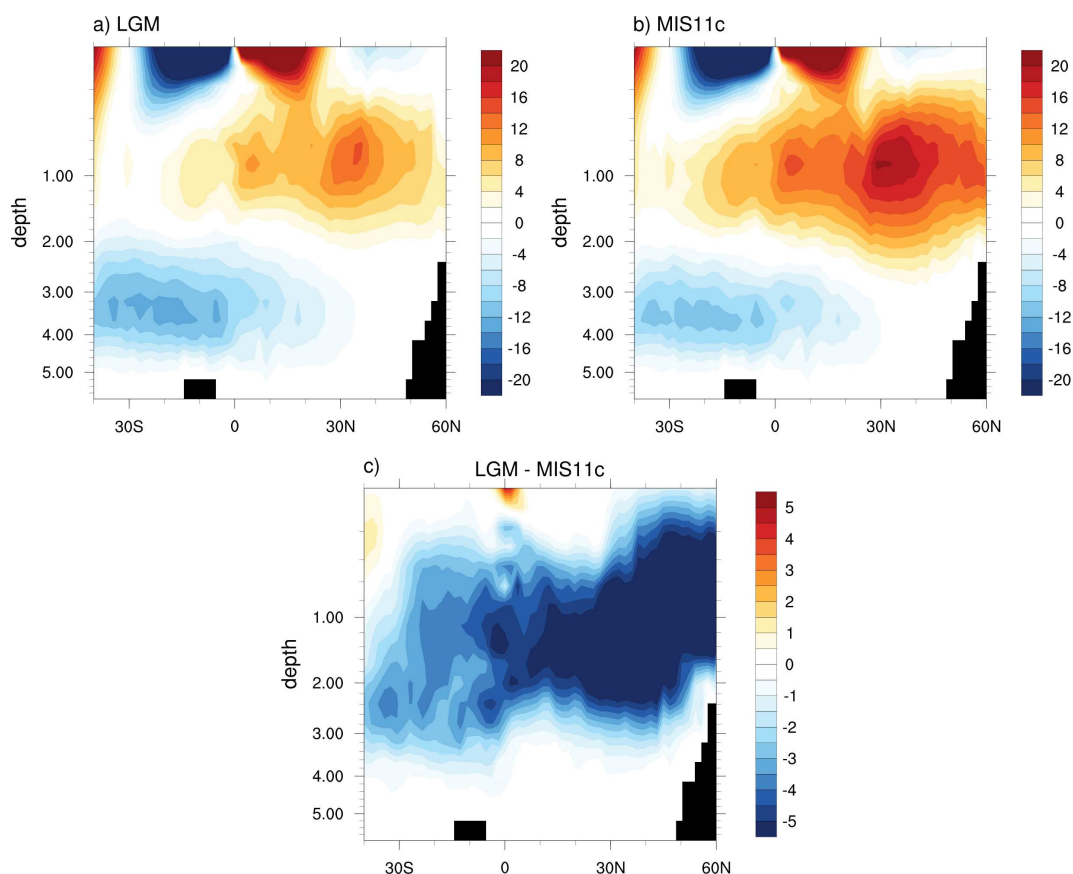


Figura 3.6: Atlantic Meridional Overturning in Sv for: a) LGM, b) MIS11c and c) LGM - MIS11c.

3.3.1 fCO_2 exchange processes

It may be argued that those climate changes discussed above might have an important impact on the oceanic biogeochemistry in the Southern Ocean in the LGM and in the interglacial periods, the MIS11c. The global mean values of the ocean surface CO_2 fugacity (fCO_2) for the LGM simulation is 188.1 ppm and for the MIS11c simulation 290.2 ppm (table. 3.4). The areas of highest concentration of fCO_2 are associated with the release of CO_2 to the atmosphere while oceanic CO_2 uptake are associated with the low concentration regions of fCO_2 (if $fCO_{2ocean} < fCO_{2atm}$).

The values were calculated according to the equation 3.7. As expected, maxima values for both LGM and MIS11c simulation of the fCO_2 found in the Equator and

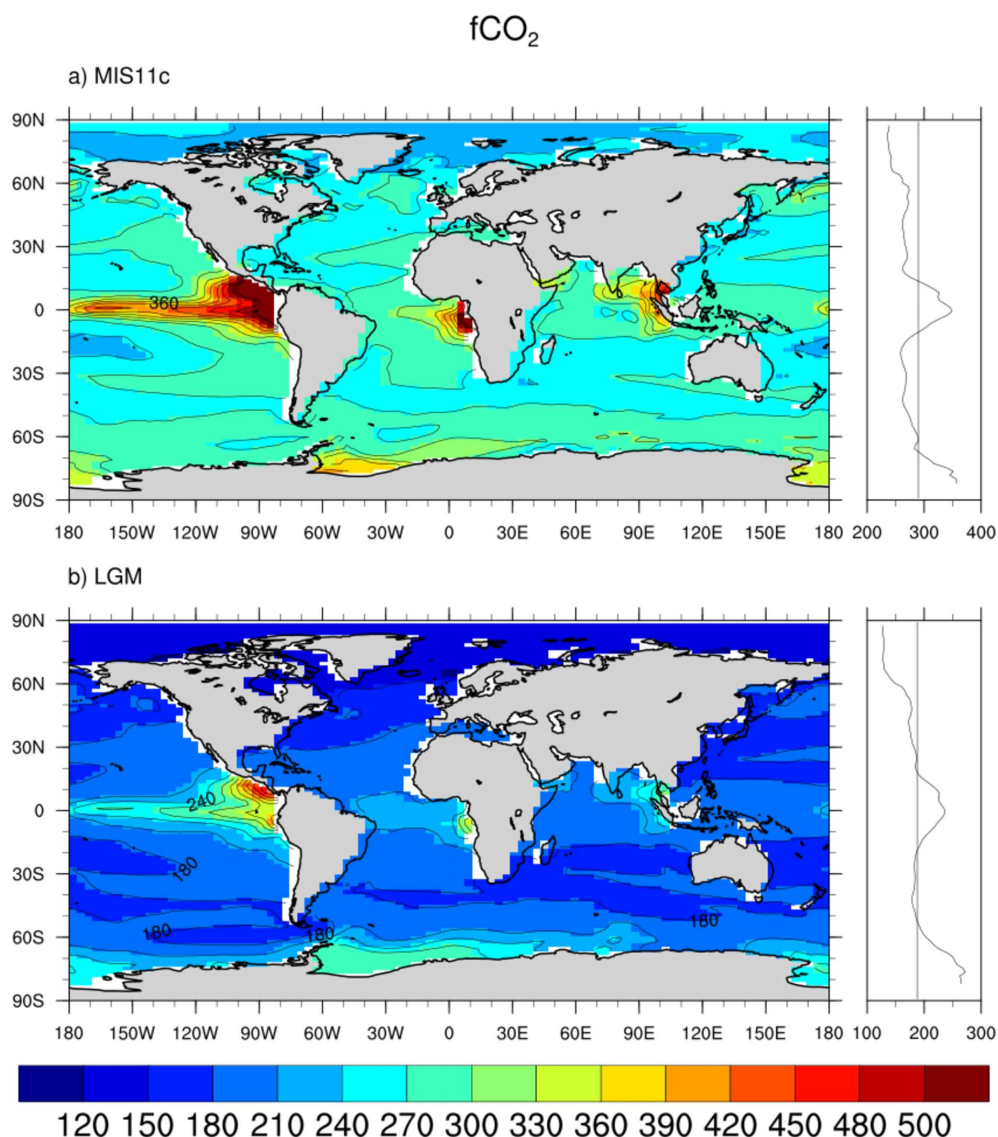


Figura 3.7: Annual mean surface ocean $p\text{CO}_2$ (ppm) calculated by CO2SYS for (a)MIS11c and b) LGM.

in the eastern boundary currents along the Pacific cold tongue, the guinea Gulf in Africa and in the northern Indian Ocean (Fig. 3.7) similar findings have been reported by Kubota et al. (2014). In addition to SST and SSS, changes of TCO_2 can also contribute to the decrease of glacial $f\text{CO}_2$, so the efficiency of ocean solubility pump would act to increase the ocean's uptake of atmospheric CO_2 during the LGM. In the MIS11c simulation the increase of $f\text{CO}_2$ is driven by higher SST and low SSS, however in the equatorial and coastal regions the upwelled nutrient-rich

waters plays a significant role.

The low concentrations found in the Southern Ocean (with the exception of Weddell Sea), especially near the Drake Passage, which corresponds to low salinity (Fig. 3.5) and low alkalinity (Fig. 3.11) for the MIS11c simulation. Despite of, the Southern Ocean is characterized by values of $f\text{CO}_2$ below or equal to the mean concentrations for both LGM and MIS11c simulations, consistent with deep water formation. In the NH another low-concentration zone of $f\text{CO}_2$ is located above 50 °N in Atlantic and the Pacific basin for both simulations, since the Arctic Ocean acts as CO_2 sink.

3.3.2 Biological production

The decrease of SST in the LGM relative to MIS11c simulation results in reduced O_2 concentration in the Austral polar waters (Fig. 3.8). The average of O_2 in the LGM simulation is $261.25 \mu\text{mol/kg}$ and $253.52 \mu\text{mol/kg}$ in the MIS11c run. The lower ventilation and the increase of primary productivity (Lu et al., 2016) over interglacial enhances the water column stratification in glacial periods. Differences between LGM and MIS11c shows of O_2 negative anomalies on the surface (between 75 °S and 60 °S), with an increase in 1000 m - 2000 m possibly related to the increase subduction of AABW. Increased respiratory CO_2 in the glacial deep sea is consistent with reduced dissolved O_2 concentrations in the glacial deep Southern Ocean (Fig. 3.8f). It also agrees with inferences of increased biological efficiency and enhanced efficiency stratification in the glacial ocean (Yu et al., 2014).

Concentrations of NO_3^- and PO_4^{3-} on the surface of the Southern Ocean (Fig. 3.10, 3.9) are similar for both simulations. The Southern Ocean surface mean (Ta-

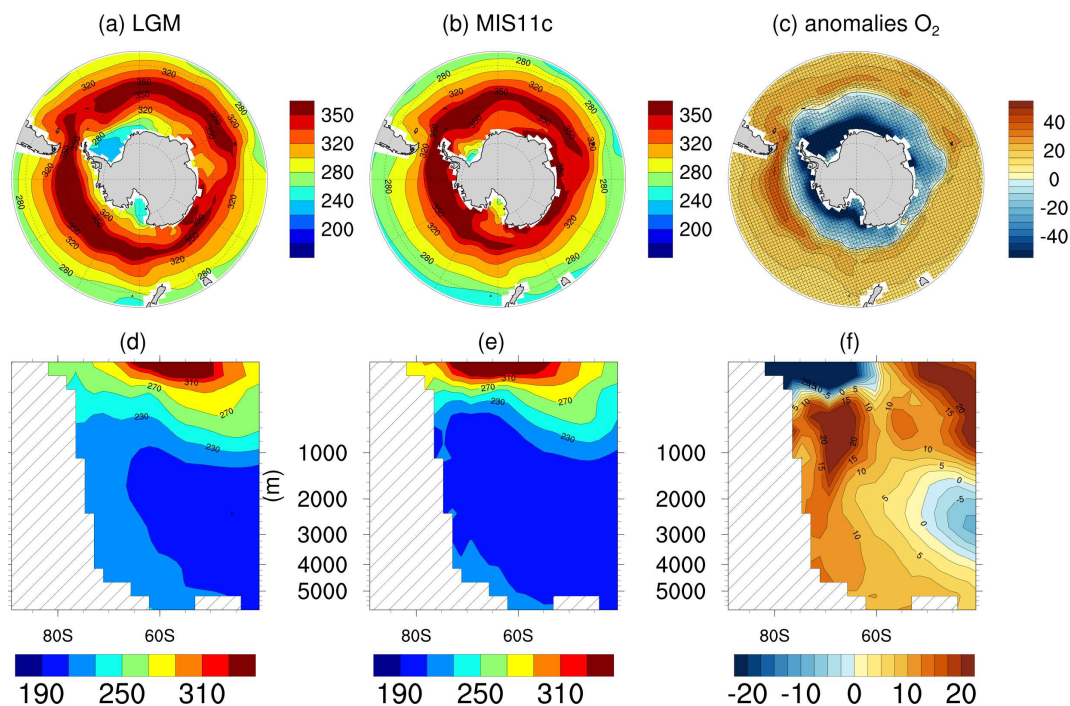


Figure 3.8: O₂ in $\mu\text{mol}/\text{kg}$ for the surface (a) LGM, (b) MIS11c, (c) anomalies and averaged meridional crosscut for (d) LGM, (e) MIS11c and (f) anomalies. Note the nonlinear vertical axes, used to zoom in on the upper ocean layers.

ble 3.4) for nitrate are 4.41 (5.22) for LGM (MIS11c) and for phosphate 0.68 (0.65) $\mu\text{mol}/\text{kg}$ for LGM (MIS11c). Interestingly, concentrations are higher for LGM than for MIS11c in the Weddell Sea. High latitudes, especially in the Southern Ocean, have a maximum of nutrients. In intermediate deep ocean, noted that negative anomalies are found for NO_3^- .

Vertically analyzed, the PO_4^{3-} is well marked (Fig. 3.10). In the first 1000 meters the concentrations are lower, but below 1000m there is an increase of concentrations in the LGM (Fig. 3.10f). The anomalies pattern shows a dipole character, in which the LGM shows lower (high) PO_4^{3-} concentration in the western (eastern) hemisphere with respect to the MIS11c. It has to be mentioned that the PO_4^{3-} anomalies match nicely with SSS pattern (Fig. 3.5).

The increase in PO_4^{3-} concentrations in the LGM simulations of Southern Ocean,

fits with the increase of the subduction PO_4^{3-} rich AABW water transferring the phosphate to the abyssal zones and consequently reducing the concentrations in upper ocean. Analyzes of $\delta^{13}\text{C}$ of Southern Ocean indicate a high concentration of nutrients (ie. NO_3^- , PO_4^{3-} and Si) above 1500 - 2000 m depth during the LGM (Marchitto and Broecker, 2006; Tagliabue et al., 2009). These results are consistent with our simulations (Fig. 3.9f and 3.10f).

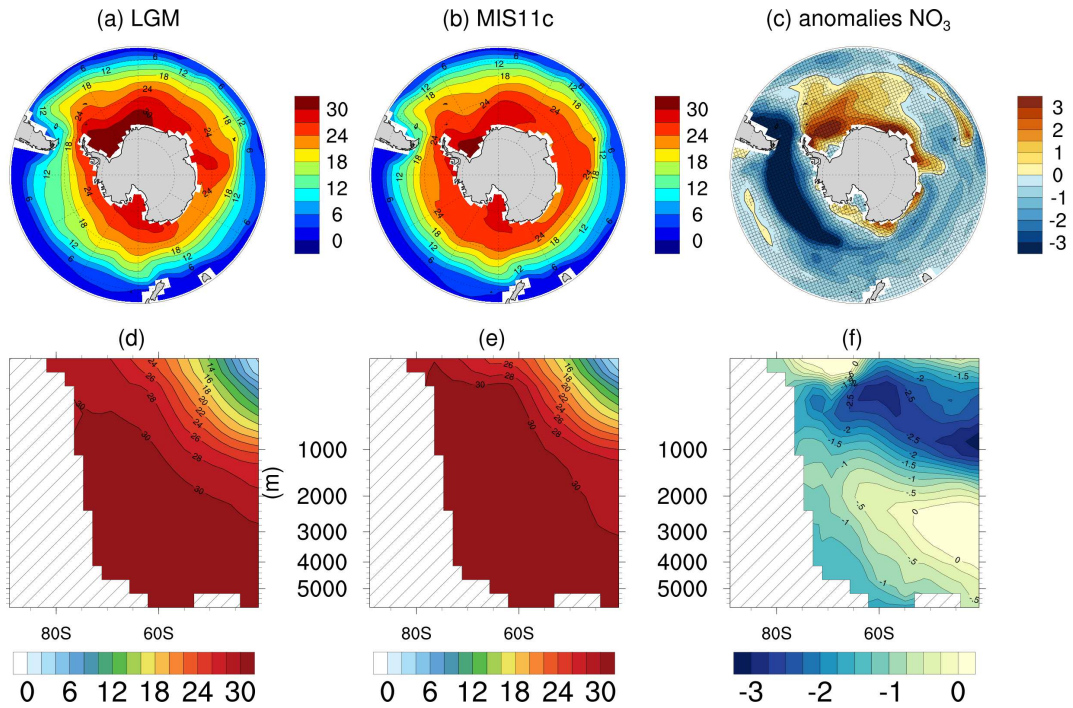


Figura 3.9: NO_3^- in $\mu\text{mol/kg}$ for the surface (a) LGM, (b) MIS11c, (c) anomalies and averaged meridional crosscut for (d) LGM, (e) MIS11c and (f) anomalies. Note the nonlinear vertical axes, used to zoom in on the upper ocean layers.

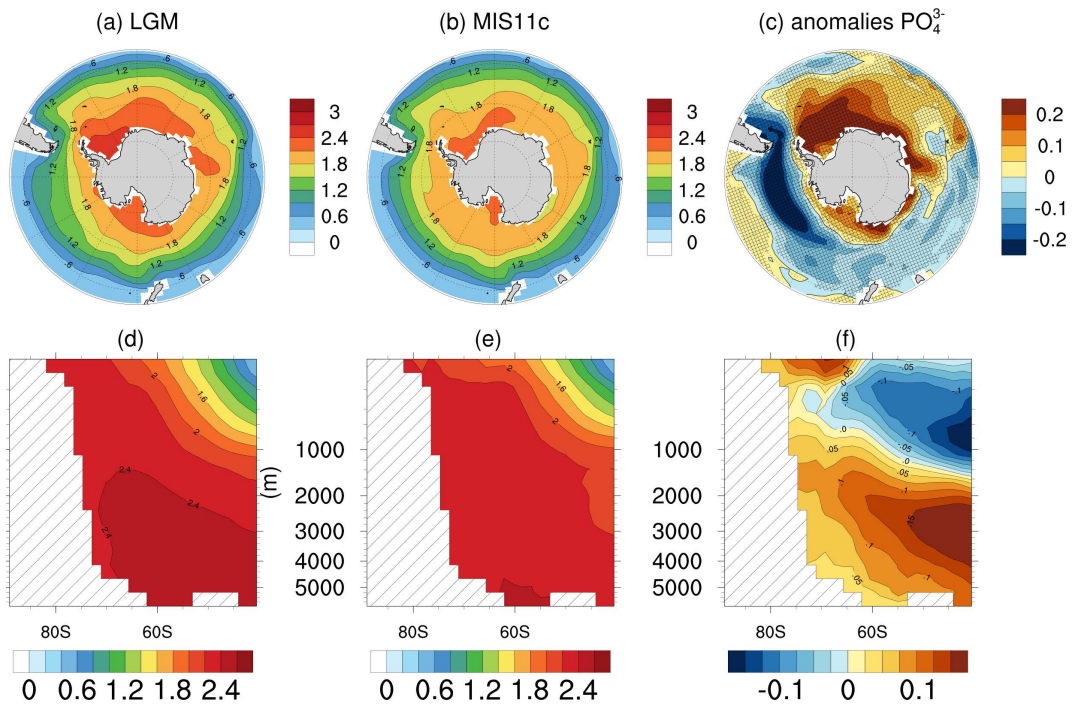


Figura 3.10: PO_4^{3-} in $\mu\text{mol/kg}$ for the surface (a) LGM, (b) MIS11c, (c) anomalies and averaged meridional crosscut for (d) LGM, (e) MIS11c and (f) anomalies. Note the nonlinear vertical axes, used to zoom in on the upper ocean layers.

3.3.3 Carbonate Chemistry

The distribution of TA concentrations in the Southern Ocean for LGM and MIS11c are shown in figure 3.11 and 3.12. The spatial pattern of surface ocean TA and TCO_2 are similar in the two simulations, the differences are in their concentrations. While TA in the LGM (Fig. 3.11c) are much higher than MIS11c, TCO_2 concentrations are slightly lower than MIS11c throughout the region, with the exception of Weddell Sea, where positive anomalies up to $40 \mu\text{mol}/\text{kg}$ are found. Differently, concentrations of TCO_2 in the LGM (Fig. 3.12c) are lower in the Southern Ocean compared to MIS11c, in exception of the Weddell Sea. The surface average (table. 3.4) of Southern Ocean for TA (TCO_2) is 2367.65 (1988.03) $\mu\text{mol}/\text{kg}$ and 2345.04 (2018.68) $\mu\text{mol}/\text{kg}$ for LGM and MIS11c, respectively.

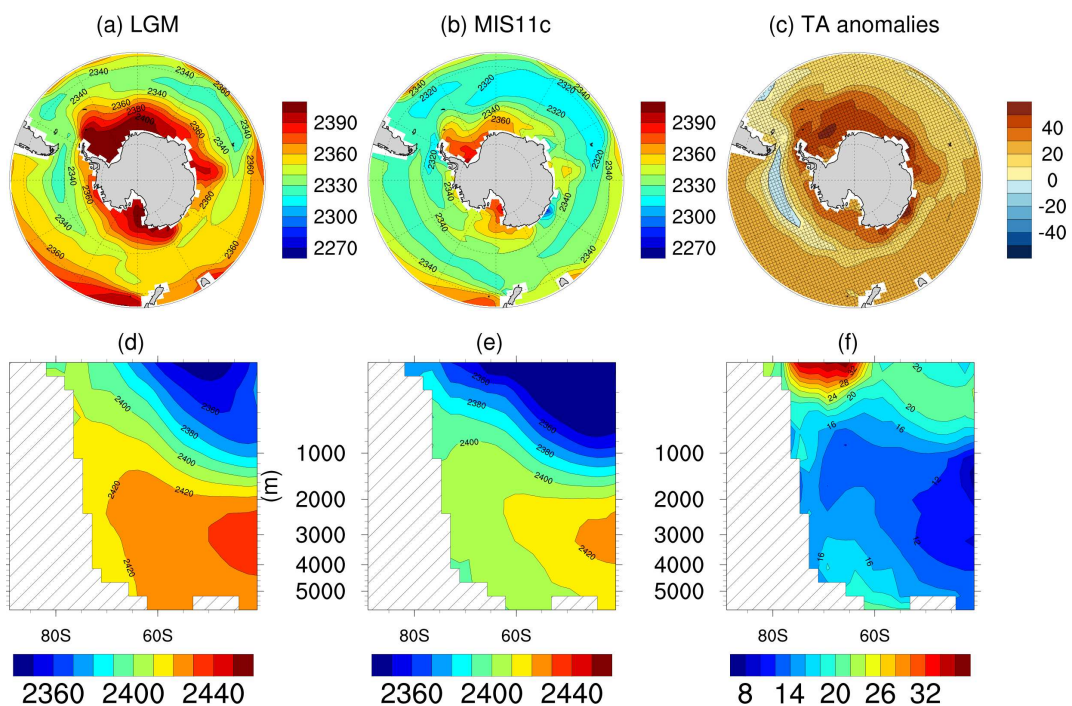


Figure 3.11: TA in $\mu\text{mol}/\text{kg}$ for the surface (a) LGM, (b) MIS11c, (c) anomalies and averaged meridional crosscut for (d) LGM, (e) MIS11c and (f) anomalies. Note the nonlinear vertical axes, used to zoom in on the upper ocean layers.

The surface concentrations of TCO_2 are driven mainly by temperature (Fig. 3.4),

whereas TA concentrations are primarily a reflection of salinity (Fig. 3.5, as can be seen for both simulations. The low salinity in the $\approx 55^\circ\text{S}$ latitudinal belt, induced by sea ice melting formation leads to a decrease of TA concentrations in the MIS11c in respect to the the LGM simulation. It should be emphasized that the MIS11c values is smaller than those delivered by the LGM simulation in the whole water column.

Turning to TCO_2 evaluation, high temperatures, low TA and low CO_2 uptake in the MIS11c, generally results in high concentrations of TCO_2 for the entire basin as compared to the LGM (Fig. 3.19). The opposite occurs in the LGM simulations (Fig. 3.12f), where the low temperatures raise the TA concentrations, however, the TCO_2 decrease in the entire water column in the Southern Ocean. This decoupling may be due to decreased biological productivity with less transport of organic carbon from the surface down into the ocean, or perhaps by the decrease of CO_2 concentration of the surface in general. The reduced CO_2 concentrations between interglacial (285 ppm) to glacial (185 ppm) implies in a forced balance of the oceans surface, which consequently reduces the TCO_2 concentrations (Matear et al., 2015).

The differences between TA and TCO_2 concentrations especially in intermediate waters of the Southern Ocean are related to remineralization of organic matter. The maximum concentration of TA occurs deeper than that for TCO_2 due to the higher influence of the biological pump on the remineralization of organic carbon, because TA is more influenced by the dissolution of the CaCO_3 particles in the water column (Chung et al., 2003).

Since the concentrations of Ca^{2+} in the oceans are nearly uniform, the solubility of CaCO_3 is often described in terms of CO_3^{2-} concentrations. The calcium car-

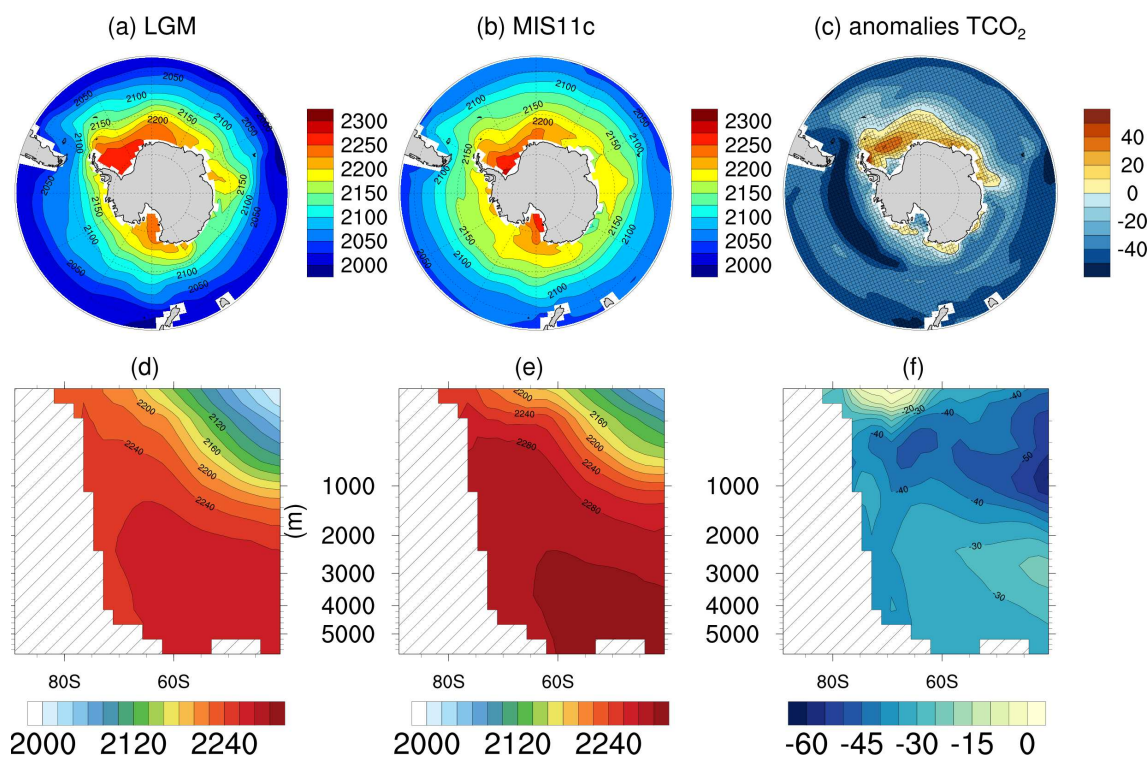


Figura 3.12: TCO₂ in $\mu\text{mol}/\text{kg}$ for the surface (a) LGM,(b) MIS11c, (c) anomalies and averaged meridional crosscut for (d) LGM, (e) MIS11c and (f) anomalies. Note the nonlinear vertical axes, used to zoom in on the upper ocean layers.

bonate (CaCO_3) in the oceans is mostly formed on the surface through limestone microorganisms (ie, foraminifera and coccolitoforid). During the calcification process, these organisms reduce TA and the dissolved organic carbon of the surface, after death these microorganisms, shells precipitate along the water column and also transporting organic matter into the deep ocean. At the time of this precipitation, the shells can be dissolve driven the increase of TA and TCO₂ into the deep ocean that had been incorporated into the surface.

The ocean pH is controlled by the chemistry of CaCO_3 and play an important role to regulating the CO₂ concentrations. When CO₂ dissolves in seawater (eq.3.1) forms carbonic acid (H_2CO_3) its reacts with the pH in order to stabilize the concentrations. As we see in the figure 3.13 the pH was higher in the LGM than in the MIS11c. The average surface pH (table. 3.4) in the Southern Ocean of the LGM was

8.45 while for the MIS11c was 8.14, a decrease of 0.31. This results are in agreement with Ridgwell (2011); Heinze and Ilyina (2015), that found in late Paleocene climate that was warmer than today, a lower pH (0.45) where the waters were more acidic, consistent with an increase of CO₂ concentrations.

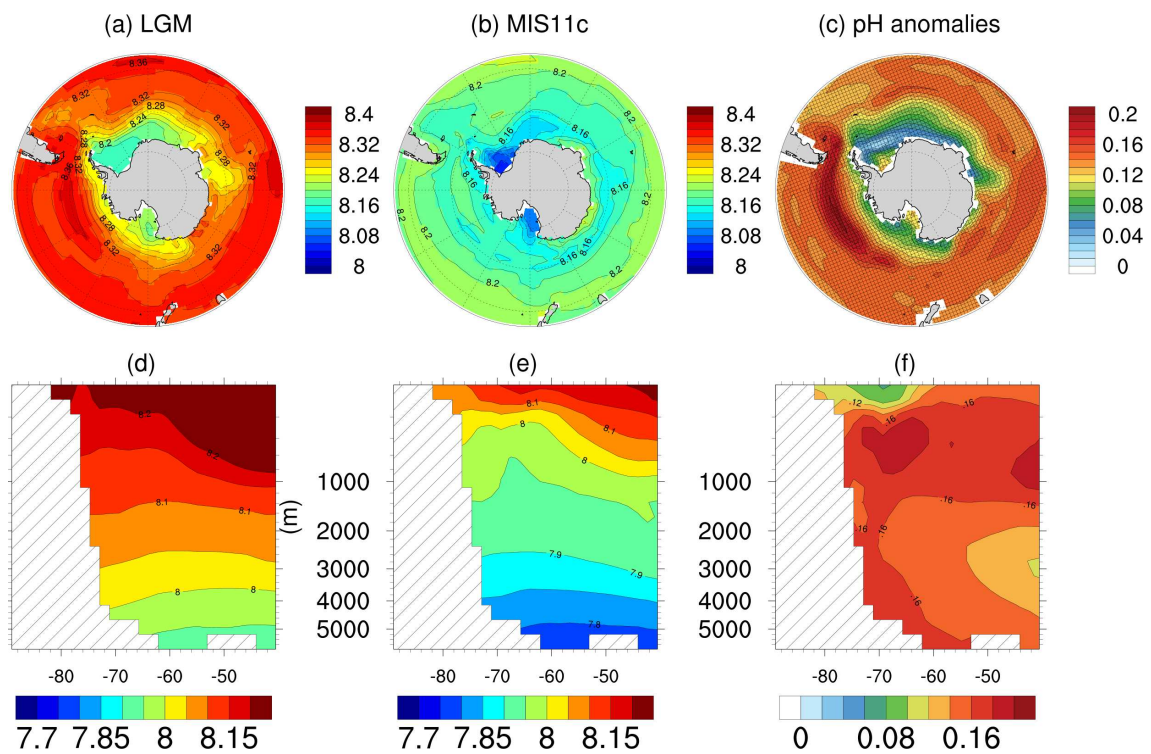


Figure 3.13: pH for the surface (a) LGM,(b) MIS11c, (c) anomalies and averaged meridional crosscut for (d) LGM, (e) MIS11c and (f) anomalies. Note the nonlinear vertical axes, used to zoom in on the upper ocean layers.

Equations 3.4 and 3.5 describe the chemical ocean buffer system which is basically a combination of dissociation reactions in order to eliminate H²⁺ sources for seawater, however, according to Henry's Law (eq. 3.8) the removal of CO₂ as in the glacial ages, tends to change the reaction (eq. 3.2) to the left decreasing production of H₂CO₃ and the oceans have 10% more CO₃²⁻ than H₂CO₃ and about 90% reacts with CO₃²⁻ is to form HCO₃. It is expected a decreases the concentrations of HCO₃ and an increasing of CO₃²⁻ concentrations in glacial times, as we can see in figure 3.14.

The decrease of $p\text{CO}_2$ in LGM simulations and well documented in ice core data demands a glacial increase of CO_3^{2-} essentially in ocean surface (Fig. 3.14). As we see above, lower CO_2 atmospheric in LGM causes a shift from HCO_3^- to CO_3^{2-} , and unlike higher CO_2 in MIS11c simulation change backwards (Fig. 3.14 and 3.15). The increase (decrease) of $\text{CO}_3^{2-} : \text{TCO}_2$ ratio in LGM (MIS11c) simulation, can increase (reduced) the oceanic buffer capacity for CO_2 perturbations. So, we can clearly see what happens in interglacial periods like MIS11c, the increase of $p\text{CO}_2$ with the consequent increase of consumption of CO_2 , increases the production of HCO_3^- (Fig. 3.15) and consumption of CO_3^{2-} (Fig. 3.14) to compose the carbonate carcass of the marine plankton. This increase in $p\text{CO}_2$ also promotes the decrease of pH (Fig.3.13) with the highest increase of available H^+ ions.

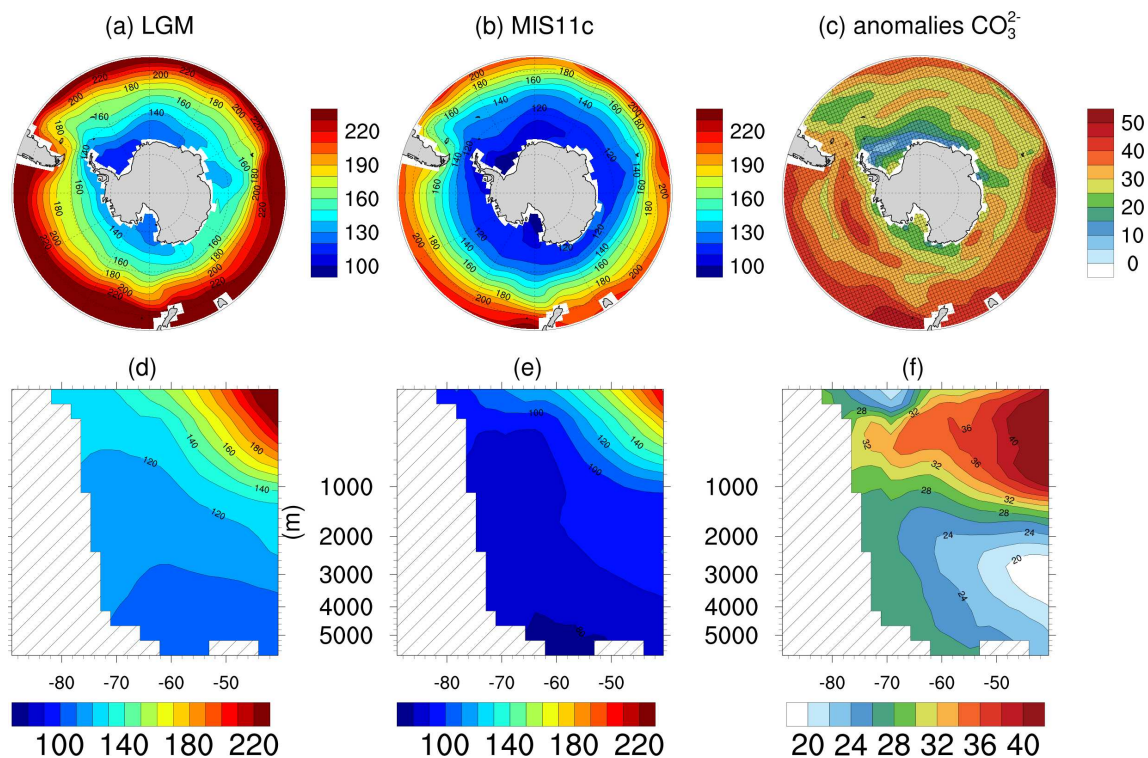


Figure 3.14: CO_3^{2-} in $\mu\text{mol/kg}$ for the surface (a) LGM,(b) MIS11c, (c) anomalies and averaged meridional crosscut for (d) LGM, (e) MIS11c and (f) anomalies. Note the nonlinear vertical axes, used to zoom in on the upper ocean layers.

The dissolution of CaCO_3 is dependent on the saturation state of seawater Ω

with respect to aragonite or calcite (Sarmiento and Gruber, 2007), the seawater saturation Ω can be defined by the product of CO_3^{2-} and Ca^{2+} ion concentrations as a product at the in situ temperature, pressure and salinity (Chung et al., 2003).

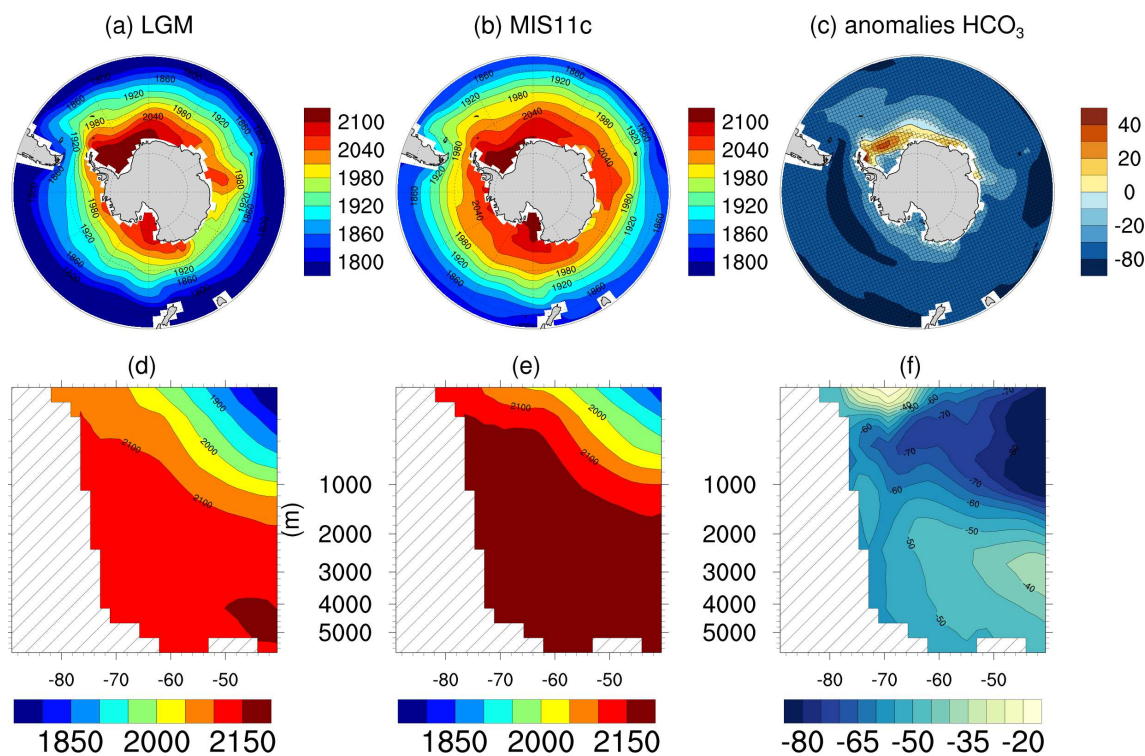


Figura 3.15: HCO_3^- in $\mu\text{mol}/\text{kg}$ for the surface (a) LGM, (b) MIS11c, (c) anomalies and averaged meridional crosscut for (d) LGM, (e) MIS11c and (f) anomalies. Note the nonlinear vertical axes, used to zoom in on the upper ocean layers.

The representation of calcium carbonate (CaCO_3) chemistry on the ocean surface in this study will be through the saturation state of aragonite (Ω), which is a widely used indicator rates of calcification (Langdon et al., 2000). Surface Ω was always supersaturated ($\Omega > 1$), ranging between 1.34 to 3.6 for MIS11c and 1.4 to 4.8 for LGM. The average over Southern ocean (table. 3.4) was 3.02 (3.68) for MIS11c (LGM). Surface Ω aragonite showed similar spatial distribution to sea surface temperature (Fig. 3.4) with Ω being highest where the surface ocean was warmest. The highest values in the region between 40°S and 55°S for LGM and between 40°S and 45°S for MIS11c. The surface Ω behaviour is higher in the subtropical

regions and lower in the high latitudes. Changes between the LGM and the MIS11c (Fig. 3.16c) shows higher values at the surface than deep ocean (Fig. 3.16f). The high surface Ω in the LGM simulations can be explained by the low concentrations of $f\text{CO}_2$, reduction of the TCO_2 concentration in the surface and also increase of the pH (Fig. 3.13) which leads to an increase of Ω an inverse process of ocean acidification.

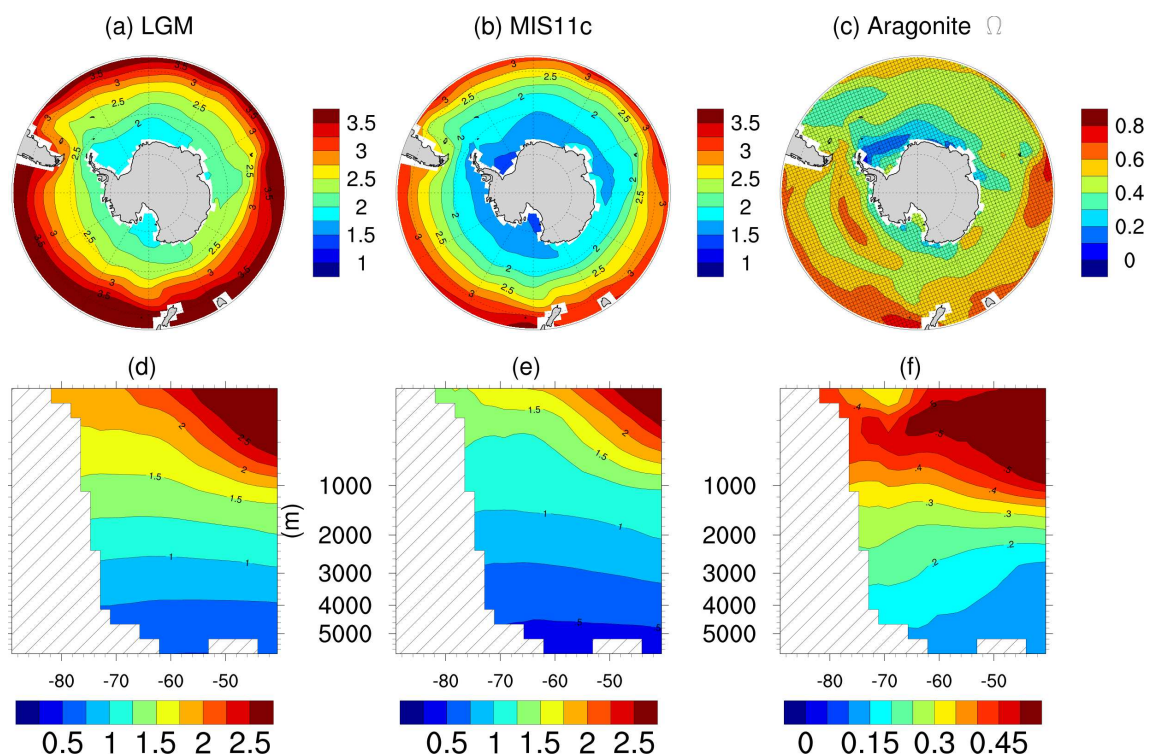


Figura 3.16: Ω CaCO₃ for the surface (a) LGM,(b) MIS11c, (c) anomalies and averaged meridional crosscut for (d) LGM, (e) MIS11c and (f) anomalies. Note the nonlinear vertical axes, used to zoom in on the upper ocean layers.

The Southern Ocean calcite saturation depth for LGM and MIS11c are shown in the figure 3.17. We can observe that for the interglacial period of the MIS11c the depth of saturation is of 1674 m, whereas for the LGM depth was of 2600 m.

The shoaling of aragonite horizontal saturation (AHS) in MIS11c is associated with oceanic equilibrium due to increased atmospheric CO₂ and decreased TA. Unlike, the simulations of LGM, the great decrease of CO₂ acting with the increase

of alkalinity and further deepening the ASH. The depth of the LGM simulation was about 1000 meters deeper than found in the MIS11c. The elevated temperatures of the MIS11c relative to the LGM (Fig. 3.4) leads a decrease in the saturation concentrations of CO_3^{2-} and this would lead to increased of Ω .

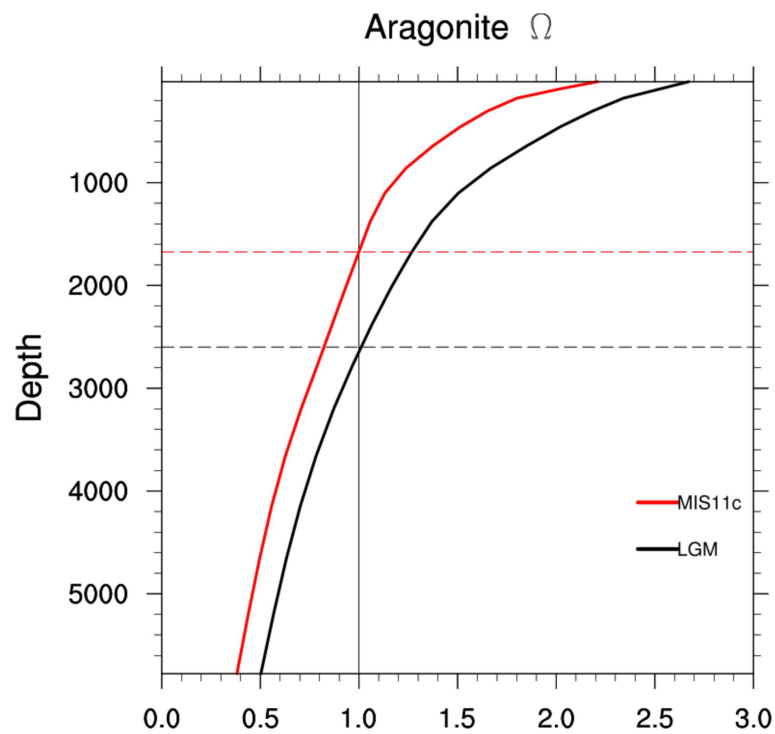


Figura 3.17: Depth profile of Ω aragonite on Southern Ocean. Black line for LGM simulations and red for MIS11c. Gray line for $\Omega = 1$ are the *Aragonite Saturation Horizon* (ASH), dashed lines show the depth of ASH for each simulation.

3.3.4 Characteristics in the Weddell Sea

The Southern Ocean variability discussed above demonstrates that the Weddell Sea experience largest differences between the LGM and MIS11c simulations. In order to investigate this in more details, this section presents the vertical distribution of components of the biogeochemical cycle for the Weddell Sea in the LGM and MIS11c periods.

The Weddell Sea (60 °W to 20 °E and 55 °S to 75 °S) plays a key role in the global thermohaline circulation through the abyssal ventilation of the oceans (Rahmstorf, 2002). The Weddell Sea is one of the most important source for AABW formation (Orsi et al., 1993; Williams et al., 2019). In this region, water masses are formed derived from the AABW, such as Warmer, Deep Water (WDW), Weddell Sea Deep Water (WSDW) and Weddell Sea Bottom Water (WSBW). The WDW is relatively warmer and saltier than WSDW and WSBW, range between 200 to 1500 meters, the WSDW is found bellow of WDW and WSBW occupies the bottom layer of deep Weddell Sea (Fahrbach et al., 2011).

Figure 3.18 shows the vertical profile of temperature (a), salinity, O₂, PO₄³⁻ and NO₃⁻. The temperature maximum within the Weddell Basin range between -0.75 °C to +1 °C for MIS11c and -2 °C to -1 °C for LGM. For the salinity the range diversify between 34 to 34.6 and 34.4 to 34.8 for MIS11c and LGM respectively. The temperature and salinity profile in the water column (Fig. 3.18a and b) shows for MIS11c that the mixed layer is separated by a intense pycnocline from 100 - 200 m which can corresponded to the to WDW (Fahrbach et al., 2011). Considering that the WDW formation was reduced in the glacial times (Grobe and Mackensen,

1992; Pudsey, 1992) due to greater sea-ice cover, it is not possible to identify this profile in our LGM simulation. The dominated by the WDW is poorly oxygenated (Fig. 3.18 c) but nutrient rich water mass (Fig. 3.18d and e). The slowly decrease of temperature and salinity for both simulations may represent a branch of the AABW, correspondent to the WSDW. Since, the AABW is a rich oxygen water mass (Broecker et al., 1998), note the Figure 3.18 c an increment in oxygen concentrations for both simulations, between 3000 - 5000 m may corresponde to the WSDW.

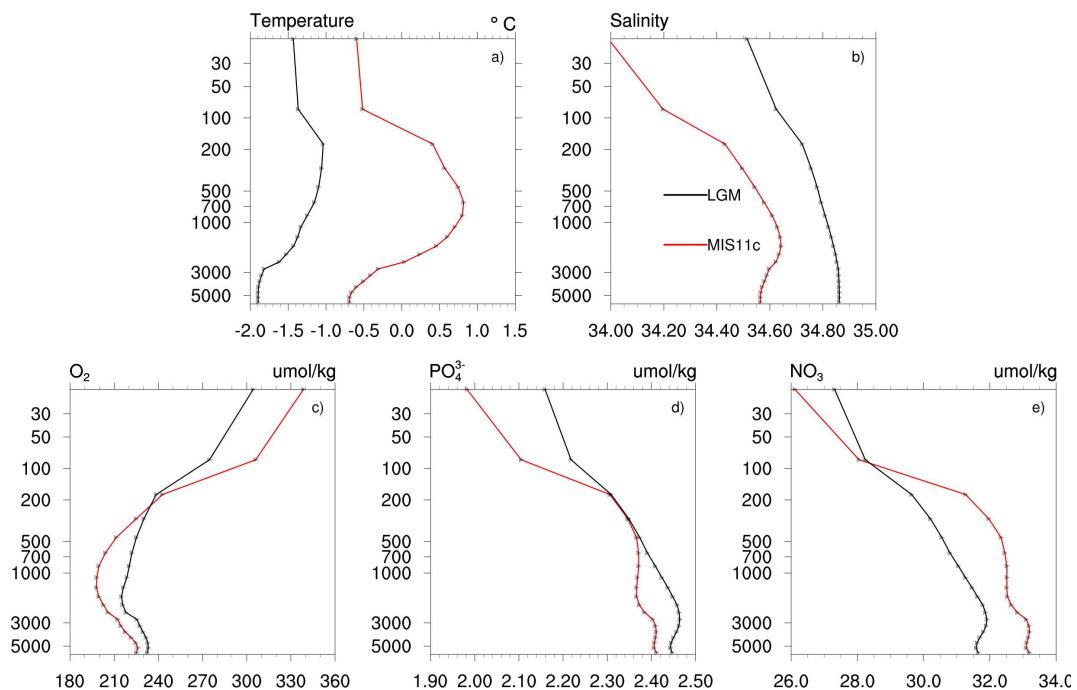


Figura 3.18: Globally averaged of Weddell Sea vertical profiles of temperature (°C), salinity, oxygen, phosphate and nitrate (all in $\mu\text{mol/kg}$). Black lines show LGM distributions; red lines show MIS11c concentrations calculated within UVic experiments. Note the nonlinear vertical axes, used to zoom in on the upper ocean layers

The concentrations of PO_4^{3-} and NO_3^- , are shown in figure 3.18 d and e. PO_4^{3-} shows higher concentrations in the first 100 meters in LGM simulation than in the MIS11c. Concentrations at surface levels range from $2\mu\text{mol/kg}$ and $2.2\mu\text{mol/kg}$, to $2.4\mu\text{mol/kg}$ e $2.45\mu\text{mol/kg}$ in the deep ocean for MIS11c and LGM, respec-

tively. The region of the WDW shows concentrations of PO_4^{3-} very similar for both simulations, with an increase of $0.15 \mu\text{mol/kg}$ for LGM and $0.30 \mu\text{mol/kg}$ for MIS11c simulation, remaining almost constant up to 3000 m, where they increased again. Turning to the NO_3^- , the concentrations range between $26 \mu\text{mol/kg}$ to $28 \mu\text{mol/kg}$ at surface to $32 \mu\text{mol/kg}$ and $33.5 \mu\text{mol/kg}$ in the deep ocean for MIS11c and LGM, respectively. The NO_3^- has higher surface concentrations for the LGM simulation, in contrast, below 200 meters, there is an increase for MIS11c simulation, can be explained by the nitrate uptake by phytoplankton, where the supply to the surface layer was inhibited by a rise of the pycnocline for the LGM than MIS11c simulation.

The 3.19 show de carbonate chemistry in the Weddell Sea. For the upper levels the LGM simulation shows high TA (Fig. 3.18a) range from $2400 \mu\text{mol/kg}$ to $2425 \mu\text{mol/kg}$ in the deep ocean. The MIS11c simulation shows for TA values that ranges from $2345 \mu\text{mol/kg}$ to $2410 \mu\text{mol/kg}$ in the deep layer. Decrease of TCO_2 in the surface (almost 50 meters) (Fig. 3.18a) and a increment in the water column from $2200 \mu\text{mol/kg}$ to $2300 \mu\text{mol/kg}$ for LGM simulation, can be attributed to increase of salinity and the precipitation of CO_2 in deeper layers. Since, CO_2 atmospheric concentrations is out-of-phase with alkalinity and correlated with TCO_2 , high (lower) CO_2 concentrations leads to a decrease (increase) the TA and decrease (increase) TCO_2 (Fig. 3.19 b), however, MIS11c has lower concentrations than found in the LGM simulation.

The CO_3^{2-} and HCO_3^- (Fig. 3.19 c and d) have the expected pattern as higher concentrations throughout the water column of the CO_3^{2-} compared to HCO_3^- for the LGM in relation to the MIS11c simulation. This is mainly due to the concentra-

tion of CO_2 on the surface and its absorption via carbon pump. The absorption of CO_2 in the interglacial periods by the oceans alters the chemistry of seawater and rise the TCO_2 and HCO_3^- , with an reduced of CO_3^{2-} and calcium saturation degree (Ω) and pH (Zeebe and Wolf-Gladrow, 2001; Caldeira and Wickett, 2003).

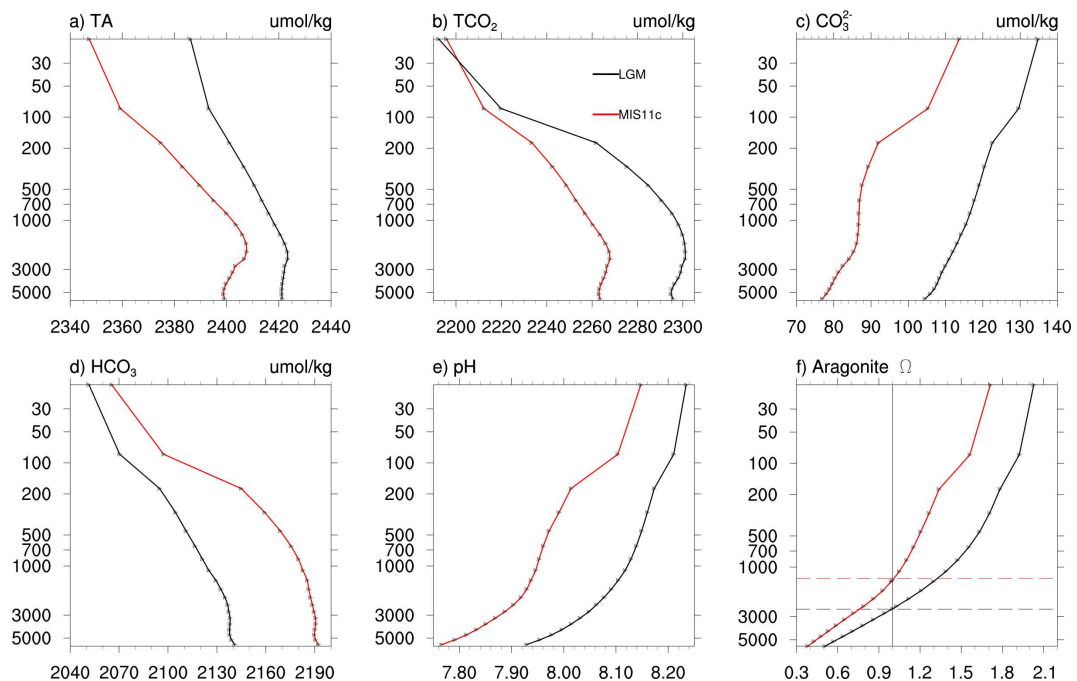


Figura 3.19: Same as Fig. 3.18 but for TA, TCO_2 , carbonate, bicarbonate (all in $\mu\text{mol/kg}$), pH and $\Omega \text{ CaCO}_3$. Black lines show LGM distributions; red lines show MIS11c concentrations calculated within UVic experiments and CO2SYS. Gray line for $\Omega = 1$ are the *Aragonite Saturation Horizon* (ASH), dashed lines show the depth of ASH for each simulation. Note the nonlinear vertical axes, used to zoom in on the upper ocean layers.

...

Many models demonstrate elevated deep ocean CO_3^{2-} concentration for part of the glacial CO_2 decrease (Toggweiler, 1999; Sigman et al., 2010) conducted by high surface alkalinity. High surface alkalinity leads to an increment of pH concentrations, as we see in Figure 3.19 e. The pH in surface of LGM simulation for Weddell Sea are 8.2 and reaches 7.9 in the deep ocean. The MIS11c simulation, the surface pH are 8.1 and 7.75 in the deep ocean. Note the pH vertical distribution for both simulations, generally show a pronounced minimum with a maximum of temperature (Fig. 3.18a) and salinity (Fig. 3.18 b). The similar vertical pattern of CO_3^{2-} between both simulations suggests that increasing the gradient between surface and deep ocean requires a large amount of CO_2 stored in the deep sea, probably due to remineralization of matter organic (Yu et al., 2014).

The ocean surface of Ω was always supersaturated ($\Omega > 1$). In the LGM Ω was 2 and in the MIS11c simulation was 1.6. The saturation depth of aragonite (Fig. 2) for MIS11c was 1288 m and 2542 m for the LGM, being 1254 m deeper, corresponding to the difference between the concentrations of CO_3^{2-} of $40 \mu\text{mol/kg}$ between both simulations. In fact, the saturation horizon of calcium carbonate is related to the depth of abrupt pH decrease (Fig. 3.19 e). That is, the decrease of the pH makes the waters more acidic, thus favoring the dissolution of CaCO_3 .

Our results is in agreement with Rickaby et al. (2010); Sigman and Boyle (2000), where the increase of alkalinity in the glacial periods than interglacial changes the carbonate accumulation. The deeper the ASH in LGM than MIS11c, increase the carbonate accumulation in the deep ocean confine more CO_2 . Indeed, when the transition of glacial to interglacial peridos occurs, degassing of CO_2 from the ocean provide a trigger to rise $p\text{CO}_2$ in warmer climates. Areas where they are found

elevated surface pH and Aragonite Ω values, correspond to lower NO_3^- in the surface suggesting high biological activity with high CO_2 uptake.

3.4 Summary and Conclusions

Modeling the Earth's climate is a challenge due to the complex climate system features. This study investigates the interglacial period of MIS11c (428-383 kyr BP) and the LGM, where CO₂ concentrations differ to those found in the pre-industrial period.

Since the Southern Ocean is particularly susceptible to climate changes, comparing the two simulations, the LGM due to lower temperatures on surface to the ocean floor as well as higher salinity and lower stratification. Thus, the LGM is dominated by AABW and larger storage of CO₂ in SO during LGM than interglacials.

The response of biogeochemical cycle to the simulated LGM and MIS11c on SO has shown a large increase of surface oxygen southward 55 °S and a decrease in west Antarctic region (in particular in the Weddell Sea). Analyses for the NO₃, PO₅³⁻, TCO₂ and TA demonstrates that they are closely linked as response of a decrease or increase CO₂ concentrations, between atmosphere and ocean surface. The SO deep ocean show a large increase in the vertical gradient of these species due to increase of AABW. The deep ocean CO₃²⁻ and HCO₃ is linked to processes that affect carbon reorganization in the surface ocean and it is in response to changes in carbonate buffer system causing changes in pH and mainly in the saturation depth of CaCO₃.

The uptake of CO₂ into the oceans is controlled primarily by the concentration of CO₃²⁻ into the water column. This feedback with an increase of CO₂ concentrations in the sea water is what we call ocean acidification. The opposite is expected in the glacial periods, as the low concentrations of CO₂ are related to the increase

in pH, CO_3^{2-} e da TA. Because increasing deep water CO_3^{2-} concentrations would promote a deep-sea CaCO_3 preservation with increase of depth of in aragonite saturation (Fig. 3.16) between LGM and MIS11c, thus deplete oceanic TA inventory with CO_3^{2-} rise likely reflects of decrease TCO_2 (Yu et al., 2013, 2014).

Referências Bibliográficas

- Annan, J. D. and Hargreaves, J. C. (2013). A new global reconstruction of temperature changes at the Last Glacial Maximum. *Climate of the Past*, 9(1):367–376.
- Archer, D. (1996). A data-driven model of the global calcite lysocline. *Global Biogeochemical Cycles*, 10(3):511–526.
- Argus, D. F., Peltier, W. R., Drummond, R., and Moore, A. W. (2014). The Antarctica component of postglacial rebound model ICE-6G_C (VM5a) based on GPS positioning, exposure age dating of ice thicknesses, and relative sea level histories. *Geophysical Journal International*, 198(1):537–563.
- Banderas, R., Álvarez-Solas, J., and Montoya, M. (2012). Role of CO_2 and Southern Ocean winds in glacial abrupt climate change. *Climate of the Past*, 8(3):1011–1021.
- Bates, N., Astor, Y., Church, M., Currie, K., Dore, J., Gonaález-Dávila, M., Lorenzoni, L., Muller-Karger, F., Olafsson, J., and Santa-Casiano, M. (2014). A Time-Series View of Changing Ocean Chemistry Due to Ocean Uptake of Anthropogenic CO_2 and Ocean Acidification. *Oceanography*, 27(1):126–141.
- Bereiter, B., Eggleston, S., Schmitt, J., Nehrbass-Ahles, C., Stocker, T. F., Fischer, H., Kipfstuhl, S., and Chappellaz, J. (2015). Revision of the EPICA Dome C CO_2

- record from 800 to 600 kyr before present. *Geophysical Research Letters*, 42(2):542–549.
- Berger, A. and Loutre, M. (1991). Insolation values for the climate of the last 10 million years. *Quaternary Science Reviews*, 10(4):297–317.
- Broecker, W. S. (1982). Glacial to interglacial changes in ocean chemistry. *Progress in Oceanography*, 11(2):151–197.
- Broecker, W. S., Peacock, S. L., Walker, S., Weiss, R., Fahrback, E., Schroeder, M., Mikolajewicz, U., Heinze, C., Key, R., Peng, T.-H., and Rubin, S. (1998). How much deep water is formed in the Southern Ocean? *Journal of Geophysical Research: Oceans*, 103(C8):15833–15843.
- Buchanan, P. J., Matear, R. J., Lenton, A., Phipps, S. J., Chase, Z., and Etheridge, D. M. (2016). The simulated climate of the Last Glacial Maximum and insights into the global marine carbon cycle. *Climate of the Past*, 12(12):2271–2295.
- Caldeira, K. and Wickett, M. E. (2003). Anthropogenic carbon and ocean pH. *Nature*, 425(6956):365–365.
- Chavaillaz, Y., Codron, F., and Kageyama, M. (2013). Southern westerlies in LGM and future (RCP4.5) climates. *Climate of the Past*, 9(2):517–524.
- Chung, S.-N., Lee, K., Feely, R. A., Sabine, C. L., Millero, F. J., Wanninkhof, R., Bullister, J. L., Key, R. M., and Peng, T.-H. (2003). Calcium carbonate budget in the Atlantic Ocean based on water column inorganic carbon chemistry. *Global Biogeochemical Cycles*, 17(4):n/a–n/a.

- Clark, P. U., Dyke, A. S., Shakun, J. D., Carlson, A. E., Clark, J., Wohlfarth, B., Mitrovica, J. X., Hostetler, S. W., and McCabe, A. M. (2009). The Last Glacial Maximum. *Science*, 325(5941):710–714.
- Coletti, A. J., DeConto, R. M., Brigham-Grette, J., and Melles, M. (2015a). A GCM comparison of Pleistocene super-interglacial periods in relation to Lake El'gygytyn, NE Arctic Russia. *Climate of the Past*, 11(7):979–989.
- Coletti, A. J., DeConto, R. M., Brigham-Grette, J., and Melles, M. (2015b). A GCM comparison of Pleistocene super-interglacial periods in relation to Lake El'gygytyn, NE Arctic Russia. *Climate of the Past*, 11(7):979–989.
- Cronin, T., Polyak, L., Reed, D., Kandiano, E., Marzen, R., and Council, E. (2013). A 600-ka Arctic sea-ice record from Mendeleev Ridge based on ostracodes. *Quaternary Science Reviews*, 79:157–167.
- Dickson, A.G., Sabine, C.L. and Christian, J. (2007). *Guide to best practices for ocean CO2 measurements*, volume 3. PICES Special Publication.
- Duplessy, J. C., Shackleton, N. J., Fairbanks, R. G., Labeyrie, L., Oppo, D., Labeyrie, L., Oppo, D., and Kallel, N. (1988). Abstract . The degree of similarity of the • 13C an oxygenated 13C rich Intermediate Water 3 Lamont Doherty Geological Observatory , climatic cycles (a few 105 years), variations in al3C is more homogenous in those basins locations , deepwater a • 3C ch. *Paleoceanography*, 3(3):343–360.
- Eby, M., Zickfeld, K., Montenegro, A., Archer, D., Meissner, K. J., and Weaver, A. J. (2009). Lifetime of Anthropogenic Climate Change: Millennial Time Scales

- of Potential CO₂ and Surface Temperature Perturbations. *Journal of Climate*, 22(10):2501–2511.
- Fahrbach, E., Hoppema, M., Rohardt, G., Boebel, O., Klatt, O., and Wisotzki, A. (2011). Warming of deep and abyssal water masses along the Greenwich meridian on decadal time scales: The Weddell gyre as a heat buffer. *Deep-Sea Research Part II: Topical Studies in Oceanography*, 58(25-26):2509–2523.
- Fairbanks, R. G. (1989). A 17,000-year glacio-eustatic sea level record: influence of glacial melting rates on the Younger Dryas event and deep-ocean circulation. *Nature*, 342(6250):637–642.
- Ferrari, R., Jansen, M. F., Adkins, J. F., Burke, A., Stewart, A. L., and Thompson, A. F. (2014). Antarctic sea ice control on ocean circulation in present and glacial climates. *Proceedings of the National Academy of Sciences*, 111(24):8753–8758.
- Grobe, H. and Mackensen, A. (1992). Late Quaternary climatic cycles as recorded in sediments from the Antarctic continental margin. In *The Antarctic Paleoenvironment: A Perspective on Global Changes*, volume 56, pages 349–376. American Geophysical Union (AGU).
- Heinze, M. and Ilyina, T. (2015). Ocean biogeochemistry in the warm climate of the late Paleocene. *Climate of the Past*, 11(1):63–79.
- Huybrechts, P. (2002). Sea-level changes at the LGM from ice-dynamic reconstructions of the Greenland and Antarctic ice sheets during the glacial cycles. *Quaternary Science Reviews*, 21(1-3):203–231.

- IPCC (2014). *Climate Change 2014: Synthesis Report. Contribution of Working Groups I, II and III to the Fifth Assessment Report of the Intergovernmental Panel on Climate Change*. Cambridge University Press, Geneva, Switzerland.
- Kobayashi, S., Ota, Y., Harada, Y., Ebata, A., Moriya, M., Onoda, H., Onogi, K., Kamahori, H., Kobayashi, C., Endo, H., Miyaoka, K., and Takahashi, K. (2015). The JRA-55 Reanalysis: General Specifications and Basic Characteristics. *Journal of the Meteorological Society of Japan. Ser. II*, 93:5–48.
- Kubota, K., Yokoyama, Y., Ishikawa, T., Obrochta, S., and Suzuki, A. (2014). Larger CO₂ source at the equatorial Pacific during the last deglaciation. *Scientific Reports*, 4(June).
- Kusahara, K. and Hasumi, H. (2013). Modeling Antarctic ice shelf responses to future climate changes and impacts on the ocean. *Journal of Geophysical Research: Oceans*, 118(5):2454–2475.
- Kusahara, K., Sato, T., Oka, A., Obase, T., Greve, R., Abe-Ouchi, A., and Hasumi, H. (2015). Modelling the Antarctic marine cryosphere at the Last Glacial Maximum. *Annals of Glaciology*, 56(69):425–435.
- Langdon, C., Takahashi, T., Sweeney, C., Chipman, D., Goddard, J., Marubini, F., Aceves, H., Barnett, H., and Atkinson, M. J. (2000). Effect of calcium carbonate saturation state on the calcification rate of an experimental coral reef. *Global Biogeochemical Cycles*, 14(2):639–654.
- Lewis, E. and Wallace, D. (1998). Program developed for CO₂ system calculations.

In Center, C. D. I. A., editor, *Program developed for CO2 system calculations*. Carbon Dioxide Information Analysis Center, Oak Ridge.

Lippold, J., Gutjahr, M., Blaser, P., Christner, E., de Carvalho Ferreira, M. L., Mulitza, S., Christl, M., Wombacher, F., Böhm, E., Antz, B., Cartapanis, O., Vogel, H., and Jaccard, S. L. (2016). Deep water provenance and dynamics of the (de)glacial Atlantic meridional overturning circulation. *Earth and Planetary Science Letters*, 445:68–78.

Lippold, J., Luo, Y., Francois, R., Allen, S. E., Gherardi, J., Pichat, S., Hickey, B., and Schulz, H. (2012). Strength and geometry of the glacial Atlantic Meridional Overturning Circulation. *Nature Geoscience*, 5(11):813–816.

Loulergue, L., Schilt, A., Spahni, R., Masson-Delmotte, V., Blunier, T., Lemieux, B., Barnola, J. M., Raynaud, D., Stocker, T. F., and Chappellaz, J. (2008). Orbital and millennial-scale features of atmospheric CH₄ over the past 800,000 years. *Nature*, 453(7193):383–386.

Lowell, T. V., Heusser, C. J., Andersen, B. G., Moreno, P. I., Hauser, A., Heusser, L. E., Schluchter, C., Marchant, D. R., and Denton, G. H. (1995). Interhemispheric Correlation of Late Pleistocene Glacial Events. *Science*, 269(5230):1541–1549.

Lu, Z., Hoogakker, B. A. A., Hillenbrand, C.-D., Zhou, X., Thomas, E., Gutchess, K. M., Lu, W., Jones, L., and Rickaby, R. E. M. (2016). Oxygen depletion recorded in upper waters of the glacial Southern Ocean. *Nature Communications*, 7(1):11146.

Lüthi, D., Le Floch, M., Bereiter, B., Blunier, T., Barnola, J. M., Siegenthaler, U., Raynaud, D., Jouzel, J., Fischer, H., Kawamura, K., and Stocker, T. F. (2008).

- High-resolution carbon dioxide concentration record 650,000-800,000 years before present. *Nature*, 453(7193):379–382.
- Marchitto, T. M. and Broecker, W. S. (2006). Deep water mass geometry in the glacial Atlantic Ocean: A review of constraints from the paleonutrient proxy Cd/Ca. *Geochemistry, Geophysics, Geosystems*, 7(12).
- Matear, R. J., Lenton, A., Etheridge, D., and Phipps, S. J. (2015). The simulated climate of the Last Glacial Maximum and the insights into the global carbon cycle. *Climate of the Past Discussions*, 11(2):1093–1142.
- Melles, M., Brigham-Grette, J., Minyuk, P. S., Nowaczyk, N. R., Wennrich, V., DeConto, R. M., Anderson, P. M., Andreev, A. A., Coletti, A., Cook, T. L., Haltia-Hovi, E., Kukkonen, M., Lozhkin, A. V., Rosen, P., Tarasov, P., Vogel, H., and Wagner, B. (2012). 2.8 Million Years of Arctic Climate Change from Lake El'gygytgyn, NE Russia. *Science*, 337(6092):315–320.
- Mix, A. C., Bard, E., and Schneider, R. (2001). Environmental processes of the ice age: Land, oceans, glaciers (EPILOG). *Quaternary Science Reviews*, 20(4):627–657.
- Mucci, A. (1983). The solubility of calcite and aragonite in seawater at various salinities, temperatures, and one atmosphere total pressure. *American Journal of Science*, 283(7):780–799.
- NOAA (2018). Global Greenhouse Gas Reference Network. *Earth System Research Laboratory, NOAA*, pages 3–4.
- Orr, J. C. (1999). On ocean carbon-cycle model comparison. *Tellus, Series B: Chemical and Physical Meteorology*, 51(2):509–510.

- Orr, J. C. and Epitalon, J. M. (2015). Improved routines to model the ocean carbonate system: Mocsy 2.0. *Geoscientific Model Development*, 8(3):485–499.
- Orsi, A. H., Nowlin, W. D., and Whitworth, T. (1993). On the circulation and stratification of the Weddell Gyre. *Deep Sea Research Part I: Oceanographic Research Papers*, 40(1):169–203.
- Orsi, H., Whitworth, T., and Nowlin, W. D. (1995). On the meridional extent and fronts of the Antarctic Circumpolar Current Pronounced meridional gradients in surface properties separate waters of the Southern Ocean from the warmer and saltier waters of the subtropical circulations . Deacon (1933 , the S. *Deep Sea Research*, 42(5):641–673.
- Peltier, W. R., Argus, D. F., Drummond, R., Strange, A., Peltier, W. R., Argus, D. F., Drummond, R., Shahnas, M. H., Yuen, D. A., Pysklywec, R. N., Peltier, W. R., Argus, D. F., Drummond, R., Tarayoun, A., Audet, P., Mazzotti, S., Ashoori, A., Peltier, W. R., Argus, D. F., and Drummond, R. (2015). Journal of Geophysical Research : Solid Earth. *Journal of Geophysical Research: Solid Earth*, 2015(120):450–487.
- Pudsey, C. J. (1992). Late quaternary changes in Antarctic bottom water velocity inferred from sediment grain size in the northern Weddell Sea. *Marine Geology*, 107(1-2):9–33.
- Rahmstorf, S. (2002). Ocean circulation and climate during the past 120,000 years. *Nature*, 419(6903):207–214.

- Raymo, M. E. and Mitrovica, J. X. (2012). Collapse of polar ice sheets during the stage 11 interglacial. *Nature*, 483(7390):453–456.
- Rickaby, R. E., Elderfield, H., Roberts, N., Hillenbrand, C. D., and Mackensen, A. (2010). Evidence for elevated alkalinity in the glacial Southern Ocean. *Paleoceanography*, 25(1):1–15.
- Ridgwell, A. (2011). Evolution of the ocean's "biological pump". *Proceedings of the National Academy of Sciences*, 108(40):16485–16486.
- Sarmiento, J. L. and Gruber, N. (2007). *Ocean Biogeochemical Dynamics*. Ocean Biogeochemical Dynamics, Jorge L. Sarmiento and Nicolas Gruber, Princeton U. Press, Princeton, NJ, 2006. \$75.00 (503 pp.). ISBN 978-0-691-01707-5. *Physics Today*, 60(6):65–65.
- Sarmiento, J. L. and Toggweiler, J. R. (1984). A new model for the role of the oceans in determining atmospheric P CO₂. *Nature*, 308(5960):621–624.
- Schartau, M. and Oschlies, A. (2004). Simultaneous data-based optimization of a 1D-ecosystem model at three locations in the North Atlantic: Part I—Method and parameter estimates. *Journal of Marine Research*, 61(6):765–793.
- Schmitt, R. (2011). Salinity and the Global Water Cycle. *Oceanography*, 21(1):12–19.
- Schmittner, A. and Galbraith, E. D. (2008). Glacial greenhouse-gas fluctuations controlled by ocean circulation changes. *Nature*, 456(7220):373–376.
- Schmittner, A., Oschlies, A., Giraud, X., Eby, M., and Simmons, H. L. (2005). A global model of the marine ecosystem for long-term simulations: Sensitivity to

ocean mixing, buoyancy forcing, particle sinking, and dissolved organic matter cycling. *Global Biogeochemical Cycles*, 19(3):1–17.

Schmittner, A., Urban, N. M., Shakun, J. D., Mahowald, N. M., Clark, P. U., Bartlein, P. J., Mix, A. C., and Rosell-Melé, A. (2011). Climate sensitivity estimated from temperature reconstructions of the Last Glacial Maximum. *Science*, 334(6061):1385–1388.

Shackleton, N. J. and Pisias, N. G. (2013). Atmospheric Carbon Dioxide, Orbital Forcing, and Climate. In *The Carbon Cycle and Atmospheric CO₂: Natural Variations Archean to Present*, volume 32, pages 303–317. American Geophysical Union (AGU).

Shadwick, E. H., Trull, T. W., Thomas, H., and Gibson, J. A. (2013). Vulnerability of polar oceans to anthropogenic acidification: Comparison of arctic and antarctic seasonal cycles. *Scientific Reports*, 3.

Sigman, D. M. and Boyle, E. A. (2000). Glacial/interglacial variations in atmospheric carbon dioxide. *Nature*, 407(6806):859–869.

Sigman, D. M., Hain, M. P., and Haug, G. H. (2010). The polar ocean and glacial cycles in atmospheric CO₂ concentration. *Nature*, 466(7302):47–55.

Tagliabue, A., Bopp, L., Roche, D. M., Bouttes, N., Dutay, J.-C., Alkama, R., Kageyama, M., Michel, E., and Paillard, D. (2009). Quantifying the roles of ocean circulation and biogeochemistry in governing ocean carbon-13 and atmospheric carbon dioxide at the last glacial maximum. *Climate of the Past*, 5(4):695–706.

- Takahashi, T., Sutherland, S., Chipman, D., Goddard, J., Ho, C., Newberger, T., Sweeney, C., and Munro, D. (2014). Climatological distributions of pH, pCO₂, total CO₂, alkalinity, and CaCO₃ saturation in the global surface ocean, and temporal changes at selected locations. *Marine Chemistry*, 164:95–125.
- Taylor, K. E. (2001). Summarizing multiple aspects of model performance in a single diagram. *Journal of Geophysical Research: Atmospheres*, 106(D7):7183–7192.
- Toggweiler, J. R. (1999). Variation of atmospheric of the ocean ' s deepest water than seen O_{2d} O_{2d} – O_{2h-ro2} : P PO_{4d} f h d + T O_{2h}. *October*, 14(5):571–588.
- Tzedakis, P. C. (2010). The MIS 11 - MIS 1 analogy, southern European vegetation, atmospheric methane and the "early anthropogenic hypothesis. *Climate of the Past*, 6(2):131–144.
- Weaver, A. J., Eby, M., Fanning, A. F., and Wiebe, E. C. (1998). Simulated influence of carbon dioxide, orbital forcing and ice sheets on the climate of the Last Glacial Maximum. *Nature*, 394(6696):847–853.
- Williams, T. J., Hillenbrand, C., Piotrowski, A. M., Allen, C. S., Frederichs, T., Smith, J. A., Ehrmann, W., and Hodell, D. A. (2019). Palaeocirculation and ventilation history of Southern Ocean sourced deep water masses during the last 800,000 years. *Paleoceanography and Paleoclimatology*, pages 1–20.
- Yu, J., Anderson, R., and Rohling, E. (2014). Deep Ocean Carbonate Chemistry and Glacial-Interglacial Atmospheric CO₂ Change. *Oceanography*, 27(1):16–25.
- Yu, J., Anderson, R. F., Jin, Z., Rae, J. W., Opdyke, B. N., and Eggins, S. M. (2013).

Responses of the deep ocean carbonate system to carbon reorganization during the Last Glacial-interglacial cycle. *Quaternary Science Reviews*, 76:39–52.

Yu, J., Menviel, L., Jin, Z. D., Thornalley, D. J., Barker, S., Marino, G., Rohling, E. J., Cai, Y., Zhang, F., Wang, X., Dai, Y., Chen, P., and Broecker, W. S. (2016). Sequestration of carbon in the deep Atlantic during the last glaciation. *Nature Geoscience*, 9(4):319–324.

Zeebe and Wolf-Gladrow (2001). CO₂ in seawater: Equilibrium, Kinetics, Isotopes. In Halpern, D., editor, *Elsevier oceanography series*. Elsevier Oceanography Series.

Perspectivas Futuras

- Melhorar as simulações do MIS11c e de outros interglaciais, com inserção de topografias e batimetrias.
- Analisar comparativamente os efeitos das forçantes orbitais e de concentração do CO₂ entre outros interglaciais, com cenários do presente e do futuro
- Quantificar a importância do Oceano Austral na absorção e liberação de CO₂ nos períodos interglaciais e qual a reação da biogeoquímica oceânica nesses cenários, principalmente devido ao processo de acidificação oceânica. Tentando entender qual a resposta dos oceanos para se restaurar equilíbrio.
- Setorizar o Oceano Austral e analisar individualmente a importância e as contribuições dos Mares Antárticos.
- Analisar comparativamente outros modelos biogeoquímicos acoplados.